Spectroscopische gassensoren gebaseerd op silicium-fotonica

Silicon Photonics Spectroscopic Trace Gas Sensors

Anton Vasiliev

Promotoren: prof. dr. ir. G. Roelkens, prof. dr. ir. R. Baets
Proefschrift ingediend tot het behalen van de graad van
Doctor in de ingenieurswetenschappen: fotonica

UNIVERSITEIT
GENT

Vakgroep Informatietechnologie
Voorzitter: prof. dr. ir. B. Dhoedt
Faculteit Ingenieurswetenschappen en Architectuur
Academiejaar 2019 - 2020

ISBN 978-94-6355-360-5
NUR 959, 926
Wettelijk depot: D/2020/10.500/37

Universiteit Gent
Faculteit Ingenieurswetenschappen en Architectuur
Vakgroep Informatietechnologie

Promotoren: Prof. Dr. Ir. Günther Roelkens
Prof. Dr. Ir. Roel Baets

Examencommissie:

em. prof. dr. ir. Daniël De Zutter (voorzitter)	Universiteit Gent
prof. dr. ir. Roel Baets (promotor)	Universiteit Gent
prof. dr. ir. Günther Roelkens (promotor)	Universiteit Gent
prof. dr. ir. Dries Van Thourhout (secretaris)	Universiteit Gent
prof. dr. ir. Bart Kuyken	Universiteit Gent
prof. dr. ir. Kristiaan Neyts	Universiteit Gent
prof. dr. Frans Harren	Radboud Universiteit
dr. Peter Offermans	Holst Centre, imec-NL

Universiteit Gent
Faculteit Ingenieurswetenschappen en Architectuur

Vakgroep Informatietechnologie
Technologiepark-Zwijnaarde 126, 9050 Gent, België

Proefschrift tot het behalen van de graad
Doctor in de ingenieurswetenschappen:
Fotonica
Academiejaar 2019-2020

Dankwoord

'T is gebakken ! Dit zijn woorden die mijn leerkracht Wiskunde vaak gebruikte om ons te wijzen op een *pointe* van een wiskundige afleiding. Ik ben er zeker van dat de combinatie van het **onuitputtelijke** enthousiasme en authentieke West-Vloamse tongval er toe geleid heeft dat ik dit hier nu kan neerpennen. Zwoane, bedankt voor al uw lessen en inspiratiemomenten die nog lang zullen nazinderen!
Een doctoraat verdedigen, dit kan je niet alleen. Ik wil graag mijn promotoren Roel en Günther bedanken. Roel, de UGent mag zeer trots zijn dat ze een professor hebben die op een dusdanig positieve manier studenten en medewerkers kan inspireren en motiveren. U leert ons om vooruit te denken en te durven dromen, bedankt om mij te steunen. Günther, het is altijd een plezier om met u samen te werken. U levert ongelooflijk nuttige feedback om het onderzoek in goede banen te leiden en bent altijd enthousiast, doch kritisch, om nieuwe ideeën te bespreken. Ik ben er van overtuigd dat zonder uw mentorschap er veel doctoraatstudenten het veel moeilijker zouden hebben, mij incluis.

Ik wil ook de andere professoren van de Photonics Research Group bedanken. Peter, voor de koffiepauzes en scherpe groupmeeting grappen. Wim, *soms* voor de moppen, maar vooral om ons te laten zien hoeveel werk een mens kan verzetten met een ijzersterke *work-ethic* en lean management skillz. Geert, om het labo in goede banen te leiden. Bart, voor de vele gesprekken, moppen, crazy lab-tricks, speculaties en *whodunnit* intriges. Nicolas, om ons te laten zien dat een prof wel degelijk nog research kan doen in het labo, zelfs 's nachts. Dries, voor de directe, no-nonsense aanpak van zaken. Stephane, voor de leuke quantum inzichten.
I would like to thank my crazy office mates Umar, Floris and Chonghuai for the parties, big and small, and for always being there for me, at least during the time when I was actually in the office...
Nuria, Michael and Jasper, you deserve a special thanks for all the help in the lab, you all bailed me out on numerous occasions. I would like to thank dr Dhooore, dr Mixwell, Kasper and Alejandro in Par-Ti-Cu-Lar! You guys are amazing, hope you can always chase your dreams whilst salsa-dancing

till you drop. Thank you for being part of my PhD adventure and beyond. Andres, thank you for the party-spirit! Sarvagya, you little promiscuous Indian, thank you for all the jokes. Bendix, for being a math-magician and the most (re)-productive PhD Student. Alfonso, the real slim shady, I miss you here in Ghent, hope you will find true happiness. Thank you so much for introducing me to the wonderful region of Amalfi, give my regards to Isabella! Fabio, thank you for your enthusiasm, hope we will catch up some day in Turin, congrats again on your long overdue CNRS position and good luck with the girls at home! Giorgio, Joris, Orges, Peter and Olivier for always being supportive, hope we will accomplish great things together! Jesper, may the Norse gods stand by you on your new adventures and guide you to the optomechanical Valhalla. Jeroen Allaert, for being the electronics guru. Aditya, you have been so helpful to me in my starting days, I owe you big time. Hope we will be able to catch up in person soon! Enjoy the nice weather in UCSB. Ruijun, for your help and your Lazers. Muneeb, for being the uncrowned mid-infrared godfather to all of us! Start writing! You too Bahawal and Jing!

Thanks Thomas, for the unforgettable San Francisco mini-tour. Herr Lukas, for being a hip gentleman. Commie Lukas, for pushing politics to where it matters, please don't stop. Ashim, for pushing the boundaries of what a PhD student can and/or should do. You are an inspiration to us on so many different levels, best of luck in Phutung, you're doing great! Jeroen, for questioning the supremacy of the nitride platform. Ashwyn, for being a great and honest guy. Jan-Willem, for the parties and business inspiration. Andreas and Sarah, one of the many photonics power couples, it's always nice to chat with you and to gossip about our kids. Ananth and Kamal, for being so fun and enthusiastic. Sulakshna and Saurav, for your persistence in the lab. You are an inspiration to us all. Amin and Leili, for keeping the spirits high. Daan, thanks for being the uncrowned king of extraordinary polls, these are dark days ahead of us without them. Eva, for all the help with TechTransfer and IP. Mahmoud, thanks for being the joyous spirit in our group. Are you measuring ?!? Xiaomin, for believing in science!
Xiaoning, may the FTIR work for you just once. Utsav, for the amazing CLEO conference. Haolan, for always keeping your cool. Grigorij, for keeping the Eastern-Europe vibe high. Abdul, my love, thanks for being a beacon of reason, scepticism and realism in the photonic turmoil. Irfan, for always being ready to toss a joke out your sleeve. Francois, thanks for helping out in the lab (ages ago). Maximilien, Alessio and Alexandros for the deep and at times weird philosophical discussions. Raphael, for the interesting science discussions, wish you all the best in US. Koen, good luck on your US journey as well.
I would also like to thank all other doctoral and postdoctoral researchers of the Photonics Research Group, in no particular order: Xiangfeng, Laurens ($\times 2$), Stijn ($\times 3$), Hong, Emmanuel, Artur, Camiel, Andrew, Nayyera,

Isaac, Chupao, Zuyang, Cenk, Sanja, Khannan, Antonio, Ivo, Paul, Nina, Jochem, Mattias, Giuseppe, Alexandre, Suzanne, Ewoud, Mi, Yufei, Javad, Tom, Nicolas, Yinghao, Iman, Wousty, Danae, Thijs, Ali, Banafsheh, Naidi, Joan, Yanlu, Ana, Christos, Zheng, Emiel, John George, Herbert, Sam, Pieter, Weiqiang
Liesbet, bedankt voor alle SEM-sessies en de leuke gesprekken. Steven, ik hoop dat je nooit op pensioen wilt gaan omdat anders de CR stilvalt. Bedankt voor alle hulp. Ilse V., Ilse M. en Bert, bedankt voor alle administratieve hulp en de leuke gesprekken. Kristien, bedankt om mij af en toe uit de nood te helpen.

Een doctoraat afronden zou natuurlijk niet gelukt zijn zonder de steun van vele vrienden en familie. Een speciale dank gaat naar de leden van de vzw U.N.E.: Alexander, Gert-Jan, Jeffrey, Lieven, Michiel, Pieter, Simon H, Simon L, Thibaut en Tim! Uiteraard is een speciale vermelding voor mijn ouders op zijn plaats. Papa en mama, dank jullie voor de warmte en absolute steun bij alles wat ik onderneem. Igor, een betere broer had ik me niet kunnen wensen! Een welgeemende merci naar mijn naaste familie: Sasha, Floor, Freek, Rosi en Kris.
Op dit moment staan wij aan de vooravond van een pandemie die ons manier van leven en werken fundamenteel zal veranderen. Ik wil alle zorgverleners van harte bedanken voor hun strijd.

Ten slotte dank ik graag mijn twee kleine schatjes Rozanne en Emmylou en de liefde van mijn leven Fanny. Liefste Fannytje, jou leren kennen was ongetwijfeld de belangrijkste gebeurtenis van de eeuw. Op naar nieuwe avonturen!

Bredene, maart 2020
Anton Vasiliev

Table of Contents

List of Figures

List of Tables

List of Acronyms

A

ADC	Analog-to-Digital Converter
ADF	Add-Drop Filter
AI	Artificial Intelligence
AFF	Asymmetric Fano Filter
APF	All Pass Filter
AR	Anti-Reflective
AWG	Arrayed Waveguide Grating

B

BET	Brunauer–Emmett–Teller theory
BCB	BenzoCycloButene
BOX	Buried OXide
BT	BuTterfly

C

COK	Centrum voor Oppervlaktechemie en Katalyse
CMOS	Complementary Metal-Oxide Semiconductor
CW	Continuous Wave

D

DAC	Digital-to-Analog Converter
DBR	Distributed Bragg Grating

DFB	Distributed FeedBack
DFT	Discrete Fourier Transform
dFTIR	Digital Fourier Transform InfraRed
DR	Dynamic Range
DRIE	Deep Reactive Ion Etching

E

EC	External-Cavity

F

FP	Fabry-Perot
FFT	Fast Fourier Transform
FSR	Free Spectral Range
FTIR	Fourier Transform InfraRed spectrometer
FWHM	Full Width at Half-Maximum

G

GC	Gas Chromatography (depending on context)
GC	Grating Coupler (depending on context)
GHG	GreenHouse Gas
GP	General Practitioner
GWP	Global Warming Potential

H

HDMS	HexaMethylDiSilazane
HVAC	Heat, Ventilation and Air Conditioning

I

IL	Insertion Loss

IoT	Internet of Things
IR	InfraRed
IRRAS	InfRared Reflection Aborption Spectroscopy

L

LASSO	Least Absolute Shrinkage and Selection Operator
LED	Light Emitting Diode
LIA	Lock-In Amplifier
LN	Liquid Nitrogen
LOD	Limit of Detection
LSP	Localized Surface Plasmon
LSQR	Least-SQuaRes
LWIR	Long-Wave InfraRed (8-12 μm)

M

MAP	Modified Atmosphere Packaging
MCT	Mercury-Cadmium-Telluride
MEMS	Micro-ElectroMechanical System
MIR	Mid-InfraRed (2-20 μm)
MOF	Metal-Organic-Frameworks
MOS	Metal Oxide Semiconductors
MRR	MicroRing Resonator
MWIR	Mid-Wave InfraRed (3-5 μm)
MZI	Mach-Zehnder Interferometer
MZM	Mach-Zehnder Modulator

N

NEA	Noise Equivalent Absorbance
NEP	Noise Equivalent Power
NNEA	Normalized Noise Equivalent Absorbance
NEMS	Nano-ElectroMechanical System
NIR	Near-InfraRed (1-2 μm)

O

OPD	Optical Path Difference
OPO	Optical Parametric Oscillator
OSA	Optical Spectrum Analyzer

P

PAS	PhotoAcoustic Spectroscopy
PCB	Printed Circuit Board
PCG	Planar Concave Grating
PD	PhotoDiode
PDMS	PolyDiMethylSiloxane
PIC	Photonic Integrated Circuit
PPB	Parts-per-Billion, 1 part in 10^9
PPM	Parts-per-Million, 1 part in 10^6
PPT	Parts-per-Trillion, 1 part in 10^{12}
PTS	PhotoThermal Spectroscopy

Q

QCL	Quantum Cascade Laser
QEPAS	Quartz-Enhanced PhotoAcoustic Spectroscopy
Q-factor	Quality Factor

R

RH	Relative Humidity
RMSE	Root-Mean Square Error

S

SAW	Surface Acoustic Wave
SEIRA	Surface Enhanced InfraRed Absorption
SERS	Surface Enhanced Raman Spectroscopy

SHS	Spatial Heterodyne Spectrometer
SNR	Signal to Noise Ratio
SOI	Silicon-on-Insulator
SPGL	Spectral Projected-Gradient aLgorithm
SPP	Surface Plasmon Polariton
SWaP-C	Size, Weight, Power and Cost
SWIR	Short-Wave InfraRed (typically 1-2.5 μm wavelength range)

T

TDLAS	Tunable Diode Laser Absorption Spectroscopy
TIA	Trans-Impedance Amplifier
TMA	Tri-MethylAmine
TO	Transistor Outline

U

USB	Universal Serial Bus

V

VIS	VISible (typically 0.4-0.8 μm wavelength range)
VOC	Volatile Organic Compound

W

WDM	Wavelength (De)Multiplexing
WMS	Wavelength Modulation Spectroscopy

X

XT	Cross-Talk

Nederlandse samenvatting –Summary in Dutch–

Het waarnemen van kleine concentraties aan gasmolecules is van groot belang in veel toepassingen. Dit varieërt van het monitoren van luchtkwaliteit in huizen en wagens, detectie van uitlaatgassen in industriële processen, tot het analyseren van de uitgeademde lucht van patiënten om indicatoren op te sporen voor bepaalde ziektes. In het bijzonder, met het oog op het wereldwijd probleem van voedselverspilling, is er slimme verpakking nodig die de staat van het voedsel en de verpakking kan accuraat weergeven. Deze informatie zou het mogelijk maken om de werkelijke houdbaarheid van veel producten nauwkeuriger te bepalen, die op heden onmiddellijk na de vervaldatum worden weggegooid, zelfs wanneer die nog niet bedorven is.

Momenteel zijn verschillende methodes voorhanden om dergelijke kleine concentraties te meten, met name electrochemische, katalytische en spectroscopische technieken. Spectroscopische sensoren zijn vaak opvallend beter op gebied van nauwkeurigheid, sensor levensduur en gevoeligheid. De analyse is gebaseerd op de meting van het 'vingerafdruk'-absorptiespectrum van het gasmonster in het midden-infrarood golflengtebereik. De systemen die tegenwoordig beschikbaar zijn, al worden hiermee uitstekende prestaties geleverd, zijn omslachtig, duur en verbruiken erg veel energie. Het doel van dit doctoraat is om de technologie van vandaag te verbeteren richting goedkope, compacte en energiezuinige geïntegreerde spectroscopische sensoren op basis van silicium chiptechnologie. De kleine voetafdruk (mm^2) van dergelijke mini-sensoren beperkt echter de interactielengte van het infraroodlicht met het gas. Daarom werden verschillende technieken onderzocht om de gevoeligheid te verhogen, waaronder het gebruik van concentratieverhogende coatings op de silicium golfgeleidercircuits alsook het toepassen van innovatieve spectroscopietechnieken, zoals fotothermische spectroscopie. De miniaturisatie van performante, maar goedkope mid-infrarood spectrometers op de sensorchip werd ook nader onderzocht.

Volledig geïntegreerde miniatuur spectroscopische sensoren hebben een gecalibreerde optische bron nodig op de chip. In deze context werd een nieuwe, digitale FTIR architectuur geïmplementeerd op een fotonische chip die slim gebruik maakt van optische schakelaars. Dit maakt het mogelijk om de golflengte van een geïntegreerde laser te monitoren op de chip. Het gefabriceerde apparaat heeft een nauwkeurigheid van 100 pm over een golf-

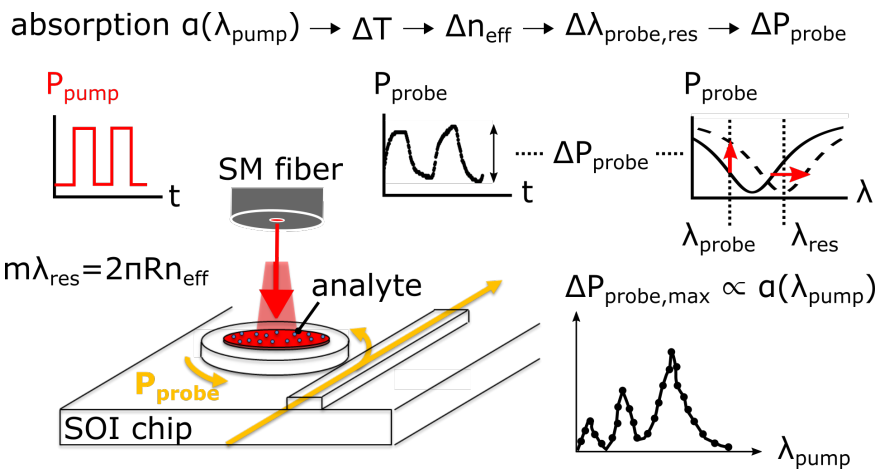

Figuur 1: De warmte die wordt gegenereerd door molecuul-specifieke absorptie van het midden-infrarood licht (pomp) verhoogt de temperatuur van de ringresonator die uiterst gevoelig wordt afgelezen met behulp van een nabij-infrarood lasersysteem (probe). Het absorptiespectrum van het monster wordt bekomen door de golflengte van de pomp te scannen en de maximale modulatie van de probe te registreren.

lengtebereik van 130 nm in het golflengtebereik van 2.3 µm.

Geïntegreerde fotothermische spectroscopie

Het detectieprincipe is uiteengezet in Figuur 1. Het monster (analyte) wordt afgezet in het ringvormige gebied van de microring-resonator (MRR). Voor spoorgas-detectie toepassingen is de MRR gecoat met een poreuze coating om de gasmoleculen efficiënt te vangen en de concentratiedichtheid lokaal te verhogen. Een nabij-infrarood uitlees-laser (probe) is gekoppeld aan de MRR met een golflengte λ_{probe} die afgestemd is op het werkpunt waar de optische transmissie $\mathcal{T}$ maximale helling $d\mathcal{T}/d\lambda = \mathcal{T}'$ heeft. De golflengte-selectieve absorptie van het mid-infrarood licht (pomp) door het monster geeft aanleiding tot een golflengte-selectieve temperatuurstijging $\Delta T(\lambda_{pump})$ van de MRR. Deze verandering wordt vervolgens uitgelezen met behulp van een zeer gevoelig nabij-infrarood lasersysteem (probe) gekoppeld aan de MRR. Het absorptiespectrum van het monster wordt gereconstrueerd door de golflengte van de pomp te scannen en de maximale modulatie van de probe te registreren.

Het fotothermisch signaal kan worden versterkt door de MRR vrijhangend te fabriceren op een dunne membraan, waardoor de ringgolfgeleider thermisch wordt geïsoleerd van het substraat. De resulterende effectieve thermische weerstand wordt twee grootte-ordes verhoogd tot 1.2×10^4 K/W.

Deze samples resulteerden in een genormaliseerde ruis-equivalente absorptie (NNEA) van $7.6 \times 10^{-6} cm^{-1} W/Hz^{1/2}$ voor 0.5 µW optisch vermogen van de probe. Voor een optisch pomp vermogen van 50 mW en 1 Hz meetbandbreedte wordt een detectielimiet (LOD) α_{min} van $1.5 \times 10^{-4} cm^{-1}$ voorspeld. Dit geeft aan dat, gecombineerd met gas-adsorberende coatings, geïntegreerde sub-ppm-detectie van sporengassen mogelijk is.

Een gas-adsorberende, mesoporeuze siliciumdioxide coating werd aangebracht op de MRRs. Sub-ppm detectielimiet-waarden werden verwacht voor sporengassen in het golflengtebereik van $3-4\mu m$, met initiële resultaten voor tolueen-gas. De huidige sensor-gevoeligheid is echter sterk beperkt omdat het signaal overschaduwd wordt door de optische achtergrond-absorptie van de coatingmatrix en de hydrofobe laag.

Midden-infrarood AWG spectrometer

Spectroscopie van complexe gasmoleculen of vloeistoffen wordt typisch uitgevoerd met behulp van een breedbandige lichtbron in combinatie met een gevoelige spectrometer die het spectrum analyseert nadat het licht door het sample of monster is gegaan. Verder, in een volledig geïntegreerd systeem kan een siliciumgolfgeleider, al dan niet gecoat met een gasadsorberende laag, dienst doen als een geïntegreerde optische 'gascel' waarbij een fractie van het licht evanescent interageert met het gas op de chip. Verschillende silicium-spectrometers operationeel in het midden-infrarood golflengtebereik zijn reeds aangetoond, maar op heden is er nog geen goedkope oplossing voor de integratie van een performante midden-infrarood fotodetectormatrix. Om dit aan te pakken, werd een hybride Arrayed Waveguide Grating (AWG) midden-infrarood spectrometer ontwikkeld, die slechts een enkele pixeldetector nodig heeft in plaats van een detector-matrix. De uitgangen van de AWG belichten een hoog-performante fotodetector. Het multiplexen van de verschillende golflengtekanalen gebeurt door elke uitgangsarm in de tijd te moduleren. Een demonstratie is gegeven in Figuur 2 waarbij een AWG-spectrometer in het golflengtebereik 2.3 µm gecombineerd wordt met slechts een midden-infrarood fotodiode. De AWG heeft twaalf uitgangskanalen met een spatiëring van 225 GHz (4 nm) en een vrij spectraal bereik (FSR) van 3150 GHz (56 nm). De uitgangen worden tegelijkertijd verzameld door een enkele, verpakte InGaAs PIN fotodiode. De respons van elk AWG-kanaal wordt gediscrimineerd door het optisch vermogen in ieder kanaal sequentieel te moduleren in de tijd met behulp van geïntegreerde Mach-Zehnder-gebaseerde (MZM) thermo-optische modulatoren met een π-fase verschuivingsverbruik van $\approx$ 50 mW. Ter illustratie werd het absorptiespectrum van een 0.5 mm dikke polydimethylsiloxaanplaat (PDMS) bepaald en vergeleken met een referentie-meting met een standaard optische spectrometer. De eerste stappen werden gezet voor verdere integratie in het MWIR-golflengtebereik rond 3.3 µm, waarbij de chip

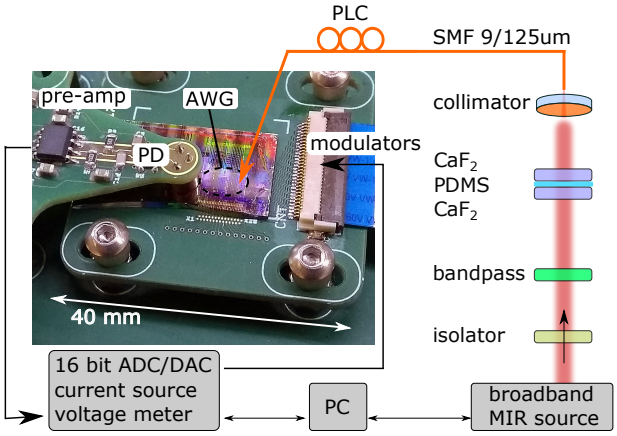

Figuur 2: Schema van een AWG-spectrometer die gebruik maakt van een enkele externe detector (a). Een breedbandige midden-infrarood lichtbron verlicht een 0.5 mm dikke PDMS-plaat. Na interactie wordt het licht gekoppeld aan de AWG en verzamelt de PD tegelijkertijd alle twaalf spectrale uitgangskanalen.

mede wordt geïntegreerd bovenop een standaard 'vlinder'-verpakte fotodiode (butterfly package). Er werd een ontwerp voorgesteld dat in staat is om CH_4 te detecteren rond 3.3 µm in het bereik van 10-100 ppm met behulp van een 12-kanaals 50 GHz AWG, zie ook Figuur 3 (a). Een compacte, volledig geïntegreerde spectrometer-op-een-verpakking wordt voorgesteld in Figuur 3 (b). De mid-infrarood breedbandige lichtbron, detector en spectrometer, zitten allemaal in één verpakking. De chip fungeert bovendien als deksel voor de verpakking en het is mogelijk om geïntegreerde micro-lenzen te fabriceren aan de achterkant van de chip om het licht van de chip van/naar de bron/detector te focusen. De voorgestelde integratie is een mogelijke route voor draagbare spectrometertoepassingen in het midden-infrarood golflengtebereik.

Digitale FTIR golflengte monitor

Het werkingsprincipe van de dFTIR-spectrometer is vergelijkbaar met een FTIR zonder bewegende elementen. Het kernelement is een Mach-Zehnder-interferometer (MZI) met een sinusoïdaal golflengterespons waarbij de sinusfrequentie een stijgende functie is van het optisch padlengteverschil (OPD) tussen de twee armen. Een interferogram wordt gevormd door de fotodioderespons op te nemen voor elke OPD-combinatie.
De cosinus Fourier-transformatie van het interferogram levert het (onbekend) initiëel licht-spectrum op. De OPD in de dFTIR-architectuur wordt bepaald door het licht door verschillende schakelaar-combinaties te sturen. Het belangrijkste principe hierbij is dat de verschillende optische paden her-

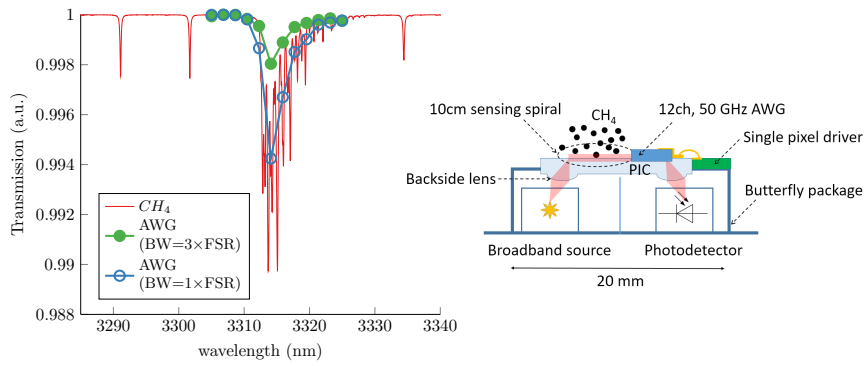

(a) (b)

Figuur 3: Simulatie van een 12-kanaals, 50 GHz AWG met één pixel voor methaandetectie bij 3.3 µm (a). De CH_4-concentratie is 100 ppm en de effectieve optische padlengte is 2.83 cm. De methaanlijn is nog steeds duidelijk discrimineerbaar, zelfs als de bandbreedte van de lichtbron de FSR van de AWG overschrijdt. Schema van een compacte, volledig geïntegreerde spectrometer-op-een-verpakking wordt getoond (b). De voorgestelde midden-infrarood lichtbron, detector en spectrometer, zijn allemaal opgenomen in één 'vlinder'-verpakking.

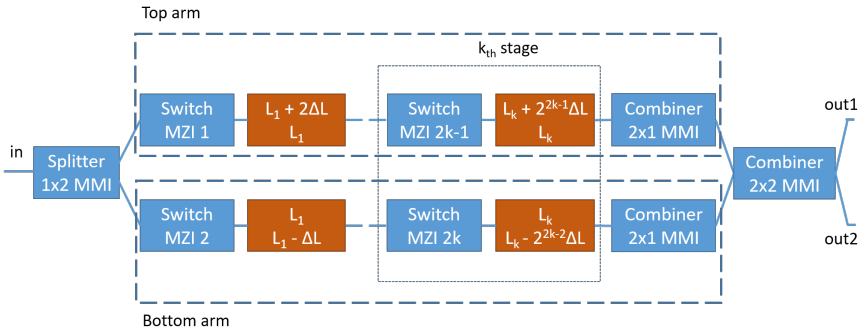

Figuur 4: Schema van het digitaal FTIR-ontwerp. De spectrometer is een herconfigureerbare MZI, bestaande uit een totaal van k schakelaars in de 'bovenste' en 'onderste' arm, zodat elke combinatie resulteert in een uniek optisch padlengteverschil (OPD) tussen de twee armen. In dit geval is de OPD exponentieel (basis 2) verdeeld over 2^k waarden.

gebruikt worden voor elke configuratie, wat een plaatsbesparing oplevert en de de totale grootte van het apparaat verkleint ten koste van de totale meettijd, zie ook Figuur 4.

Het gefabriceerd optisch circuit van de dFTIR heeft imperfecties, de schakeling tussen de verschillende toestanden gebeurt onvolledig. Daarnaast

zijn er verlies- en dispersie-effecten die het gebruik van de eenvoudige cosinus Fourier-transformatie verbieden. In plaats van Fourier-transformaties werden kleinste kwadraat (LSQR) en 'dunne-matrix' benaderingsalgoritmen (LASSO) gebruikt om het onbekende spectrum te bekomen. Een dFTIR-chip, werkend rond 2.3 µm, werd vervaardigd in het 400 nm SOI golfgeleider-platform met geïntegreerde thermo-optische schakelaars. In de 'dunne'-matrix benadering kan dit chip gebruikt worden als een precieze (100 pm) golflengtemeter over een bandbreedte van 130 nm. De spectrale reconstructie van een onbekend laser-spectrum wordt getoond in Figuur 5. De resultaten worden vergeleken met een standaard, commercieel optisch spectrometer. De onbekende lasergolflengte werd bepaald door telkens het globaal maximum in het spectrum te nemen. Zowel LSQR- als LASSO-algoritmen kunnen de piekgolflengte nauwkeurig bepalen binnen de operationele bandbreedte. Bovendien werd er aangetoond dat het mogelijk is om

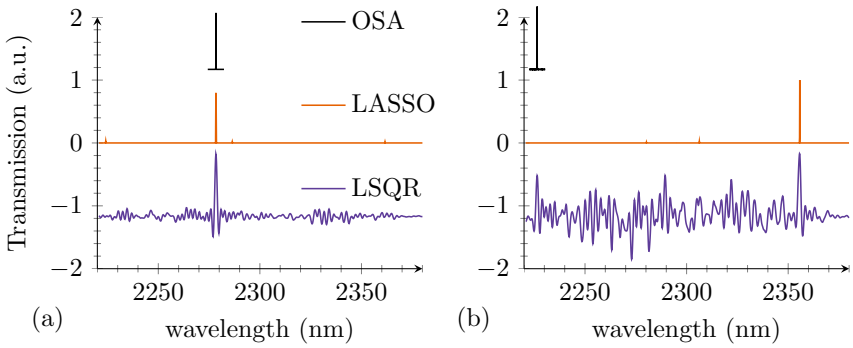

Figuur 5: Resultaten van gefabriceerd dFTIR chip die aangewend wordt om de golflengte van een onbekende laser-invoer te bepalen. De resultaten worden vergeleken met een standaard spectrometer (OSA). Het globaal maximum wordt gebruikt om de lasergolflengte te bepalen. Zowel LSQR- als LASSO-algoritmen kunnen de piekgolflengte nauwkeurig binnen de bandbreedte bepalen (a). Een aliaseffect treedt op wanneer de lasergolflengte buiten de operationele bandbreedte van de dFTIR ligt (b). De genormaliseerde spectra zijn voor de duidelijkheid verticaal verschoven.

twee naburige spectrale lijnen, met een spatiëring van 500 pm, van elkaar te onderscheiden. Dit kan handig zijn voor het identificeren van 'modesprongen' bij geïntegreerde laserbronnen.

Conclusies

Het gebruik van gas-adsorberende coatings en fotothermische spectroscopie op een fotonische chip werd ontwikkeld en geanalyseerd. Eerste demos geven aan dat sub-ppm detectie van sporengassen inderdaad mogelijk moet zijn

met deze methode. De bijkomende achtergrond-absorptie van beschikbare coatings beperkt echter de huidige detectieniveaus aanzienlijk.
Een spectrometerarchitectuur met één pixel werd gedemonstreerd, gebruikmakend van een AWG bij 2.3 μm golflengte. Dit toont aan dat het mogelijk is om één enkele gekoelde, hoog-performante fotodiode in het midden-infrarood golflengtebereik te gebruiken, in tegenstelling tot een matrix van inferieure geïntegreerde PD's. Verdere integratieroutes werden uitgelijnd met demonstratie van een AWG chip, geïntegreerd bovenop een 'vlinder'-verpakte fotodiode in het bereik van 3.3 µm. Verder werd er een geavanceerder ontwerp voorgesteld dat toelaat CH_4-gas te meten bij 3.3 µm, met als beoogd detectielimiet in het 10-100 ppm bereik. De voorgestelde integratiebenadering is een kost-efficiënte route voor toekomstige draagbare sensortoepassingen in het midden-infrarood golflengtebereik.

Een recente, op schakelaar gebaseerde, digitale FTIR architectuur werd geïmplementeerd op een SOI fotonisch circuit in het mid-infrarood golflengte bereik. De gefabriceerde chip kan gebruikt worden als een geïntegreerde golflengtemeter met een nauwkeurigheid van 100 pm over een bandbreedte van 130 nm in het SWIR golflengtebereik rond 2.3 µm. De onmiddellijke toepassing is het monitoren van de golflengte van geïntegreerde laserbronnen op dezelfde chip.

English summary

The sensing of small concentrations of gas molecules is of high importance in many applications, ranging from air quality monitoring in houses and cars, over exhaust monitoring and industrial process control, to analyzing the exhaled breath of patients to look for biomarkers for particular diseases. In particular, to address the global food waste problem, intelligent packaging is required that can monitor the food package integrity and spoilage state. This added information would allow the users to more accurately determine and prolong the effective shelf-life of many products whereas now the package is discarded after the expiry date, even when the food product is not yet spoiled.

Different techniques are available today to measure such small concentrations, including electrochemical, catalytic and spectroscopic techniques. Spectroscopic approaches stand out in terms of sensor lifetime, specificity and sensitivity. The analysis is based on the measurement of the 'fingerprint' absorption spectrum of the gas sample in the mid-infrared wavelength range. Currently available systems however, while having outstanding performance, are bulky, expensive and very power hungry. The aim of this PhD is to advance the state-of-the-art towards low-cost, compact and low-power integrated spectroscopic sensors based on silicon optical chip technology. The small footprint (mm^2) of such sensors however limits the interaction length of the infrared light with the gas. Therefore, several enhancement techniques were investigated to increase the sensitivity, including the use of concentration enhancement coatings on the silicon waveguide circuits, and the use of novel spectroscopy techniques on-chip such as photothermal spectroscopy. The miniaturization of high performance, yet low-cost, mid-infrared spectrometers on the sensor chip were studied as well.
Fully integrated devices require calibrated on-chip optical laser sources. In this context, a novel digital Fourier Transform InfraRed (FTIR) architecture was implemented on an silicon photonic chip, enabling in-line monitoring of the wavelength of an integrated laser.

On-chip photothermal spectroscopy

The sensing principle is outlined in Figure 6. The analyte is deposited in the annular region of the microring resonator (MRR). For trace gas applica-

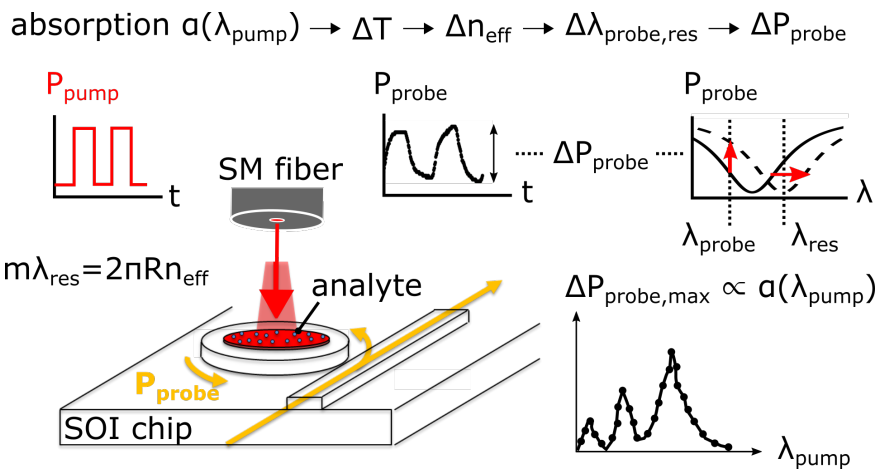

Figure 6: The heat generated through molecule-specific absorption of the mid-infrared pump beam increases the temperature of the ring resonator which is read-out sensitively using a near-infrared laser system. The absorption spectrum of the analyte is reconstructed by scanning the pump wavelength and recording the maximum probe modulation.

tions, the MRR is coated with a pre-concentrating porous coating to capture and trap the molecules. A near-infrared probe laser is coupled to the MRR and the wavelength λ_{probe} is tuned to the operation point where the the optical transmission $\mathcal{T}$ has the highest slope $d\mathcal{T}/d\lambda = \mathcal{T}'$. The wavelength selective absorption of mid-infrared radiation by the analyte gives rise to a wavelength selective temperature increase $\Delta T(\lambda_{pump})$ which is transferred to the resonator. This change is read-out sensitively using a near-infrared laser system coupled to the MRR. The absorption spectrum of the analyte is reconstructed by scanning the pump wavelength and recording the maximum probe modulation.

The photothermal signal can be increased by fabricating suspended MRR membranes, thermally isolating the ring waveguide. The resulting effective thermal resistance is estimated to be $1.2\times10^4 K/W$. The latter resulted in a normalized noise equivalent absorbtion (NNEA) of $7.6\times10^{-6} cm^{-1}W/Hz^{1/2}$ for 0.5 µW of probe power. By using a pump power of 50 mW and 1 Hz measurement bandwidth, a limit of detection (LOD) α_{min} of $1.5 \times 10^{-4} cm^{-1}$ is predicted. This indicates that sub-ppm integrated trace gas detection is possible, combined with gas adsorbing coatings.

A gas-adsorbing mesoporous silica coating was coated on the ring transducers. Sub-ppm LOD values were expected for trace gases such as toluene in the $3-4\mu m$ wavelength range. However the current sensitivity is severely limited by the background optical absorption of the coating matrix and the hydrophobic layer.

Mid-infrared single pixel AWG spectrometer

Spectroscopy of complex gas molecules or liquids is commonly performed using broadband sources which require a sensitive spectrometer to analyze the spectrum after having passed through the analyte. In a fully-integrated system, the silicon waveguide, potentially coated with a gas adsorbing layer, can act as an integrated 'gas cell'. While silicon spectrometers operating in the mid-infrared have been demonstrated, there is no low-cost solution for the integration of a high-performance mid-infrared photodetector array. To address this, a hybrid Arrayed Waveguide Grating (AWG) mid-infrared spectrometer was developed, requiring only a single pixel detector instead of a detector array. The outputs of the AWG array are illuminating a high-performance single photodetector. The multiplexing of the different wavelength channels is done by time-modulating each output arm. A demonstration is shown in Figure 7 using an AWG spectrometer in the 2.3 µm wavelength range with a high performance mid-infrared photodiode. The AWG has twelve output channels with a spacing of 225 GHz (4 nm) and a free spectral range (FSR) of 3150 GHz (56 nm), which are simultaneously collected by a single, transistor outline (TO)-packaged extended InGaAs PIN photodiode. The response of each AWG channel is discerned by time-sequentially modulating the optical power in each output channel using integrated Mach-Zehnder based (MZI) thermo-optic modulators with a π-phase shift power consumption of $\approx$ 50 mW. As an example, the absorption spectrum of a 0.5 mm thick polydimethylsiloxane sheet (PDMS) was retrieved and compared to a bench-top optical spectrum analyzer to good agreement. First steps have been taken towards integration further

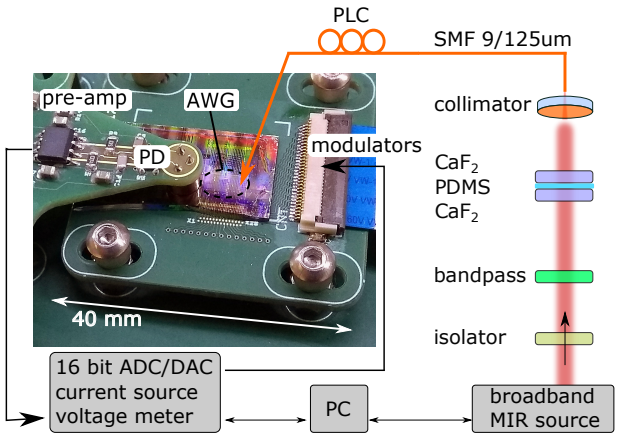

Figure 7: Schematic of an AWG spectrometer experiment using a single external detector (a). A broadband mid-infrared source illuminates a 0.5 mm thick PDMS sheet. After interaction, the light is coupled to the AWG and the PD collects all twelve spectral output channels simultaneously.

in the MWIR wavelength range at 3.3 µm, where the PIC is co-integrated on top of a butterfly packaged photodiode. A design was proposed, capable of detecting CH_4 in the 3.3 µm wavelength region in the 10-100 ppm range using a 12 channel 50 GHz AWG, see also Figure 8(a). A compact fully-integrated spectrometer-on-a-package is proposed in Figure 8(b). Th mid-infrared broadband source, detector and spectrometer, are all contained within one butterfly package. The PIC additionally acts as a lid for the package and integrated focusing lenses can be processed on the backside of the chip to couple the light to the PIC and back to the PD. The proposed integration approach is a viable route for portable spectrometer applications in the mid-infrared.

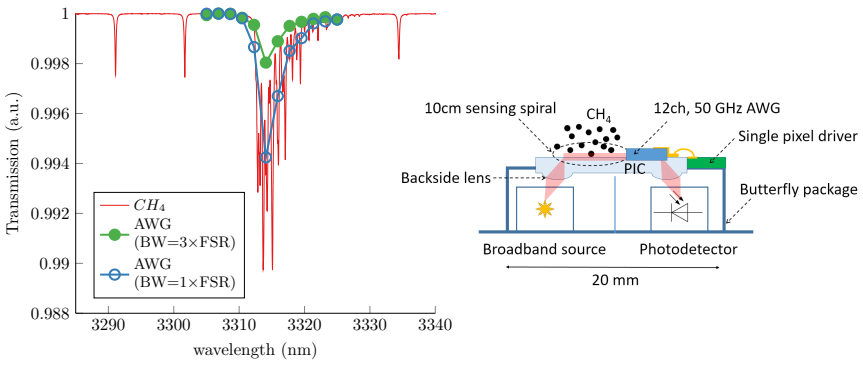

Figure 8: Simulation of a 12 channel, single pixel 50 GHz AWG response for methane detection at 3.3 µm (a). The CH_4 concentration is 100 ppm and the effective optical path length is 2.83 cm. The methane line is still clearly resolved even the broadband source bandwidth exceeds the FSR of the AWG. Schematic of a compact fully-integrated spectrometer-on-a-package is shown (b). The proposed mid-infrared broadband source, detector and spectrometer, are all contained within one butterfly package.

Digital FTIR wavelength monitor

The operation principle of the dFTIR spectrometer approach is similar to an FTIR without moving parts. The core element is a Mach-Zehnder Interferometer (MZI) which has a cosine-shaped spectral response. The cosine frequency is an increasing function of the optical path delay (OPD) between the two arms. By collecting the photodiode response for each OPD, an interferogram is formed. The cosine Fourier transform of the interferogram will yield the initial input spectrum. The OPD in the dFTIR configuration are controlled by directing the light through different switch combinations.

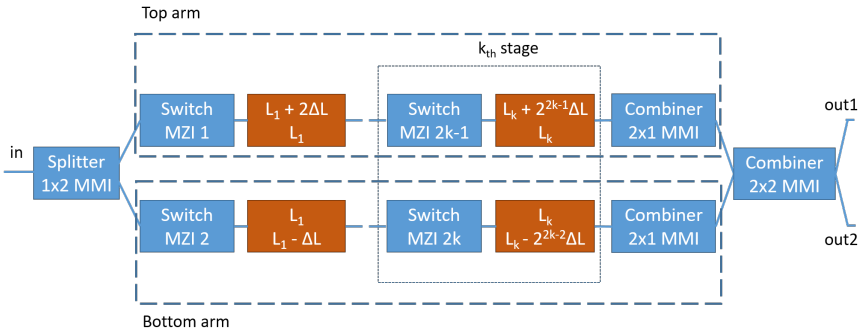

Figure 9: Schematic of the digital FTIR spectrometer design. The spectrometer is a reconfigurable MZI, consisting of a total of k switches in the 'top' and 'bottom' arm in such a way that each combination results in a unique optical path difference between the two. In this case, the OPD is exponentially (base 2) distributed over 2^k values.

The key principle is that several optical pathways are re-used for each configuration, yielding a reduction in overall size of the device at the expense of total measurement time, see also Figure 9.

The fabricated dFTIR device features imperfections, non-perfect switching states, loss and dispersion effects which prohibit the use of the simple cosine Fourier transform to recover the spectrum. Instead, least-square (LSQR) and sparse approximation algorithms (LASSO) are used to recover the unknown spectrum, given that the dFTIR is characterized a-priori. A dFTIR device, operating at 2.3 µm was fabricated in the 400 nm waveguide SOI platform with integrated thermo-optic switches. In the sparse approximation, this dFTIR device can be used as an accurate (100 pm) wavelength meter with an alias-free range span of 130 nm. The spectral retrieval for an unknown laser input is shown in Figure 10 and compared to a bench-top optical spectrum analyzer (OSA). The global maximum is used to assert the unknown laser wavelength. Both LSQR and LASSO algorithms can recover the peak wavelength accurately within the operating bandwidth. Furthermore, two neighbouring spectral lines spaced 500 pm apart can be resolved using the same device. This is useful for identifying 'mode-hopping' operation of integrated silicon photonics laser sources.

Conclusions

In conclusion, the use of gas adsorbing coatings and on-chip photothermal spectroscopy was analyzed and developed. A proof-of-concept demonstration indicates that sub-ppm detection is indeed possible with this method. However, the absorbance of the available pre-concentration coatings are

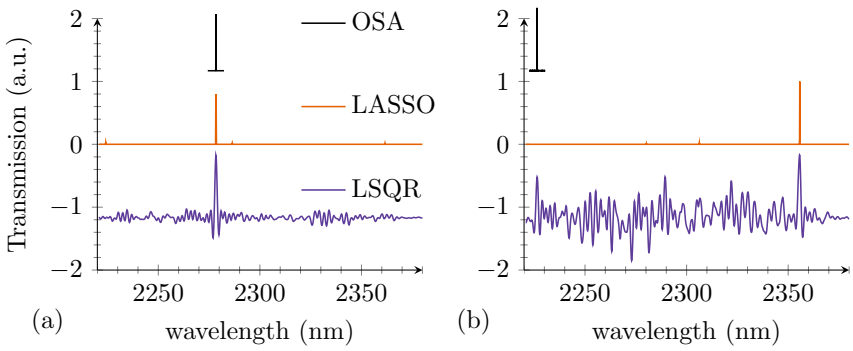

Figure 10: dFTIR device used to recover an unknown laser input compared to an OSA. The global maximum is used to assert the laser wavelength. Both LSQR and LASSO algorithms can recover the peak wavelength accurately within the operating bandwidth (a). Aliasing occurs when the laser wavelength is outside of the operating bandwidth of the device (b). The normalized spectra are shifted vertically for clarity.

severely limiting the current performance. A single pixel spectrometer architecture was demonstrated with a 2.3 µm AWG. This permits using a single cooled, high-performance photodiode in the mid-infrared wavelength range as opposed to an array of inferior integrated PDs. Further integration on top of a butterfly packaged photodiode in the 3.3 µm range was demonstrated and a more advanced design was proposed, capable of detecting CH_4-gas in the 3.3 µm wavelength region in the 10-100 ppm range. The proposed integration approach is a viable low-cost direction for handheld spectroscopy applications in the mid-infrared wavelength region.

A novel switch-based, digital FTIR-based architecture was implemented on a SOI photonic circuit. The fabricated device shows an accuracy of 100 pm over a wavelength span of 130 nm in the 2.3 µm wavelength range and is readily implemented for on-chip laser source wavelength monitoring applications.

1 Introduction

In this introductory chapter, the context and the socio-economic drivers behind this PhD thesis on miniaturized spectroscopic optical gas sensors are given. The potential for greenhouse gas emission reduction through mitigation of food waste with intelligent packaging is elucidated. Possible applications for other industries such as industrial gas leak monitoring, gas process compositional analysis and personal health monitoring are given that can greatly benefit from research in this domain. An overview of the state-of-the art technologies is given together with an outline of the thesis.

Contents

1.1 Greenhouse gas emission reduction

Climate change is at our doorstep and innovation in technology is one of the key solutions to counteract it. Whenever people mention green technology,

the first elements that come to mind are renewable energy sources: wind turbines and solar panels. However, it is important to realize that innovation in renewables and replacement of fossil fuel energy sources alone is insufficient to solve the global climate crisis [1]. In fact, the current world production of electricity through fossil fuels each year is only responsible for 25% of the global greenhouse gas (GHG) emissions [2]. To curb the global warming, it is therefore crucial to innovate in other sectors just as vigorously. The Agriculture sector is estimated to be responsible for 24% of the total GHG emissions. The main contributing factor there is the worldwide cattle population which emits methane, a potent GHG. On top of this, the deforestation in favor of crop lands leads to lower number of trees which naturally capture CO_2 from the air. Manufacturing of goods such as plastic, steel and aluminum is responsible for 21 % and the transportation sector is responsible for 14%. It is interesting to stress that electrifying the worldwide car fleet alone would not even halve the contribution of the transportation sector as the main contribution comes from the voracious consumption of diesel for planes, cargo ships and trucks [1]. Finally, 6 % is attributed to heat, ventilation and air conditioning (HVAC) of buldings, as well as energy used for cooking at home. The remaining 10% are attributed to various manipulation in the Energy sector not directly related to energy production and include fossil fuel extraction, refining, processing and transportation.

The battle against climate change therefore requires innovative solutions within each of the aforementioned domains. In what follows, it will be shown that the capability to monitor and visualize gas components with a miniature affordable sensor would be instrumental to tackle some of the aforementioned global warming challenges. Advancements in the reduction of Size, Weight, Power and Cost (SWaP-C) of these sensors, combined with inter-connectivity and advanced analytics offered by Internet-of-Things (IoT) networks are crucial for breakthrough improvements in the climate sensitive sectors that we desperately need to address today. It is the intention of this thesis to explore, analyze and further advance the field of **integrated optical sensors**, and more specifically, spectroscopic devices based on the silicon photonics waveguide platform which leverages the high-volume complementary metal-oxide semiconductor (CMOS) supply chain. The global food waste problem should be addressed through intelligent food packaging which can monitor the package integrity and food spoilage state.

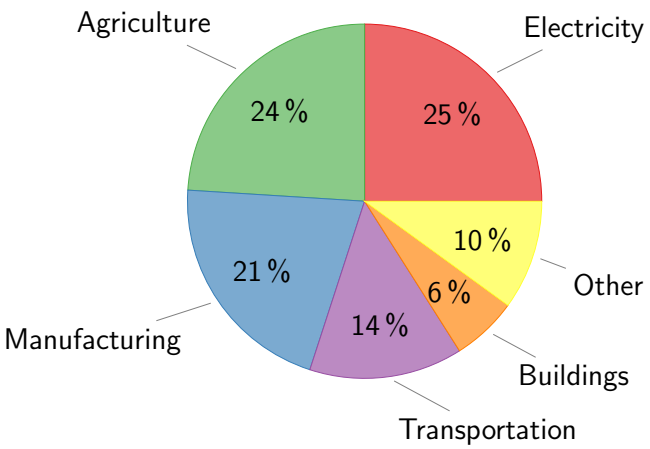

Figure 1.1: Global greenhouse gas emissions by sector, based on [2].

1.1.1 CheckPack: intelligent packaging

In order to feed the ever-growing number world population it is essential to improve our efficiency in how we grow and transport food. A great opportunity and at the same time a great challenge exists to reduce GHG emissions in the agriculture sector by minimizing the food loss/spoilage in the food supply chain. A decrease in the food loss would decrease the required crop/livestock land area, therefore directly reducing the GHG emissions. There is still a lot of room for improvement as an estimated one third of all food products worldwide is lost or wasted every year [3]. The land area necessary to produce this waste is equivalent to 450 times the surface of Belgium and requires over 250 km^3 water. On top of this, additional GHG gases are released due to either the decomposition of discarded products on landfills (methane) or released into the atmosphere after incineration (black carbon).
In western countries, most waste occurs either just after harvest or at the time of consumption (mealtime). For example in the U.S.A, up to one quarter of all fruits and vegetables are lost to poor temperature control during storage and transport [4]. There are several opportunities to dramatically reduce the food spoilage across the whole food supply chain which would dramatically reduce the greenhouse gas emissions in the process.
One direction to address this issue is through intelligent packaging. **Check-**

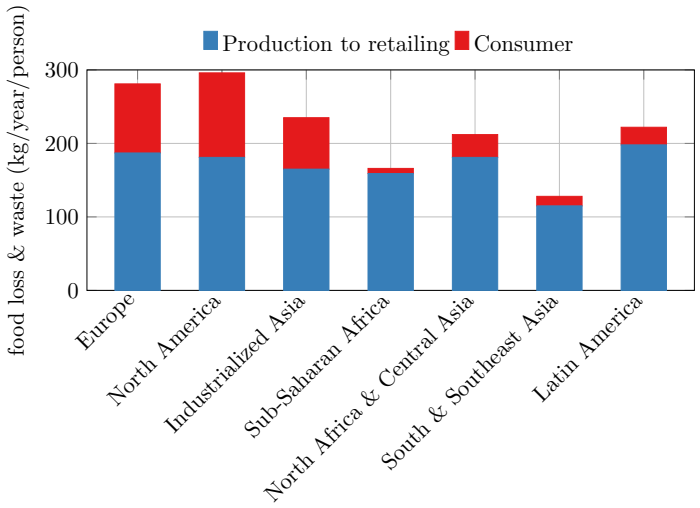

Figure 1.2: Per capita food losses and waste at consumption and pre-consumption stages; Blue: food loss between production and retailing; Red: food waste from consumers [5]

Pack[1] is a multidisciplinary research project aiming to develop an optical 'nose' for intelligent packaging to reduce food waste by monitoring the spoilage state and package integrity. This added information would allow users to more accurately determine and prolong the effective shelf-life of many products whereas now the package is discarded after the expiry date, even when the food product is not yet spoiled. The introduction of the expiration date has had an impact on the amount of food that is wasted. In the framework of the CheckPack project, a Belgian questionnaire with 904 participants indicated that people throw away food for two main reasons. Reason one (74%) being the perceived freshness/quality of the food is not as expected and reason two (55%) the expiration date method. High quality standards and the current use of the expiration date technique for products are the leading reasons why food products are thrown away in more developed countries. However, not all products that have passed their shelf-life label are meant to be discarded. The existence of two different types of shelf-life labels has led to more confusion with the consumers. The two labels are indicated as 'best before' and 'use by'. The 'best before' date is the date of minimal shelf-life of a food product to which the food pertains its advertised, specific properties (such as crispiness of chips) when stored

[1] CheckPack: integrated optical sensors in food packaging to simultaneously detect early-spoilage and check package integrity, project nr. IWT-SBO-130036

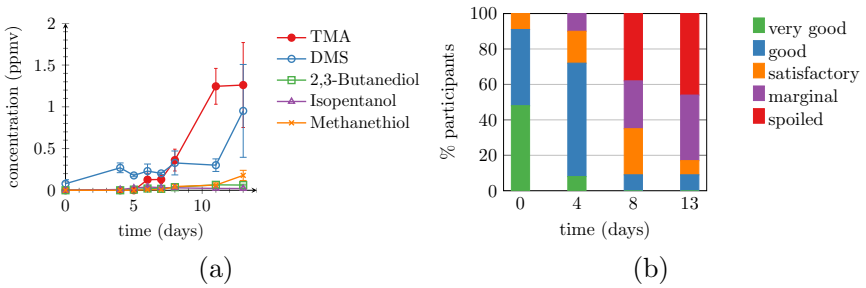

Figure 1.3: VOC analysis of cod-fish packaged under modified atmosphere (a). Only a fraction of total number of VOCs is shown. The concentration of tri-methylamine (TMA) rises quickly inside the package over time and is a good indicator to track. Results of professional food panel assessing the freshness of packaged cod-fish (b).

in an adequate way. The 'use by' date specifies the date after which there is an immediate hazard for human health when the product is consumed. The latter date is based on a series of experimental tests, but a safety margin is calculated to take different uncontrollable factors into account such as the variety of products, geographic location and temperature variations during transport and storage. Unfortunately, there is a portion of the general public who erroneously treats the 'best before' date as an indicator to throw away the food product, even though there is no immediate hazard. A better, intelligent packaging system would therefore (1) ideally take into account the actual shelf-life conditions (e.g. temperature during transport and storage), (2) provide tighter expiration dates by monitoring the actual state of the packaged food by analyzing the packaged headspace environment and (3) provide clear, unambiguous information to the retailer or consumer.

Perishable food such as fresh fish and meat in the supermarkets is almost always packaged under a Modified Atmosphere (MAP). Typically, oxygen (O_2) in the air is replaced by a large concentration of nitrogen (N_2) and/or carbon dioxide (CO_2) with total volume concentrations ranging between 20-100%. This allows the inhibition of microbial growth and greatly extends the expiration date up to two weeks. Over time, food products naturally produce distinct gas emissions, volatile organic compounds (VOCs), when deteriorating due to the presence of a specific microbial footprint. When the package is opened, our human nose can, to some extent, determine the spoilage stage of the product withing. For instance, spoiled fish will have a distinct ammonia-like odor. The spoilage of each food product type has a natural variety in microbial composition which results in a unique time-evolution of the package gas-composition and concentration. The challenge

is that there is also a variability in the exact content between samples of the same type. In order to obtain an unambiguous result on the status of the food product, this natural occurring variance must be included in the data analysis of the sensor. On top of this, our own perception of food spoilage has a large variance as well. As an example, a food panel of trained food examiners was exposed to a series of different samples of cod-fish of varying spoilage state, see also Figure 1.3(b). Even when presented to an experienced food panel, the spoilage state of the sample is highly subjective to the observer.

The goals of the CheckPack project are:

- explore and identify unambiguous markers for different food types (fish, meat, fresh-cut vegetables) under various MAP conditions that correlate well with the spoilage state and the food test panel results.
- identify a method to group and quantify the results of the food test panel
- explore different miniaturized optical 'nose' sensor strategies that enabling the detection and monitoring of specific gas-markers inside the food package in a non-contact way.
- explore a non-contact sensor strategy that would allow users to monitor package integrity, e.g. detect CO_2 leakage from the MAP.

Ideally, the proposed sensor would produce a signal when a specific gas-marker exceeds a threshold concentration. This response would then mimic the food 'sniffing' test panel results. The threshold concentration for various food products poses quite a challenge on the optical 'nose' sensitivity: very low, sub-parts per million (ppm) concentrations need to be detected reliably among a soup of different gas-markers.
Next to this main technical challenge, there are secondary challenges that the sensor technology needs to address: (a) The sensor needs to probe the head-space environment inside the MAP without compromising the package integrity. (b) The implementation of the sensor in the MAP-production chain should be easy, fast and reliable. If the implementation of the sensor proves to be too difficult or too expensive, the widespread adoption of this technology will not occur. (c) The sensor unit, if it comes in physical contact with the food should not pose a hazard to the consumer, e.g. when swallowed or interferes with the product and (d) the recycling or disposal strategies of the sensor after its use should be thoroughly investigated. Next to the technical challenges, it is unclear whether the consumers or producers are willing to use the new technology and how much are they willing (or

should) pay for this functionality.
It has been identified that integrated optical spectroscopic sensors, in combination with gas-adsorbing coatings, are one of the promising candidates to achieve these specifications. A detailed analysis of the proposed sub-ppm sensor architecture is given in Chapter 5 and the package integrity monitoring in Chapter 6.

1.1.2 Fugitive methane leak detection

Methane (CH_4) is a strong greenhouse gas and is the main constituent of natural gas. Methane has a Global Warming Potential (GWP) 84 times higher than CO_2 over a 20 year span and 28 times when compared over 100 years, the full lifetime of atmospheric methane after which it decomposes. Currently, methane in the atmosphere accounts for more than 10% of all GHG-induced global warming [2]. In view of the relatively short lifespan of methane, any short-term reduction of methane emissions would have a pronounced effect on the climate change and is therefore has come under attention of the scientific community and policy makers. The Oil and Gas industry is responsible for about 30% of all anthropogenic methane emissions. This is because strong unwanted fugitive methane leakages occur during the production, transport, and distribution, with leakage rates of 2-10% of the total production. The unnoticed natural gas leaks are also the cause of great problems in the gas distribution sector, where they can lead to sudden fires or even explosions on site which compromises the security of people on site. Current methane monitoring solutions are limited in terms of sensitivity, cost-efficiency and are unable to precisely quantify and locate the rate of the leaks reliably. Additionally, existing methods are too expensive to monitor all of the many sites (more than 2 million sites worldwide) continuously 24/7. Widespread adoption of leak detection and repair is hindered by the current high-cost gas monitoring equipment. In view of this issue, the US department of Energy has issued an ARPA-E program "Methane Observation Networks with Innovative Technology to Obtain Reductions" (MONITOR) in 2014 which aims to address these shortcomings by supporting the development of novel technologies that can estimate methane emission flow rates, provide continuous monitoring, localize the leak source, and improve the accuracy of methane detection [6]. The vast majority of solutions backed by the program is based on miniaturized optical gas sensors, hereby confirming the need for a sensitive, yet affordable (optical) trace gas sensor. Furthermore, facilities which aim to capture and store (or reuse) CO_2 would benefit from a scalable, continuous gas monitoring solution as well.

1.2 Personal health monitoring devices

A completely different area which requires innovative portable gas sensors is situated in the medical domain. It is expected that point-of-care diagnostics will play an ever-growing role in the (bio)-medical sensor market. Due to an increasingly aging population, medical costs are expected to be reduced by focusing on early detection of disease markers and fast adequate monitored medication. To make this possible, novel sensors are required that are capable of early detection of specific disease markers without using expensive hospital time and infrastructure. Over time this should allow for the screening of many more diseases at the general practitioner (GP) level or even for self-screening at home, reducing the medical cost for the population. Among many different biomedical applications which require a miniaturized sensor, analysis of the gas composition of exhaled breath is believed to contain a plethora of information for patient diagnosis of some widespread ailments. Our breath contains over 400 VOCs of which some have been identified as potential biological indicators for specific diseases [7]. Concentrations of acetone, ammonia (NH_3) and nitric oxide (NO) are believed to correlate well with medical conditions such as asthma, kidney failure and other oral diseases [8–10]. Moreover, recurrent monitoring of exhaled NH_3 of dialysis patients would be beneficial for the evaluation of the treatment. In order for these gas monitoring devices to be widely used for point-of-care deployment irrespective of the economic and geographic boundaries, orders of magnitude improvements are needed in terms of sensitivity and cost, energy efficiency, and size (SWaP-C).

1.3 Review of gas sensing technologies

Gas sensing devices measure changes of different physical or chemical properties. In what follows, an overview is given of the state-of-the-art with an emphasis on widely used competing technologies which can be miniaturized and potentially employed in high-volume applications as described above. These can be classified into optical and non-optical techniques.

1.3.1 Non-optical gas sensors

Three classes of non-optical techniques can be defined: gas chromatography, the workhorse of analytical chemistry, electrical gas sensors and mass sensors. From these three, (micro-)Gas Chromatography (μGC) systems are the main contender to compete with integrated spectroscopic optical methods in terms of specificity, sensitivity, size and cost.

(micro-) Gas Chromatography

Gas chromatography is an accurate technique used in analytical chemistry to analyze complex mixtures with high reliability, accuracy and sensitivity. This can be performed on non-gaseous samples as well, given that they can be vaporized without decomposition. In such a device the gaseous analyte is diluted in a carrier gas and is forced through a long capillary with a coating on the inside for which the adsorption/desorption rate is molecule specific [11]. In this manner, a complex gas mixture can be physically separated in its components and the individual components can be identified based on their retention time in the capillary. A mass detection system at the end of the column determines the concentration of each component. For benchtop instruments, the detection is often based on measuring the thermal conductivity which provides a signal proportional to the gas analyte concentration passing by at a specific time. The thermal conductivity of the carrier gas is used as the reference baseline.
There is ongoing interest in fabricating and integrating the various parts on a single platform by utilizing known silicon wafer technology processes to realize miniature (micro-) gas chromatography systems [12–17]. In view of the limited length of on-chip microfluidic capillaries (order 1 meter), μGC systems often first use a pre-concentration layer to enhance the concentration of the analytes in a high flow rate environment [12, 16]. Monolithic integration of all subcomponents is possible: pre-concentration layer, GC columns and detectors have been shown in a single silicon die, fabricated using well-known Micro-ElectroMechanical System (MEMS) processes such as Deep Reactive Ion Etching (DRIE), see also Figure 1.4 [16]. The GC capillary is fabricated by etching a deep spiral (about 1 meter in length, 0.5 mm deep) on the chip. The pre-concentrator and detector are based on a MEMS resonator plate which is functionalized with a polymer to trap the molecules. By measuring resonance frequency shifts, the mass on the resonator is calculated. The plate is actuated using magnets and heaters are used to scrub or modulate the capillary response. Furthermore, MEMS based pump/injectors can be fabricated in similar manner. Other miniaturized mass detectors are also further explored such as Surface Acoustic Wave (SAW) sensors [12, 18], integrated electrochemical sensors [15], nano-electromechanical resonator systems (NEMS) [14, 19] and miniaturized thermal conductivity detectors [17]. Currently, there are no commercial full monolithic μGC systems yet, however APIX Analytics is well on its way and already offers sub-ppm portable GC systems with NEMS-based chip mass detectors [20]. One of the challenges of μGC is the limited available length of the on-chip capillary, limiting the separation capacity of such devices which ultimately hinders the specificity required for highly demanding applications. Moreover, the need for a carrier gas, active pump and heating

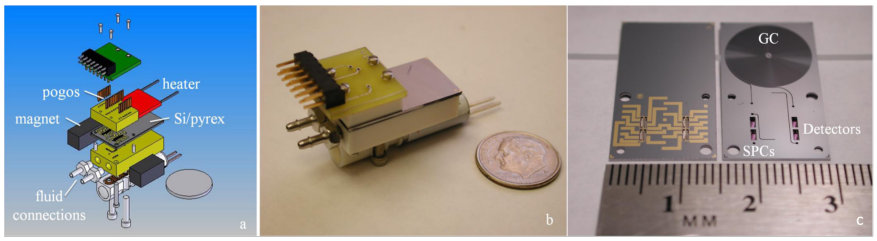

Figure 1.4: Schematic and photograph of packaged monolithically integrated μGC system on a silicon chip (a,b). The pre-concentrator, GC column and mass detector are fabricated using MEMS processes on a single silicon chip (c) [16].

increases the overall complexity and can limit the widespread applicability. The analysis speed is relatively slower than other methods. Furthermore, the choice of coating material for the μGC capillary and pre-concentrating does not give universal performance for all gas types and hinders specificity [12]. A careful match must be found for each application at hand separately. And lastly, the dynamic range of the sensor depends on the coatings properties, GC column length and detector performance and can be quite limited compared to optical sensors.

Electrical gas sensors

These sensors measure the variation of electrical properties such as conductivity in the presence of a gas. There are many different types of electrical sensors and can be classified based on the material with which the gas molecules interact: Metal Oxide Semiconductors (MOS), conducting polymers and carbon nanotubes cover most of the used materials [21]. MOS sensors have for many years been the dominant toxic sensing technology for Oil and Gas installations. While very small gas concentrations can be detected with a tiny low-cost sensor, the selectivity of such structures is very limited, since it is completely determined by how selective the material interacts with the molecule of interest. The primary challenges for MOS sensors are: (1) they are typically slow in response, the typical T90 [2] is on the order of tens of seconds. (2) There is no built-in self-test mechanism and therefore the sensors need to be periodically calibrated and 'bump'-tested to make sure that they are not giving false readings. A dead sensor gives a zero-response even when there is immediate danger. (3) The sensors are highly sensitive to temperature and humidity variations [21].

Other popular electrical sensors use electro-chemical cells. These cells rely on oxidizing or reducing (redox) the analyte gas at the electrode surface and measure the resulting current. Main problem with this type is the limited

[2] T90: time to reach 90 % of end value.

lifetime and frequent calibration. Lastly, there are electrical gas sensors based on photoionization detectors, popular with hand-held devices and as part of a μGC system due to their fast response and low cost. The key principle is to ionize the target gas with a high-energy photon. e.g. with ultraviolet (UV) light and measure the current produced by the ions. The current scales with the number of ions and therefore the target gas concentration. The response is broadband, not molecule-specific, making them ideal for μGC-systems which require concentration analysis of an isolated stream of target analytes.

Mass sensors

Mass sensors also measure the adsorption of gas molecules by a material typically by measuring the resonance frequency of a cantilever, which depends on the total mass (cantilever and gas molecules) of that structure. Again, while being very sensitive, the selectivity depends on the material that is used for gas adsorption. Typical examples are the integrated detectors used for μGC systems such as SAWs and NEMS cantilevers. In a SAW sensor, a piezo-electric substrate is used where electrodes are patterned in such a way to efficiently induce surface mechanical waves with an electrical signal. A gas-adsorbing coating material is added on top of the substrate that captures the molecules. A change in the amplitude, phase or frequency of the acoustic wave due to the presence of the gas is probed with the electrodes and processed to extract the mass. The selectivity here is again solely determined by the coating properties and is limited. SAW sensor arrays with five different selective polymers have been used to successfully discern gas mixtures [22]. However, it is hard to warrant the selectivity for applications where dust, water and other contaminants in the sampled volume can produce an unwanted signal cross-talk whenever similar molecules or particles are co-adsorbed on the same coating type. Additionally, inherent to non-optical sensors, electromagnetic interference can deteriorate the signal. On top of that, neighbouring SAW sensors need to be shielded from each other [12].

1.3.2 Optical gas sensors

Optical gas sensors based on optical absorption have the advantage of fast response, minimal environmental drift and high gas specificity. Furthermore the cross-talk between different gas species can be minimized by carefully choosing the measured wavelength range [23]. Only integrated optical gas sensor technologies are discussed that cover the most promising fields: refractive index sensors, Raman sensors, photothermal and photoacoustic sensors, integrated tunable laser diode spectroscopy systems, non-dispersive infrared sensors (NDIR) spectroscopic sensors and integrated

Fourier-Transform Infrared Spectrometers (FTIR).

refractive index sensors

The adsorption of gas molecules by a material gives rise to a change in the refractive index of the material, which can be measured by on-chip optical interferometric techniques, for example in a Mach-Zehnder Modulator (MZM) configuration. All previously mentioned gas adsorbing coatings can be used to add selectivity and enhance the effective surface area and hence increase the apparent refractive index change [7, 24, 25]. Label-free biosensing of various chemicals has been shown [26, 27], the key principle is to use a highly specific biochemical binding reaction to trap one specific biomolecule (protein) to the surface functionalization layer. While optical interferometry in combination with porous coatings is very sensitive, these devices suffer from the same issues as the non-optical technique, namely the critical dependence on a coating material for selective adsorption.

Optical spectroscopic gas sensors on the other hand, measure the absorption- or Raman spectrum of a gas sample directly. Every molecule has a characteristic 'fingerprint' spectrum, which allows identifying the components of a complex gas mixture along with their concentration [28, 29]. This is a 'universal' technique which can identify and quantify a sample in any state: solid, liquid or gaseous. This approach does not require the interaction with a material, distinguishing it from the aforementioned non-optical and refractive index techniques [3]. The spectroscopic sensors can be further categorized by how the light interacts with the gas medium and what property is measured.

Integrated Raman spectroscopy

First proof-of-principle experiments were recently performed showing initial results for both spontaneous- and stimulated Raman spectroscopy on a silicon nitride photonic chip, suitable for gas and liquid detection [30, 31]. Furthermore, it is possible to use metallic structures to enhance the weak Raman signal on the chip through Surface Enhanced Raman Spectroscopy (SERS) to create local 'hot spots' on the optical waveguide, hereby strongly enhancing the light-matter interaction strength. It has been shown that waveguides patterned with gold bowtie antennas, show a 10^6 enhancement in Raman signal compared to free space Raman scattering of the same molecule [32]. This is one approach for future on-chip Raman sensing systems. Alternatively, plasmonic slotted waveguides can be used [33]. The remaining challenges for a fully integrated system is to develop high performance spectrometers, light source, isolator and extremely high extinction

[3] As will be explained in the Chapter on Photothermal Spectroscopy, a preconcentrating coating can still be highly beneficial to compensate for lower on-chip interaction length. However, the selectivity of the method is attributed to the uniqueness of the optical absorption spectrum of the molecule

Raman pump filter on the same chip.

Photothermal and photoacoustic spectroscopy

In recent years, several indirect optical spectroscopic techniques are starting to emerge with extremely sensitive detection capabilities. Main principle is that instead of looking at what happens with the light that interacts with the gas of interest, the interaction is probed with another, decoupled system. Light that is absorbed at wavelengths of molecular vibrations (which does not subsequently emit) results in sample heating. This heat changes the optical and mechanical properties (typically through thermal expansion) of the system, which can be probed electrically or optically. Quartz-Enhanced Photoacoustic Absorption Spectroscopy (QEPAS) has become popular in recent years and ppb-level detection of trace gases has been demonstrated [34]. A quartz tuning fork is used to measure the acoustic waves generated by the expanding gas, which is heated by a tunable mid-infrared laser. Although a promising technique, the size, fabrication complexity and the expensive laser-sources limit the current application range but the field is rapidly expanding [35, 36]. Other promising techniques involve optically probing the change in physical properties due to the wavelength selective heating. They rely on the photothermal-lensing [37], -deflection [38], (heterodyne) -interferometry [39] or -radiometry [40] effects. Among these, several have demonstrated sub-ppb trace gas sensitivities and even sub-parts-per-trillion-sensitivities using a resonant cantilever readout [41]. Single-molecule imaging has also been demonstrated [42, 43]. Usually these high sensitivities are obtained with bulky, table-top measurement schemes. Key feature of all these indirect methods is that the measured quantity is directly proportional to the absorbed energy and is therefore immune to noise induced by reflections, scattering or other effects observed in conventional spectroscopy. Additionally, the photothermal signal can be greatly amplified as compared to conventional spectroscopy methods. A more detailed discussion is presented in Chapter 5.

Integrated Tunable Diode Laser Absorption Spectroscopy (TDLAS)

Silicon photonics technology has been used to demonstrate on-chip TDLAS of methane [44]. Using a near-IR light at 1650 nm distributed-feedback (DFB) laser and an uncooled InGaAs detector, the evanescent optical field of a high-index contrast nanoscale silicon waveguide is used to probe ambient methane, yielding sub 100 ppm detection limits. The results demonstrate the feasibility of chip-scale photonic integration for realizing compact, cost-effective, and versatile gas sensors, albeit it is challenging to reach sub-ppm sensitivities with this method.

1.4 Outline

In this PhD, the integration of novel, highly sensitive spectroscopic sensors on silicon photonic ICs is pursued that will pave the way for ultra-compact, cheap, highly sensitive and selective devices. The main objective is to address the following question: **can we realize chip-scale, spectroscopic gas sensors that obtain sensitivities below 1 part per million (ppm) based on technology that can be mass-manufactured at low cost?** The application range for such devices is very broad. One can envision for example the incorporation of such sensors in food packages for spoilage detection by 'sniffing' the food as explained in the section on intelligent packaging. Or one could think of incorporating such devices in a portable safety monitor or smartphone, which can measure e.g. CO_2, CO and CH_4 in air. In the case of food packages the sensor itself must be disposable, implying that the interrogating mid-IR light source and receiving photodetector should be off-chip. In the case of a portable application (e.g. personal health device or smartphone) integrated light sources and spectrometers will be required, yet overall cost will still be of paramount importance. The challenges of this PhD work are

- How can we reach sub-ppm sensitivity on a disposable, passive silicon chip, which is read out using an external robust optical interrogation system?
- How can we integrate in a low-cost way mid-infrared sources and spectrometers on a silicon trace gas sensor for use in handheld applications?
- Is it possible to calibrate the sensor on-line, such that a pre-calibration is not necessary? This would dramatically increase the viability of such a sensor in a commercial application and decrease the cost of fabrication.

In Chapter 2, the basic concepts of absorption spectroscopy are reviewed. The silicon photonics waveguide platform is introduced and the benefits and challenges for (mid-)infrared spectroscopy applications are discussed. Dr. Ruijun Wang has fabricated a variety of PICs capable of TDLAS combining III-V integrated laser sources and the SOI platform through heterogenous integration for spectroscopy in the Short-Wave Infrared (SWIR) wavelength range of 2-3 µm. The author has contributed to the gas sensing experiments and some key results are outlined. Furthermore, the main challenge is discussed on how to deal with the reduced on-chip optical interaction length of light with the analyte.

Spectroscopy of complex gas molecules or liquids is commonly performed using broadband sources which require a sensitive spectrometer to analyze the spectrum after having passed through the analyte. In a fully-integrated system, the silicon waveguide, potentially coated with a gas adsorbing layer, can act as an integrated 'gas cell'. While silicon spectrometers operating in the mid-infrared have been demonstrated, there is no low-cost solution for the integration of a high-performance mid-infrared photodetector array. To address this, a hybrid Arrayed Waveguide Grating (AWG) mid-infrared spectrometer was developed in Chapter 3, requiring only a single pixel detector instead of a detector array. The outputs of the AWG array are illuminating a high-performance single photodetector. The multiplexing of the different wavelength channels is done by time-modulating each output arm. Further, the use of a high-resolution AWG as a multiplexer for combining the output of laser source arrays is discussed. The optical design of all mid-infrared AWG photonic circuits except for the methane sensor (not fabricated) was carried out by Muhammad Muneeb, whereas further post-processing, integration, experiments, analysis and design of methane AWG sensor were performed by the author. The chip-on-a-package integration was carried out together with Fabio Pavanello and in close collaboration with VIGO, Poland in the context of the MIRPHAB project.

In Chapter 4, further quest for integrated broadband spectrometers led to the exploration of integrated Spatial Heterodyne Spectrometer (SHS) architectures. The SHS can be thought of as a Fourier-Transform Infrared Spectrometer (FTIR) without moving parts. In particular, a recent architecture called digital FTIR was designed for ultra-broadband and robust wavelength monitoring applications. Fabio Pavanello carried out the layout of the chip whereas simulations, further post-processing of the chip, integration, experiments and analysis was performed by the author.

For the disposable sensors, in order to reach sub-ppm sensitivity on a silicon chip, the benefits of CMOS compatible silicon photonics technology are combined with the highly sensitive photothermal spectroscopy methods in Chapter 5. Given the limited optical interaction length, additional porous gas adsorbers are integrated on the chip in order to concentrate the gas for maximum light-interaction. Brecht Vallaey and Bettina Baumgartner are acknowledged for fully developing and depositing the gas adsorbing coatings onto the photonic chips. The design, fabrication, experiment and analysis was performed by the author in the context of the CheckPack project. Aditya Malik has contributed greatly to the first version of the mid-infrared

setup and carried out the processing of the suspended membranes.

Chapter 6 is devoted to an integrated non-dispersive CO_2 measurement method for package integrity monitoring applications.

Overall conclusions and outlook are given in Chapter 7.

1.5 Publications

This work has led to several publications in international peer-reviewed journals. The majority of the work has also been presented at national and international conferences. An overview is given below.

1.5.1 Publications in international journals

1. R. Wang, B. Haq, S. Sprengel, A. Malik, **A. Vasiliev**, G. Boehm, I. Symonyte, A. Vizbaras, K. Vizbaras, J. Van Campenhout, R. Baets, M.C. Amann, G. Roelkens, "Widely tunable III-V/silicon lasers for spectroscopy in the short-wave infrared", IEEE Journal on Selected Topics in Quantum Electronics (invited), 25(6), p.1502412 (2019) `https://doi.org/10.1109/jstqe.2019.2924109`

2. F. Pavanello*[4], **A. Vasiliev***, M. Muneeb, G. Roelkens, "Broadband Digital Fourier Transform Spectrometer for On-Chip Wavelength Monitoring in the 2.3-µm Wavelength Range", IEEE Photonics Journal, 11(3), p.1-9 (2019) `https://doi.org/10.1109/JPHOT.2019.2914013`

3. **A. Vasiliev**, M. Muneeb, J. Allaert, J. Van Campenhout, R. Baets, G. Roelkens, "Integrated Silicon-on-Insulator Spectrometer with Single Pixel Readout for Mid-Infrared Spectroscopy", IEEE Journal on Selected Topics in Quantum Electronics, 24(6), p.8300207 (2018) `https://doi.org/10.1109/jstqe.2018.2820169`

4. R. Wang, S. Sprengel, **A. Vasiliev**, G. Boehm, J. Van Campenhout, G. Lepage, P. Verheyen, R. Baets, M.-C. Amann, G. Roelkens, "Widely tunable 2.3 µm III-V-on-silicon Vernier lasers for broadband spectroscopic sensing", Photonics Research, 6(9), p.858 (2018) `https://doi.org/10.1364/prj.6.000858`

5. R. Wang*, **A. Vasiliev***, M. Muneeb, A. Malik, S. Sprengel, G. Boehm, M.-C. Amann, I. A imonyte, A. Vizbaras, K. Vizbaras, R.

[4] * denotes equal contribution of authors.

Baets, G. Roelkens, "III-V-on-Silicon Photonic Integrated Circuits for Spectroscopic Sensing in the 2-4 µm Wavelength Range", Sensors (invited), 17(8), p.1788 (2017)
https://doi.org/10.3390/s17081788

6. R. Wang, Stephan Sprengel, A. Malik, **A. Vasiliev**, Gerhard Boehm, R. Baets, Markus-Christian Amann, G. Roelkens, "Heterogeneously integrated III-V-on-silicon 2.3x µm distributed feedback lasers based on a type-II active region", Applied Physics Letters , 109(22), p.221111 (2016)
https://doi.org/10.1063/1.4971350

7. **A. Vasiliev**, A. Malik, M. Muneeb, B. Kuyken, R. Baets, G. Roelkens, "On-Chip Mid-Infrared Photothermal Spectroscopy using Suspended Silicon-on-Insulator Microring Resonators", ACS Sensors, 1(11), p.1301-1307 (2016)
https://doi.org/10.1021/acssensors.6b00428

8. M. Muneeb, **A. Vasiliev**, A. Ruocco, A. Malik, H. Chen, M. Nedeljkovic, J. S. Penades, L. Cerutti, J.B. Rodriguez, G. Mashanovich, M. Smit, E. Tournie, G. Roelkens, "III-V-on-silicon integrated micro-spectrometer for the 3 µm wavelength range", Optics Express, 24(9), p.9465-9472 (2016).
https://doi.org/10.1364/oe.24.009465

1.5.2 Publications in international conferences

1. F. Pavanello, **A. Vasiliev**, R. Wang, M. Muneeb, A. Malik, G. Lepage, P. De Heyn, J. Van Campenhout, I. Simonyte, A. Vizbaras, K. Vizbaras, R. Baets and G. Roelkens, "Mid-IR devices and sub-systems based on SOI technology", PhotonIcs & Electromagnetics Research Symposium (PIERS) (invited), Rome, Italy, p.390, (2019)

2. **A. Vasiliev***, F. Pavanello*, M. Muneeb, G. Roelkens, "2.3 µm wavelength range digital Fourier transform on-chip wavelength monitor", Conference on Lasers and Electro-Optics (CLEO), United States, pp. STuO4.4 (2019).

3. **A. Vasiliev**, F. Pavanello, M. Muneeb, J. Jurenczyk, A. Janaszek, M. Liebert, G. Roelkens, "Novel approach for the integration of photonic circuits with Mid-IR detectors", Freiburg Infrared Colloquium, Germany, pp. paper 8.4 (2019).

4. J. Missinne, N. Teigell Beneitez, N. Mangal, J. Zhang, **A. Vasiliev**, J. Van Campenhout, B. Snyder, G. Roelkens, G. Van Steenberge, "Alignment-tolerant interfacing of a photonics integrated circuit using back-side etched silicon micro lenses", SPIE Photonics West, United States, pp. paper 10923 (2019).

5. G. Roelkens, R. Wang, **A. Vasiliev**, S. Radosavljevic, X. Jia, N. Teigell Beneitez, B. Haq, F. Pavanello, M. Muneeb, G. Lepage, P. Verheyen, J. Van Campenhout, S. Sprengel, G. Boehm, M.C. Amann, I. Simonyte, K. Vizbaras, A.Vizbaras, R. Baets, "III-V/Si photonic integrated circuits for the mid-infrared", IEEE International Conference on Group IV Photonics, Mexico, pp. FE1 (2018).

6. R. Wang, S. Radosavljevic, **A. Vasiliev**, M. Muneeb, A. Malik, R. Baets, S. Sprengel, G. Boehm, M.-C. Amann, I. Simonyte, A. Vizbaras, K.Vizbaras, G. Roelkens, "III-V-on-silicon mid-IR photonic integrated circuits", 2nd Global Summit and Expo on Laser Optics and Photonics, Italy, (2018).

7. G. Roelkens, R. Wang, **A. Vasiliev**, S. Radosavljevic, F. Pavanello, A. Malik, M. Muneeb, R. Baets, S. Sprengel, G. Boehm, M.C. Amann, I. Simonyte, A. Vizbaras, K. Vizbaras, "III-V-on-silicon photonic integrated circuits for spectroscopic sensing in the mid-infrared", Advanced Photonics Congress, Switzerland, pp. IM4B.1 (2018).

8. **A. Vasiliev**, M. Muneeb, J. Allaert, R. Baets, G. Roelkens, "Integrated Silicon-on-Insulator AWG Spectrometer with Single Pixel Readout for 2.3 um Spectroscopy Applications", European Conference on Integrated Optics (ECIO, Spain, pp. We.2.B.4-HRP (2018).

9. R. Wang, M. Muneeb, **A. Vasiliev**, A. Malik, Stephan Sprengel, Gerhard Boehm, I. Simonyte, Augustinas Vizbaras, Kristijonas Vizbaras, R. Baets, Markus-Christian Amann, G. Roelkens, "III-V/silicon photonic integrated circuits for spectroscopic sensing in the 2 um wavelength range", SPIE Photonics West, United States, pp. 1053603 (2018).

10. **A. Vasiliev**, M. Muneeb, R. Baets, G. Roelkens, "High Resolution Silicon-on-Insulator Mid-Infrared Spectrometers operating at 3.3 um", IEEE Photonics Society Summer Topicals 2017, Puerto Rico, pp. 177-178 (2017).

11. **A. Vasiliev**, A. Malik, M. Muneeb, R. Baets, G. Roelkens, "Photothermal Mid-Infrared Spectroscopy using Fano Resonances in Sili-

con Microring Resonators", CLEO 2016, United States, pp. SF2H.5 (2016).

12. **A. Vasiliev**, M. Muneeb, A. Ruocco, A. Malik, H. Chen, M. Nedeljkovic, J. Soler-Penades, L. Cerutti, J. B. Rodriguez, G. Z. Mashanovich, M. K. Smit, E. Tournie, G. Roelkens, "3.8 µm Heterogeneously Integrated III-V on Silicon Micro-Spectrometer", 18th European Conference in Integrated Optics 2016 (ECIO), Poland, pp. paper ECIO/p-24 (2016).

13. **A. Vasiliev**, A. Malik, M. Muneeb, R. Baets, G. Roelkens, "Design of Cavity-Enhanced Photothermal Mid-Infrared Spectroscopy for Sensing Applications", Proceedings of the 20th Annual Symposium of the IEEE Photonics Benelux Chapter, Belgium, pp. 199-202 (2016).

References

[1] Bill Gates. *Climate change and the 75% problem.* `https://www.gatesnotes.com/Energy/My-plan-for-fighting-climate-change`. Accessed: 2019-12-11.

[2] Thomas Stocker. *Climate change 2013: the physical science basis: Working Group I contribution to the Fifth assessment report of the Intergovernmental Panel on Climate Change.* Cambridge University Press, 2014.

[3] FAO Statistical Pocketbook. *World food and agriculture.* FAO: Rome, Italy, 2015.

[4] Breaktrough Energy Coalition. *Eliminating Spoilage/Loss in the Food-Delivery Chain.* `http://www.b-t.energy/landscape/agriculture/eliminating-spoilageloss-in-the-food-delivery-chain/`. Accessed: 2019-12-11.

[5] Brecht Vallaey. *Investigating gas adsorption in thin films by in situ spectroscopic ellipsometry.* PhD thesis, KU Leuven, 2018.

[6] US Department of Energy. *Methane Observation Networks with Innovative Technology to Obtain Reductions.* `https://arpa-e.energy.gov/?q=arpa-e-programs/monitor`. Accessed: 2019-12-11.

[7] Nebiyu Yebo. *Silicon Based Integrated Optical Gas Sensing.* PhD thesis, Ghent University, 2012.

[8] CMHHT Robroeks, KDG Van De Kant, Q Jöbsis, HJE Hendriks, R Van Gent, EFM Wouters, JGMC Damoiseaux, A Bast, WKWH Wodzig, and E Dompeling. *Exhaled nitric oxide and biomarkers in exhaled breath condensate indicate the presence, severity and control of childhood asthma.* Clinical & Experimental Allergy, 37(9):1303–1311, 2007.

[9] LR Narasimhan, William Goodman, and C Kumar N Patel. *Correlation of breath ammonia with blood urea nitrogen and creatinine during hemodialysis.* Proceedings of the National Academy of Sciences, 98(8):4617–4621, 2001.

[10] L Wang, K Kalyanasundaram, M Stanacevic, and P Gouma. *Nanosensor device for breath acetone detection.* Sensor Letters, 8(5):709–712, 2010.

[11] Harold M McNair, James M Miller, and Nicholas H Snow. *Basic gas chromatography*. John Wiley & Sons, 2019.

[12] Imadeddine Azzouz and Khaldoun Bachari. *MEMS Devices for Miniaturized Gas Chromatography*. MEMS Sensors: Design and Application, page 149, 2018.

[13] Stefano Zampolli, Ivan Elmi, Gian Carlo Cardinali, Luca Masini, Filippo Bonafè, and Federico Zardi. *Compact-GC platform: a flexible system integration strategy for a completely microsystems-based gas-chromatograph*. Sensors and Actuators B: Chemical, page 127444, 2019.

[14] Mo Li, EB Myers, HX Tang, SJ Aldridge, HC McCaig, JJ Whiting, RJ Simonson, Nathan S Lewis, and ML Roukes. *Nanoelectromechanical resonator arrays for ultrafast, gas-phase chromatographic chemical analysis*. Nano letters, 10(10):3899–3903, 2010.

[15] Te-Hsuen Tzeng, Chun-Yen Kuo, San-Yuan Wang, Po-Kai Huang, Yen-Ming Huang, Wei-Che Hsieh, Yu-Jie Huang, Po-Hung Kuo, Shih-An Yu, Si-Chen Lee, et al. *A portable micro gas chromatography system for lung cancer associated volatile organic compound detection*. IEEE Journal of Solid-State Circuits, 51(1):259–272, 2015.

[16] Ronald Manginell, Joseph Bauer, Matthew Moorman, Lawrence Sanchez, John Anderson, Joshua Whiting, Daniel Porter, Davor Copic, and Komandoor Achyuthan. *A monolithically-integrated μGC chemical sensor system*. Sensors, 11(7):6517–6532, 2011.

[17] Apoorva Garg, Muhammad Akbar, Eric Vejerano, Shree Narayanan, Leyla Nazhandali, Linsey C Marr, and Masoud Agah. *Zebra GC: A mini gas chromatography system for trace-level determination of hazardous air pollutants*. Sensors and Actuators B: Chemical, 212:145–154, 2015.

[18] Takamitsu Iwaya, Shingo Akao, Toshihiro Sakamoto, Toshihiro Tsuji, Noritaka Nakaso, and Kazushi Yamanaka. *Development of high precision metal micro-electro-mechanical-systems column for portable surface acoustic wave gas chromatograph*. Japanese Journal of Applied Physics, 51(7S):07GC24, 2012.

[19] Eric Sage, Ariel Brenac, Thomas Alava, Robert Morel, Cécilia Dupré, Mehmet Selim Hanay, Michael L Roukes, Laurent Duraffourg, Christophe Masselon, and Sébastien Hentz. *Neutral particle mass spectrometry with nanomechanical systems*. Nature communications, 6:6482, 2015.

[20] APIX Analytics. *Miniaturized and Modular Gas Analyzers for Industrial Analysis and OEM use*. `https://www.apixanalytics.com/`. Accessed: 2019-12-11.

[21] Xiao Liu, Sitian Cheng, Hong Liu, Sha Hu, Daqiang Zhang, and Huansheng Ning. *A survey on gas sensing technology*. Sensors, 12(7):9635–9665, 2012.

[22] Massimiliano Benetti, Domenico Cannatà, Enrico Verona, Alexandra Palla Papavlu, Valentina Carmen Dinca, Thomas Lippert, Maria Dinescu, and Fabio Di Pietrantonio. *Highly selective surface acoustic wave e-nose implemented by laser direct writing*. Sensors and Actuators B: Chemical, 283:154–162, 2019.

[23] Jane Hodgkinson and Ralph P Tatam. *Optical gas sensing: a review*. Measurement Science and Technology, 24(1):012004, 2012.

[24] Nebiyu A. Yebo, Petra Lommens, Zeger Hens, and Roel Baets. *An integrated optic ethanol vapor sensor based on a silicon-on-insulator microring resonator coated with a porous ZnO film*. Opt. Express, 18(11):11859–11866, May 2010.

[25] Nebiyu A. Yebo, Sreeprasanth Pulinthanathu Sree, Elisabeth Levrau, Christophe Detavernier, Zeger Hens, Johan A. Martens, and Roel Baets. *Selective and reversible ammonia gas detection with nanoporous film functionalized silicon photonic micro-ring resonator*. Opt. Express, 20(11):11855–11862, May 2012.

[26] Katrien De Vos, Irene Bartolozzi, Etienne Schacht, Peter Bienstman, and Roel Baets. *Silicon-on-Insulator microring resonator for sensitive and label-free biosensing*. Opt. Express, 15(12):7610–7615, Jun 2007.

[27] Arthur Nitkowski, Long Chen, and Michal Lipson. *Cavity-enhanced on-chip absorption spectroscopy using microring resonators*. Opt. Express, 16(16):11930–11936, Aug 2008.

[28] Barbara Stuart. *Infrared spectroscopy*. Kirk-Othmer Encyclopedia of Chemical Technology, pages 1–18, 2000.

[29] Peter Larkin. *Infrared and Raman Spectroscopy; Principles and Spectral Interpretation*. Elsevier, 2011.

[30] Haolan Zhao, Stéphane Clemmen, Ali Raza, and Roel Baets. *Stimulated Raman spectroscopy of analytes evanescently probed by a silicon nitride photonic integrated waveguide*. Optics letters, 43(6):1403–1406, 2018.

[31] Haolan Zhao, Ali Raza, Bettina Baumgartner, Stéphane Clemmen, Bernhard Lendl, Andre Skirtach, and Roel Baets. *Waveguide-Enhanced Raman Spectroscopy Using a Mesoporous Silica Sorbent Layer for Volatile Organic Compound (VOC) Sensing.* In CLEO: Science and Innovations, pages STh1F–7. Optical Society of America, 2019.

[32] Frédéric Peyskens, Ashim Dhakal, Pol Van Dorpe, Nicolas Le Thomas, and Roel Baets. *Surface enhanced Raman spectroscopy using a single mode nanophotonic-plasmonic platform.* ACS photonics, 3(1):102–108, 2015.

[33] Yang Li, Haolan Zhao, Ali Raza, Stéphane Clemmen, and Roel Baets. *Surface-Enhanced Raman Spectroscopy Based on Plasmonic Slot Waveguides With Free-Space Oblique Illumination.* IEEE Journal of Quantum Electronics, 56(1):1–8, 2019.

[34] Vincenzo Spagnolo, Pietro Patimisco, Simone Borri, Gaetano Scamarcio, Bruce E Bernacki, and Jason Kriesel. *Part-per-trillion level SF 6 detection using a quartz enhanced photoacoustic spectroscopy-based sensor with single-mode fiber-coupled quantum cascade laser excitation.* Opt. Lett., 37(21):4461–4463, 2012.

[35] Pietro Patimisco, Angelo Sampaolo, Huadan Zheng, Lei Dong, Frank K Tittel, and Vincenzo Spagnolo. *Quartz–enhanced photoacoustic spectrophones exploiting custom tuning forks: a review.* Advances in Physics: X, 2(1):169–187, 2017.

[36] Hongpeng Wu, Lei Dong, Xukun Yin, Angelo Sampaolo, Pietro Patimisco, Weiguang Ma, Lei Zhang, Wangbao Yin, Liantuan Xiao, Vincenzo Spagnolo, et al. *Atmospheric CH4 measurement near a landfill using an ICL-based QEPAS sensor with VT relaxation self-calibration.* Sensors and Actuators B: Chemical, 297:126753, 2019.

[37] Humberto Cabrera, Jehan Akbar, Dorota Korte, Imrana Ashraf, Evelio E Ramírez-Miquet, Ernesto Marín, and Joseph Niemela. *Absorption spectra of ethanol and water using a photothermal lens spectrophotometer.* Applied spectroscopy, 72(7):1069–1073, 2018.

[38] David Becker-Koch, Boris Rivkin, Fabian Paulus, Hengyang Xiang, Yifan Dong, Zhuoying Chen, Artem A Bakulin, and Yana Vaynzof. *Probing charge transfer states at organic and hybrid internal interfaces by photothermal deflection spectroscopy.* Journal of Physics: Condensed Matter, 31(12):124001, 2019.

[39] Yuechuan Lin, Wei Jin, Fan Yang, Jun Ma, Chao Wang, Hoi Lut Ho, and Yang Liu. *Pulsed photothermal interferometry for spectroscopic gas detection with hollow-core optical fibre.* Scientific reports, 6:39410, 2016.

[40] Nina Verdel, Griffin Lentsch, Mihaela Balu, Bruce J Tromberg, and Boris Majaron. *Noninvasive assessment of skin structure by combined photothermal radiometry and optical spectroscopy: coregistration with multiphoton microscopy.* Applied optics, 57(18):D117–D122, 2018.

[41] Teemu Tomberg, Markku Vainio, Tuomas Hieta, and Lauri Halonen. *Sub-part-per-trillion level detection of hydrogen fluoride by cantilever-enhanced photo-acoustic spectroscopy.* arXiv preprint arXiv:1707.01312, 2017.

[42] A Gaiduk, M Yorulmaz, PV Ruijgrok, and M Orrit. *Room-temperature detection of a single molecule's absorption by photothermal contrast.* Science, 330(6002):353–356, 2010.

[43] Miao-Hsuan Chien, Mario Brameshuber, Benedikt K Rossboth, Gerhard J Schütz, and Silvan Schmid. *Single-molecule optical absorption imaging by nanomechanical photothermal sensing.* Proceedings of the National Academy of Sciences, 115(44):11150–11155, 2018.

[44] Lionel Tombez, EJ Zhang, JS Orcutt, Swetha Kamlapurkar, and WMJ Green. *Methane absorption spectroscopy on a silicon photonic chip.* Optica, 4(11):1322–1325, 2017.

2

Silicon photonics for optical absorption spectroscopy

SILICON *photonics was first developed with the promise to boost datacom speed and volumes. Now it is clear that other fields can benefit from these developments as well. In this chapter an overview is given of the Silicon-on-Insulator technology, specifically for (mid-infrared) sensing applications. Some basic sensing concepts are reviewed along the way, together with a discussion on the implications of limited optical interaction path length.*

Contents

2.1 Optical Spectroscopy

Many chemical species exhibit strong absorption in the UV/visible (UV/VIS: 200-700 nm), near infrared (NIR: 700 nm-2.5 µm) or mid infrared regions

(MIR: 2.5-14 µm) of the electromagnetic spectrum. The exact boundaries for the designation of the regions is loosely defined in literature. The absorption lines or bands are specific to each species and this forms the basis for their detection and measurement. Absorption spectra in the different spectral regions have different origins: UV/VIS energies probe the electronic transitions of the molecules, MIR energies correspond to molecular rotational and vibrational states and NIR are the first harmonic overtones of the same rovibrational states. In the so-called fingerprint region of the infrared (MIR), gas phase absorption spectra exhibit narrow lines as a result of molecular vibrations at discrete energy levels. These can be measured at high resolution, resolving the individual lines, or at lower resolution, measuring the absorption band envelope. Near IR spectra are typically overtones of fundamental vibrations in the mid IR and hence can be significantly weaker (e.g. up to three orders of magnitude). However, the availability of low-cost high quality sources and detectors in the NIR, enabled by research for telecommunication applications, still makes NIR systems attractive [1]. Additionally, due to spectral broadening at higher pressure and temperatures, the overtone bands in the NIR can overlap significantly such that the apparent net absorption coefficient can be of comparable value to individual, spectrally separated MIR absorption lines. An example is the detection of gaseous NH_3 at 1512 nm compared to the stronger MIR band at 3 µm, the apparent absorption coefficient at Standard Temperature and Pressure (STP) conditions[1] in the MIR is 'only' five times stronger than the overlapping NIR transition. In this case, the added complexity for the instrumentation at MIR wavelengths does not outweigh the stronger absorption cross-section.

Instrumentation in the mid-infrared region is often sub-categorized into three smaller windows, which is dominated by a different photodetector material technology[2]. Short-Wave InfraRed (SWIR) covers 1-2.5 µm. This is the wavelength range which can be covered by (extended) InGaAs photodetectors. Mid-Wave Infrared (MWIR), 3-5 µm is covered by (cryogenically) cooled InSb or InAsSb photodiodes. The Long-Wave Infrared (LWIR) 8-12 µm requires cooled HgCdTe- or Mercury-Cadmium-Telluride (MCT) detectors. Cryogenically cooled bolometers are also a popular choice [2]. Historically, the MIR range was used for thermal imaging and defense applications such as heat-seeking missiles, requiring free space transmission through the atmosphere. For this reason, the MIR windows that feature water absorption (e.g. 5-8 µm) are left out of this classification.

[1] temperature = 273.15 K and absolute pressure = 101.325 kPa

[2] exceptions in each range are possible, the given classification only relates to the most often used photodiode material

Conventional absorption spectroscopy is based on the application of the exponential Beer-Lambert law

$$I(\lambda) = I_0 e^{-\alpha(\lambda)L} \tag{2.1}$$

where I is the light intensity transmitted through the gas path, I_0 is the incident light intensity, α is the gas absorption coefficient at wavelength λ and L is the optical path length [1]. The absorption coefficient α is the product of the gas concentration (for example as the partial pressure in atmospheres) and the specific absorptivity of the gas ϵ (for example in cm^{-1} atm^{-1}). The optical transmittance $\mathcal{T}$ is defined as the ratio I/I_0. It is often required to compare the absorption strength between different molecules in different phase states (e.g. liquid versus gas). For this reason, the absorption cross-section σ_a in units (cm^2/molecule) is a better quantity that relates the absorption strength to a single molecule at any given temperature, pressure and state.

$$\sigma_a = \alpha/\rho \tag{2.2}$$

with ρ the molecular density in (molecules/cm^3) along a given path of length L. Furthermore, in the case of gases it is possible to convert the concentration to typical units of ppm by volume, the ideal gas equation $PV = Nk_BT$ can be used, where V is the volume of a closed cell, k_B is the Boltzmann constant and N is the number of molecules in the cell.
For low αL, the absorbance $A = 1 - \mathcal{T}$ is readily approximated as follows

$$A = \frac{I_0 - I}{I_0} \approx \alpha L \tag{2.3}$$

The quantity A is unitless but is often stated in 'absorbance units' (AU). Limits of detection can be quantified as the noise equivalent absorbance (NEA), in AU or the minimum detectable absorption coefficient α_{min}, in cm^{-1}. This allows different sensing methods to be compared, independent of the specified gas. Typical absorption spectra[3] of some common gas molecules in the mid-infrared are shown in Figure 2.1, for a series of gases in the mid-infrared.
Absorption features have a finite spectral width, typically expressed as Full Width at Half Maximum (FWHM) or as Half Width at Half Maximum (HWHM) and are typically on the order of tens of picometer for most environmental gas sensing applications. At low pressures, the rovibrational transition is dominated by Doppler-broadening effects, the gas velocities have a finite temperature dependant distribution, and the line has a Gaussian profile. At atmospheric pressure, the line is predominantly pressure-broadened

[3] 0.01 cm^{-1} spectral resolution used in the HITRAN calculation

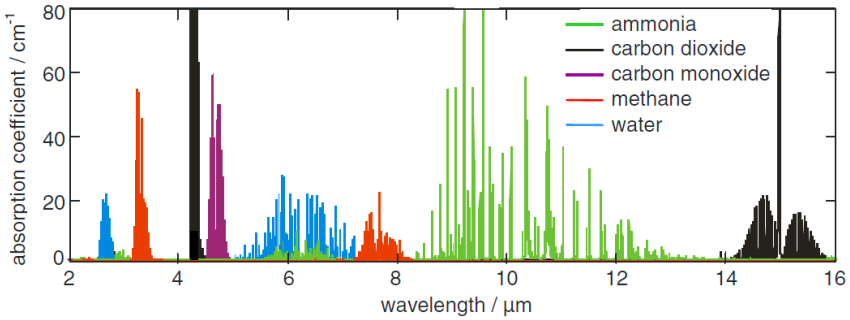

Figure 2.1: IR absorption spectra for common gases in the mid-infrared wavelength range. The absorption values are for pure gases (100%vol) at STP (273 K, 1 atm) [1].

or collision-broadened and the line has a Lorentzian profile [3]. For arbitrary cases, the spectral lines are best modeled with a Voigt-profile, a convolution of Gaussian and Lorentzian line combining both effects. The collision broadening further takes into account collisions between molecules of the same kind (self-broadening) and collision with the matrix (air-broadening). The latter is typically important for low concentration measurements. These broadening mechanisms are important to consider. For example methane has multiple transitions near 3.3 µm which all start to overlap and contribute to one very strong and broad absorption line at STP conditions due to pressure broadening. A dispersive mid-infrared methane measurement system with a coarse spectral resolution designed to identify this broad transition at STP conditions, might not function at all when sensing low pressure and low temperature gas volumes containing methane[4], see also Figure 2.2.

More in-depth analysis and discussion on the physics behind molecular absorption spectroscopy and benchtop instrumentation can be found here [3, 5, 6].

2.2 Silicon-on-Insulator technology

Silicon photonics is emerging as an important platform for photonic integration [7]. A photonic integrated circuit (PIC) comprises multiple optical functionalities necessary for optical spectroscopy on a single chip such as wavelength (de)multiplexing, filtering, light generation, modulation and detection. The PIC is typically comprised of a stack of high-index material, e.g. silicon or InP, sandwiched between lower-index ones such as glass to

[4] 0.01 cm^{-1} spectral resolution used in the HITRAN calculation

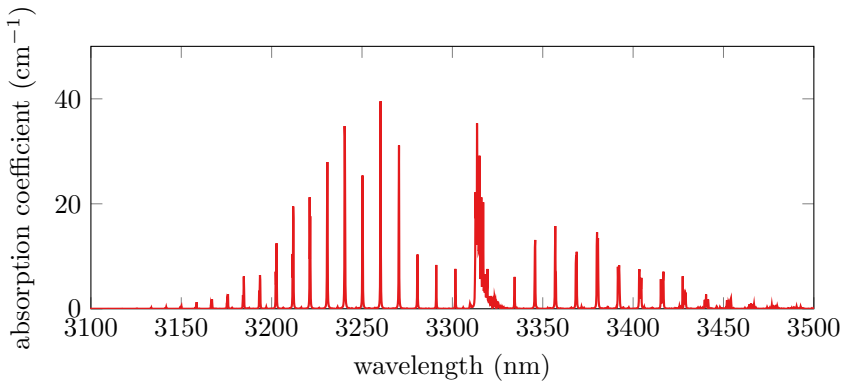

Figure 2.2: Simulation of methane absorption in the 3.3 µm wavelength range at STP conditions and 100% vol concentration, based on HITRAN [4]. The absorption peak at 3.3 µm is an overlap of many neighbouring transitions, resulting in a spectrally broad peak which can potentially be resolved using an integrated high-resolution dispersive spectrometer.

confine the light. The layers can be deposited or grown chemically on top of a semiconductor wafer and the typical thicknesses are on the order of microns or less. Structures are patterned in the top device layer that support single-mode optical guiding modes. Many different material platforms have been explored over the years, each having their own (dis)-advantages. The Silicon-on-Insulator (SOI) platform has emerged as one of the most popular platforms and consists of a silicon substrate (300 mm wafer diameter), athermally grown silicon oxide (SiO_2) layer (thickness 1 to 3 µm) and a silicon device layer (typical thickness 220 nm or 400 nm). The high index contrast between silicon and SiO_2 ($\Delta n \approx 2$) enables very high optical confinement, resulting in tight bend radii of merely a few microns. High performance passive and active devices have been realized with an ultra small footprint. Essential components have been shown and include: tightly confined low loss waveguides [9, 10], grating couplers to couple light in and out of the chip [11], high-Q microring resonators [12] and AWGs wavelength (de)multiplexers [13] have been successfully demonstrated on SOI in the 1550 nm wavelength range. An example of a silicon photonic integrated circuit wire-bonded on a printed circuit board is shown in Figure 2.3.

Spectroscopy in the mid-infrared is attractive due to the much larger absorption cross-section with increasing wavelength of operation as compared to the telecommunication wavelength band at 1550 nm, exceptions notwithstanding. This is due to the fact that most fundamental (ro)-vibrational

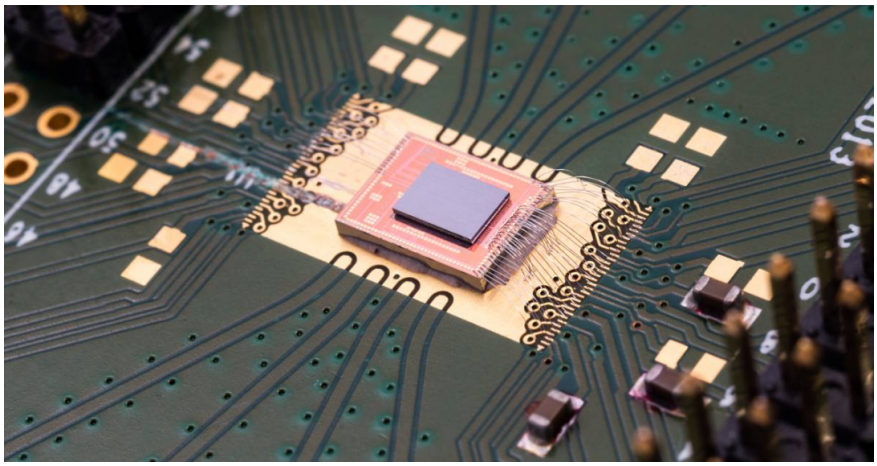

Figure 2.3: Optical microscope image of a SOI photonic integrated circuit, wire-bonded to a printed circuit board. Image taken from [8].

energy transitions are addressed in the mid-infrared wavelength region, whereas only overtones are addressed in the near-infrared. The SOI platform can still be used with minor adaptations up to 4 µm wavelength, after which the buried oxide absorption and substrate leakage increase exponentially, rendering waveguide propagation impractical [14]. This wavelength range is still relevant for many practical applications and mid-infrared components and devices have been demonstrated on the SOI platform such as filters, modulators, sources and detectors [15–20]. It is in this context that this work advances the field through novel device integration strategies and sensing schemes. Integration of silicon photonics for spectroscopy is being considered on other substrate platforms such as CaF_2 [21] as well as the use of chalcogenide glass waveguides [22–24].

2.3 On-chip mid-infrared spectroscopy

In most applications, a spectroscopic sensing system should have a light source, a probe component and a spectrometer or single pixel detector. For a compact sensor system, both the light source and detector should be integrated together with the waveguide circuit, which interacts with the environment through evanescent coupling of the light. Figure 2.4 shows two typical configurations of fully integrated mid-infrared on-chip spectroscopic sensors [25]. In both configurations, light is coupled from the integrated light source to the waveguide and then split into two arms. The probe com-

ponent in one arm interacts with the analyte while the other one provides the reference information. Different probe components have been proposed to realize efficient interaction between the environment and light in the waveguide, e.g., slot waveguides [26], spiral waveguides [27], and microring resonators (MRRs) [28]. In the case of liquid sensing, a low-cost broadband light source such as a light emitting diode (LED) can be used since liquid samples typically have broad absorption features. In this configuration, a spectrometer with integrated photodetectors should be implemented to analyze the absorption spectra. For gas sensing, typically a tunable single mode laser is required to probe the absorption lines of gases, as used in the popular tunable diode laser absorption spectroscopy (TDLAS) technique. Integrating a widely tunable laser or a broadband wavelength coverage laser array on the waveguide circuit enables to simultaneously detect several gases or even broad absorption features of liquids using the configuration shown in Figure 2.4(b). At 2 µm wavelength, a propagation loss of 0.6 dB/cm was

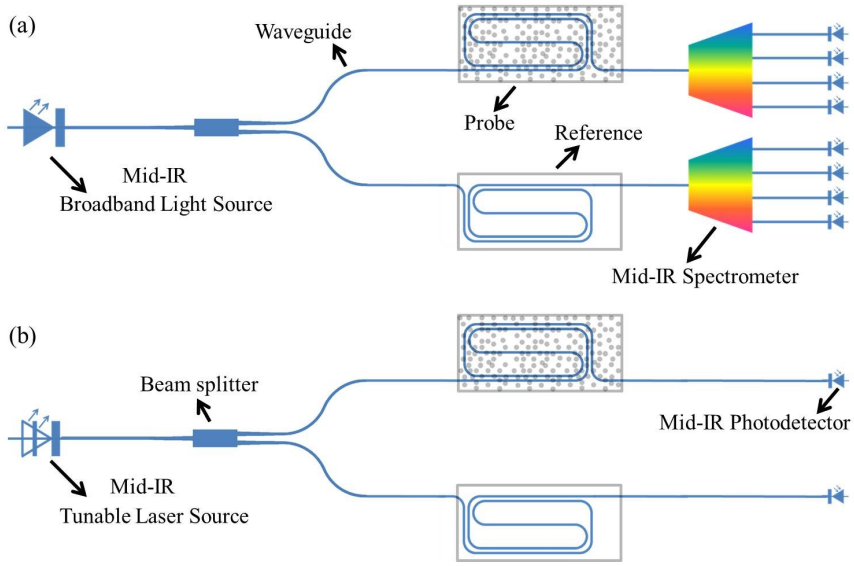

Figure 2.4: Schematic of two silicon photonic configurations to realize a fully integrated on-chip mid-infrared absorption spectroscopy sensor. Broadband source and spectrometer, best suited for liquid and solid analytes (a). Tunable single mode laser source for trace gas detection (b) [25].

achieved for SOI strip waveguides (TE-polarization) [29]. As the wavelength increases to 3.8 µm, a low propagation loss of 1.5 dB/cm for 400 nm rib SOI waveguides with 220 nm etch depth was reported [30].

2.4 Breaking the sub-ppm limit

Down-sizing traditional sensing methods such as NDIR, FTIR or TDLAS to integrated on-chip solutions presents a challenge as sensors based on evanescent field interaction are limited to an optical interaction length much shorter than for bulk instruments where for instance a multi-pass free space Herriott cell can be used. The evanescent tail of the confined waveguide mode interacts only partially with the analyte. The optical mode overlap of the waveguide with the analyte, often called the confinement factor Γ, is less than unity and typically scales inversely proportional with propagation loss due to increased scattering losses at the interfaces [31]. Additionally, spurious on-chip reflections create unwanted interference effects which will deteriorate the Signal-to-Noise Ratio (SNR) associated with the absorption feature [32]. The small physical size of the PIC together with the on-chip propagation losses, reflections and Γ limit the ultimate attainable optical interaction length. It is interesting to consider what limit of detection current state-of-the-art integrated waveguide platforms could potentially achieve using such a system. It will be shown that sub-ppm detection is not possible with this approach and therefore other innovative methods such as photothermal- and photoacoustic spectroscopy methods are required to boost the matter-light interaction. Additionally, the use of pre-concentrating gas adsorbing coatings is discussed to boost the signal for practical miniaturized on-chip spectroscopic gas sensors.
As described in the previous section, there are two conventional absorption spectroscopy strategies to retrieve information about an analyte. In a laser-scanning system, a tunable narrow linewidth laser is coupled into a waveguide evanescent based PIC. The attenuated signal is then recorded by a single-element photodetector as the laser is swept over the target wavelength range, see also Figure 2.4. The other strategy is to use a broadband source and resolve the spectral components with a spectrometer. The performance of both approaches suffers greatly from down-scaling directly to PIC designs. This is independent of spectral range and is determined by the optimal optical interaction path length on-chip which is governed by the lowest propagation loss and spurious reflections that will ultimately make the signal indistinguishable from noise.

Using a simple example it is demonstrated that current state-of-the-art waveguide platforms such as low-loss Si_3N_4 [33] with a record low loss of 0.045dB/m are not sufficient for sub-ppm detection using conventional TDLAS schemes for the near-infrared (NIR) wavelength range. The case holds true even in the mid-IR wavelength range (MIR) above 3µm where the ab-

sorption cross-section is a few orders of magnitude higher. Record low-losses of 0.1dB/cm were reported on an SOI platform in the $3.5\mu m$ wavelength range [9].

One can derive the sensitivity $\mathcal{S}$ of a TDLAS system using the exponential Lambert-Beer relation for optical transmission $\mathcal{T}$ through an optical waveguide medium exposed to an absorbing medium

$$\mathcal{T} = e^{-(\alpha_g \Gamma C + \alpha_L)L} \tag{2.4}$$

$$\mathcal{S}_{\mathcal{TDLAS}} = \left|\frac{\partial \mathcal{T}}{\partial C}\right| = \alpha_g \Gamma L e^{-(\alpha_g \Gamma C + \alpha_L)L} \tag{2.5}$$

with α_g the absorption coefficient of the pure analyte (cm^{-1}), Γ the confinement factor of the optical mode in the analyte, C the analyte concentration and α_L the effective waveguide propagation loss including scattering losses and material loss of the platform. Assume now that one has an on-chip

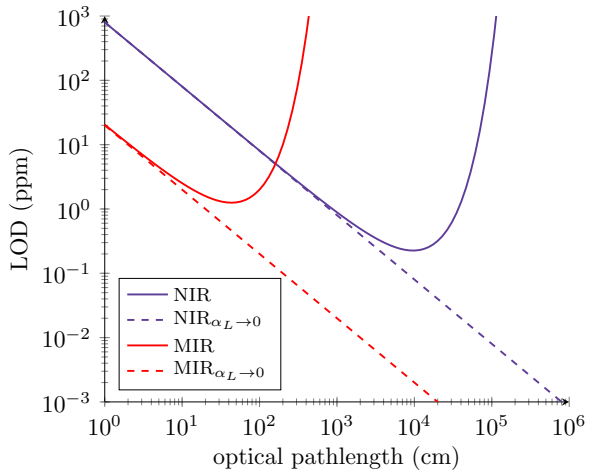

Figure 2.5: Projected limit of detection for toluene gas as a function of optical pathlength for an on-chip TDLAS spectroscopic sensor in the NIR (1.7 µm and MIR (3.3 µm wavelength ranges. The calculations assume a hypothetical best-case scenario using the lowest reported waveguide loss for the NIR range (0.045dB/m Si_3N_4 [34]) and MIR (0.1dB/cm SOI [9]), a minimum detectable transmission change of $\Delta\mathcal{T}_{min}$=10^{-4} and a confinement factor of unity. Projected results for lossless waveguides are denoted with a dashed line. It is clear that sub-ppm trace gas detection is not possible by simply down-scaling TDLAS sensors.

TDLAS system that can detect a minimum transmission change $\Delta\mathcal{T}_{min}$ as low as $10^{-4} = 0.01\%$ at a given sampling bandwidth, which corresponds

to the effective detector noise floor. This value is a reasonable assumption for average lock-in type measurement systems with negligible spurious reflection interference considering that state-of-the-art lock-in systems can achieve 10^{-6} [35]. Consider toluene gas as the analyte with an absorption cross-section σ_a=$1.5\times10^{-19} cm^2/molecule$ which translates to an absorption coefficient of 5 cm^{-1} at 3.3 µm wavelength in STP conditions. This represents a typical value one could expect in the mid-infrared wavelength range for most trace gases [1]. The absorption coefficient in the near-infrared wavelength range at 1.67 µm is 0.12 cm^{-1}. Assuming that the detection limit corresponds to a SNR of unity, the limit of detection (LOD) is simply calculated with $\mathcal{S}^{-1}\Delta\mathcal{T}_{min}$. The projected, hypothetical best-case scenario results for toluene using record low-loss waveguide platforms are plotted in Figure 2.5 together with the lossless limit $\alpha_L \to 0$ (dashed line). The minimum is achieved when the interaction path length equals 1/e length of the total propagation loss. Even in this hypothetical best-case scenario, it is clear that it is not possible to reach sub-ppm sensitivities by simply downsizing the TDLAS system. Interesting to note that using resonant cavities will not improve the LOD as the effective optical pathlength in resonators is equally bound by optical propagation losses. The limited path length is the main reason for the performance difference between on-chip spectroscopic systems and bulky free-space absorption cells (e.g. Herriott cells), which can reach optical path lengths more than hundred meter with low loss and reflections and hence are suited for ppb-level detection

2.5 Conclusions

Silicon-on-Insulator technology is a mature technology which has enabled complex devices in the near-infrared. There has been significant progress to expand the operating wavelength range beyond the telecommunication band at 1550 nm towards Short-Wave Infrared 2-4 µm applications. In what follows, different spectrometer sensing schemes are proposed based on AWGs to address the performance issue of current integrated SWIR spectroscopic devices. For the most demanding application goals set forth in this work of reaching sub-ppm detection, simply down scaling the spectroscopic TDLAS system is not sufficient. Gas pre-concentration enhancement and/or highly sensitive methods, such as photothermal spectroscopy are therefore explored further in Chapter 5.

References

[1] Jane Hodgkinson and Ralph P Tatam. *Optical gas sensing: a review.* Measurement Science and Technology, 24(1):012004, 2012.

[2] Antonio Rogalski. *Infrared detectors.* CRC press, 2010.

[3] Colin N Banwell, Elaine M McCash, et al. *Fundamentals of molecular spectroscopy*, volume 851. McGraw-Hill New York, 1994.

[4] Laurence S Rothman, Iouli E Gordon, Alain Barbe, D Chris Benner, Peter F Bernath, Manfred Birk, Vincent Boudon, Linda R Brown, Alain Campargue, J-P Champion, et al. *The HITRAN 2008 molecular spectroscopic database.* Journal of Quantitative Spectroscopy and Radiative Transfer, 110(9-10):533–572, 2009.

[5] Barbara Stuart. *Infrared spectroscopy.* Kirk-Othmer Encyclopedia of Chemical Technology, pages 1–18, 2000.

[6] James D Ingle Jr and Stanley R Crouch. *Spectrochemical analysis.* 1988.

[7] R. Soref. *The Past, Present, and Future of Silicon Photonics.* IEEE J. Sel. Top. Quantum Electron., 12(6):1678–1687, Nov 2006.

[8] *Silicon photonics integration at imec.* `https://www.imec-int.com/en/integrated-silicon-photonics`. Accessed: 2019-12-11.

[9] Steven A Miller, Mengjie Yu, Xingchen Ji, Austin G Griffith, Jaime Cardenas, Alexander L Gaeta, and Michal Lipson. *Low-loss silicon platform for broadband mid-infrared photonics.* Optica, 4(7):707–712, 2017.

[10] Wim Bogaerts and Shankar Kumar Selvaraja. *Compact single-mode silicon hybrid rib/strip waveguide with adiabatic bends.* IEEE Photonics Journal, 3(3):422–432, 2011.

[11] Dirk Taillaert, Frederik Van Laere, Melanie Ayre, Wim Bogaerts, Dries Van Thourhout, Peter Bienstman, and Roel Baets. *Grating couplers for coupling between optical fibers and nanophotonic waveguides.* Japanese Journal of Applied Physics, 45(8R):6071, 2006.

[12] Jan Niehusmann, Andreas Vörckel, Peter Haring Bolivar, Thorsten Wahlbrink, Wolfgang Henschel, and Heinrich Kurz. *Ultrahigh-quality-factor silicon-on-insulator microring resonator.* Optics letters, 29(24):2861–2863, 2004.

[13] Tatsuhiko Fukazawa, Fumiaki Ohno, and Toshihiko Baba. *Very compact arrayed-waveguide-grating demultiplexer using Si photonic wire waveguides.* Japanese journal of applied physics, 43(5B):L673, 2004.

[14] Richard Soref. *Mid-infrared photonics in silicon and germanium.* Nat. Photonics, 4(8):495–497, 2010.

[15] M. Muneeb, A. Vasiliev, A. Ruocco, A. Malik, H. Chen, M. Nedeljkovic, J. S. Penades, L. Cerutti, J. B. Rodriguez, G. Z. Mashanovich, M. K. Smit, E. Tourni, and G. Roelkens. *III-V-on-silicon integrated micro - spectrometer for the 3 μm wavelength range.* Opt. Express, 24(9):9465–9472, May 2016.

[16] Sanja Zlatanovic, Jung S Park, Slaven Moro, Jose M Chavez Boggio, Ivan B Divliansky, Nikola Alic, Shayan Mookherjea, and Stojan Radic. *Mid-infrared wavelength conversion in silicon waveguides using ultracompact telecom-band-derived pump source.* Nat. Photonics, 4(8):561–564, 2010.

[17] Ruijun Wang, Muhammad Muneeb, Stephan Sprengel, Gerhard Boehm, Aditya Malik, Roel Baets, Markus-Christian Amann, and Gunther Roelkens. *III-V-on-silicon 2-μm-wavelength-range wavelength demultiplexers with heterogeneously integrated InP-based type-II photodetectors.* Opt. Express, 24(8):8480–8490, 2016.

[18] Gunther Roelkens, Utsav Dave, Alban Gassenq, Nannicha Hattasan, Chen Hu, Bart Kuyken, Francois Leo, Aditya Malik, Muhammad Muneeb, Eva Ryckeboer, Sarah Uvin, Zeger Hens, Roel Baets, Yosuke Shimura, Federica Gencarelli, Benjamin Vincent, Roger Loo, Joris Van Campenhout, Laurent Cerutti, Jean-Baptiste Rodriguez, Eric Tournié, Xia Chen, Milos Nedeljkovic, Goran Mashanovich, Li Shen, Noel Healy, Anna C. Peacock, Xiaoping Liu, Richard Osgood, and William Green. *Silicon-based heterogeneous photonic integrated circuits for the mid-infrared.* Opt. Mater. Express, 3(9):1523–1536, Sep 2013.

[19] Alexander Spott, Jon Peters, Michael L. Davenport, Eric J. Stanton, Charles D. Merritt, William W. Bewley, Igor Vurgaftman, Chul Soo Kim, Jerry R. Meyer, Jeremy Kirch, Luke J. Mawst, Dan Botez, and John E. Bowers. *Quantum cascade laser on silicon.* Optica, 3(5):545–551, May 2016.

[20] G. Z. Mashanovich, G. T. Reed, M. Nedeljkovic, J. Soler Penades, C. J. Mitchell, A. Z. Khokhar, C. J. Littlejohns, S. Stankovic, X. Chen, L. Shen, N. Healy, A. C. Peacock, C. Alonso-Ramos, A. Ortega-Monux,

G. Wanguemert-Perez, I. Molina-Fernandez, P. Cheben, J. J. Ackert, A. P. Knights, F. Y. Gardes, and D. J. Thomson. *Silicon and germanium mid-infrared photonics.* Proc. SPIE, 9755:97550W:1–97550W:6, 2016.

[21] Yu Chen, Hongtao Lin, Juejun Hu, and Mo Li. *Heterogeneously Integrated Silicon Photonics for the Mid-Infrared and Spectroscopic Sensing.* ACS Nano, 8(7):6955–6961, 2014.

[22] Hongtao Lin, Lan Li, Yi Zou, Sylvain Danto, J. David Musgraves, Kathleen Richardson, Stephen Kozacik, Maciej Murakowski, Dennis Prather, Pao T. Lin, Vivek Singh, Anu Agarwal, Lionel C. Kimerling, and Juejun Hu. *Demonstration of high-Q mid-infrared chalcogenide glass-on-silicon resonators.* Opt. Lett., 38(9):1470–1472, May 2013.

[23] Lan Li, Hongtao Lin, Shutao Qiao, Yi Zou, Sylvain Danto, Kathleen Richardson, J David Musgraves, Nanshu Lu, and Juejun Hu. *Integrated flexible chalcogenide glass photonic devices.* Nat. Photonics, 8(8):643–649, 2014.

[24] Z. Han, P. Lin, V. Singh, L. Kimerling, J. Hu, K. Richardson, A. Agarwal, and D. T. H. Tan. *On-chip mid-infrared gas detection using chalcogenide glass waveguide.* Appl. Phys. Lett., 108(14):141106:1–141106:3, 2016.

[25] Ruijun Wang, Anton Vasiliev, Muhammad Muneeb, Aditya Malik, Stephan Sprengel, Gerhard Boehm, Markus-Christian Amann, Ieva Šimonytė, Augustinas Vizbaras, Kristijonas Vizbaras, et al. *III–V-on-silicon photonic integrated circuits for spectroscopic sensing in the 2–4 μm wavelength range.* Sensors, 17(8):1788, 2017.

[26] J Gonzalo Wangüemert-Pérez, Pavel Cheben, Alejandro Ortega-Moñux, Carlos Alonso-Ramos, Diego Pérez-Galacho, Robert Halir, Iñigo Molina-Fernández, Dan-Xia Xu, and Jens H Schmid. *Evanescent field waveguide sensing with subwavelength grating structures in silicon-on-insulator.* Optics letters, 39(15):4442–4445, 2014.

[27] Lionel Tombez, EJ Zhang, JS Orcutt, Swetha Kamlapurkar, and WMJ Green. *Methane absorption spectroscopy on a silicon photonic chip.* Optica, 4(11):1322–1325, 2017.

[28] Katrien De Vos, Irene Bartolozzi, Etienne Schacht, Peter Bienstman, and Roel Baets. *Silicon-on-Insulator microring resonator for sensitive and label-free biosensing.* Opt. Express, 15(12):7610–7615, Jun 2007.

[29] Nannicha Hattasan, Bart Kuyken, Francois Leo, Eva MP Ryckeboer, Diedrik Vermeulen, and Gunther Roelkens. *High-efficiency SOI fiber-to-chip grating couplers and low-loss waveguides for the short-wave infrared.* IEEE Photonics Technology Letters, 24(17):1536–1538, 2012.

[30] M Nedeljkovic, AZ Khokhar, Y Hu, Xia Chen, J Soler Penades, S Stankovic, HMH Chong, DJ Thomson, FY Gardes, GT Reed, et al. *Silicon photonic devices and platforms for the mid-infrared.* Optical Materials Express, 3(9):1205–1214, 2013.

[31] Derek M Kita, Jérôme Michon, Steven G Johnson, and Juejun Hu. *Are slot and sub-wavelength grating waveguides better than strip waveguides for sensing?* Optica, 5(9):1046–1054, 2018.

[32] Yufei Xing, Ang Li, Raphaël Van Laer, Roel Baets, and Wim Bogaerts. *Backscatter Model for Nanoscale Silicon Waveguides.* In 24th International workshop on Optical Wave & Waveguide Theory and Numerical Modelling (OWTNM 2016), 2016.

[33] Michael Belt, Jock Bovington, Renan Moreira, Jared F Bauters, Martijn JR Heck, Jonathon S Barton, John E Bowers, and Daniel J Blumenthal. *Sidewall gratings in ultra-low-loss Si 3 N 4 planar waveguides.* Optics express, 21(1):1181–1188, 2013.

[34] Jared F Bauters, Martijn JR Heck, Demis D John, Jonathon S Barton, Christiaan M Bruinink, Arne Leinse, René G Heideman, Daniel J Blumenthal, and John E Bowers. *Planar waveguides with less than 0.1 dB/m propagation loss fabricated with wafer bonding.* Optics express, 19(24):24090–24101, 2011.

[35] Giacomo Gervasoni, Marco Carminati, and Giorgio Ferrari. *A general purpose lock-in amplifier enabling sub-ppm resolution.* Procedia Engineering, 168:1651–1654, 2016.

3

Integrated dispersive AWG spectrometers

In the context of telecommunication, high data rate links are established across a common single fiber by sending information over different spectral channels simultaneously. At some point in this data link, separate wavelengths have to be combined or split apart with wavelength (de)multiplexers (WDM). For optical spectroscopy using a broadband light source, the same devices can be used to retrieve the absorption spectrum by analyzing the spectral channels. Moreover, the multiplexing capability can be used to combine multiple narrowband laser source array for high spectral resolution applications. This chapter deals with novel AWG system architectures, such as the single pixel AWG configuration for short-wave mid-infrared applications.

Contents

3.1 Introduction

Commercial spectroscopy instrumentation use either prism- or grating-based elements for wavelength separation and these can be quite large in size to achieve sufficient resolving power. Additionally, the cost can easily go up to more than 100 thousands dollars per device for the mid-infrared wavelength range (2-4 µm) [1]. For spectroscopy applications involving broad absorption features such as liquids and solids, the most cost-efficient solution includes a broadband light source and a suitable spectrometer to analyze the spectral response, see also Figure 2.4 in the previous chapter. As an example, the typical 3 dB-bandwidth of absorption features of a liquid such as sesame oil at 3.4 µm and an organic solid such as polydimethylsiloxane (PDMS) in the 2.3 µm region would be about 900 GHz (35 nm) and 1300 GHz (50 nm), respectively [2].

A spectrometer resolution $\Delta\nu$ of at least 100 GHz would be adequate in both cases. It is common to refer to the resolution of a spectrometer in terms of its resolving power R

$$R = \lambda/\Delta\lambda \tag{3.1}$$

with $\Delta\lambda$ the distance between two neighbouring spectral lines that are just distinguishable (Rayleigh criterion) [3]. This allows different spectrometers to be compared in terms of resolving strength of, irrespective of the wavelength of operation. In a typical grating-based spectrometer, it can be shown that the resolving power is a function of the grating diffraction order m and the number of illuminated grating periods N:

$$R_{grating} = mN = OPD_{max}/\lambda \tag{3.2}$$

where OPD_{max} is the maximum optical path difference between the outer rays on the grating [3]. This relationship is often expressed in the following form in literature

$$\Delta\lambda = \frac{\lambda^2}{OPD_{max}} \tag{3.3}$$

From the above, to achieve better resolution for high-demanding spectroscopy applications it is beneficial to operate the grating in a high diffraction order m. This finding has led to the development of reflective *Echelle* or 'staircase'-like gratings, where the grating tooth shape and orientation (blazed angle) is optimized to maximize the diffraction order and the number of illuminated grating periods [4]. Resolutions on the order of 10^6 have

been achieved for astronomy applications using large echelle gratings [5]. In comparison, for the example given above, a resolving power of 10^3 would already be sufficient to adequately probe and distinguish the spectrum of sesame oil at 3.4 µm.

By operating in a high grating order, there is an inherent trade-off with the free spectral range (FSR) of the device, the wavelength difference over which consecutive diffraction orders $(m-1, m+1)$ direct light into the same direction. The FSR of a grating device is equal to λ/m such that the maximum operating wavelength range or bandwidth of a spectrometer is inversely proportional to the resolving power. Additionally, coarse wavelength filters can be used to distinguish between consecutive FSR wavelength ranges. The astronomy and liquid examples above show that the spectrometer design should be optimized for the task at hand. The planar waveguide analogy of this grating is often called a Planar Concave Grating (PCG). In the next section, the development of a different type of spectrometer is discussed.

3.2 Arrayed Waveguide Grating spectrometer

A different approach to efficiently disperse the light into its components is used in arrayed waveguide grating design, which sometimes is also called a phased array. The core principle is similar to phased arrays used in radar-technology where the phase front of the transmitted (received) radio signal can be manipulated to focus the signal to a different point by controlling the phase difference between the antenna units in the array. In an AWG, the incoming light is split among different optical waveguides (the waveguide array) using an input aperture. The waveguides have increasing length, such that the path length difference between the waveguides equals an integer multiple of the central wavelength. At this wavelength, light in the separate waveguides will arrive at the output aperture in phase and the phase front at the output aperture will mimic the divergent field at the input aperture. Light at the output aperture will focus to a point at the same relative position as the input waveguide in the input aperture. Due to the linear increase in waveguide length, wavelength dispersion will change the phase relationship between the waveguides in a linear fashion such that at wavelengths different from the central design, the output phase front will be tilted, focusing the beam to a different point on the image plane. By providing receiving waveguides at the corresponding focal points, spatial separation of wavelengths is achieved. As in the case of Echelle gratings, the resolution will depend on OPD_{max}, the distance between the longest and shortest waveguide in the array [3].

In recent years, considerable effort has been devoted to develop a compact, integrated version of Echelle- and AWG-based spectrometers on a photonic IC [6, 7]. It was also demonstrated that it is possible to realize AWG-based [8–10] and PCG-based [11] spectrometers in the SOI platform for the 2-4 µm wavelength range. In addition, AWGs can also be used as multiplexers for DFB laser arrays. Combing a mid-infrared DFB laser array with an AWG would allow the coupling of light from different lasers (with a narrow tuning range) to a single diffraction limited output waveguide with low loss [12]. More practical guidelines on how to design AWGs can be found in [3, 4, 8, 13].

A microscope picture of an SOI AWG operating in the 2.3 µm wavelength range is shown in Figure 3.1(a). The footprint of the device is 0.45 mm^2. Figures 3.1(b)-(d) show the measured transmission spectra of three AWG spectrometers operating at different wavelengths. The filters are fabricated on a 200 mm SOI wafer with a 400 nm thick crystalline Si device layer and 2 µm buried oxide layer thickness. Rib (ridge) waveguides and grating couplers are defined with a 180 nm deep etch and are cladded with SiO_2 and planarized down to the silicon device layer. The waveguide loss is around 0.5 dB/cm in the 2-2.5 µm wavelength range and increases to 2.6 dB/cm at 3.3 µm and 3 dB/cm at 3.8 µm [10]. Low insertion loss (2 to 3 dB) and low crosstalk (30 to 20 dB) are obtained in all of the AWG spectrometers. This state-of-the-art performance of the AWG spectrometers indicates that the SOI waveguide platform is optimally poised for SWIR/MWIR (1-4 µm) dispersive spectroscopy applications [1].

3.3 AWG with integrated photodetectors

For a spectroscopic sensor, the passive spectrometer should be integrated with photodetectors to convert the optical signals to an electrical response. In addition, the photodetectors should connect with electronic components such as trans-impedance amplifiers (TIA) to realize a complete opto-electronic system.[2]

SWIR AWG-spectrometer

Figure 3.2(a) displays a microscope image of the 2.3 µm AWG spectrometer

[1] The MWIR portion from 4-5 µm cannot be covered by the SOI platform using the same methodology due to buried oxide absorption. It is possible to extend the SOI platform further by under-etching the silicon device layer creating free-standing silicon waveguides.

[2] Disclaimer: section 3.3 has been largely the work of M. Muneeb and R. Wang but is included for continuity. The measurements and analysis of the 3.8 µm integrated AWG were carried out by the author.

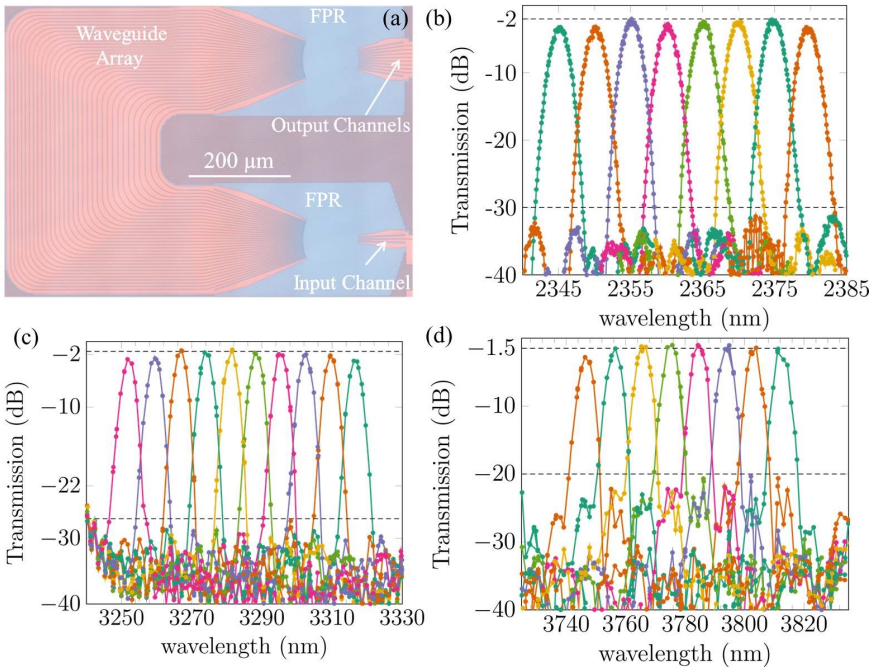

Figure 3.1: Microscope image of a 2.3 µm AWG spectrometer (a); the measured spectral responses of all the channels in three AWGs operating at different wavelengths: 2.3 µm (b), 3.3 µm (c) and 3.8 µm (d) [10]

integrated with an adiabatically-coupled InP-based type-II quantum well photodetector array [14]. Every channel of the AWG is integrated with a photodetector spaced 60 µm apart. In order to interface with the electronic components, the III-V-on-silicon spectrometer is wire bonded to a printed circuit board (PCB), as shown in Figure 3.2(b). A reference photodetector is present on a reference silicon waveguide to estimate the insertion loss of the AWG after heterogeneous integration. Figure 3.2(c) shows the photo-response of the 2.3 µm III-V-on-silicon spectrometer. During the measurement, the bias voltage is fixed at -0.5 V. An insertion loss of 3 dB and crosstalk level of -27 dB is obtained by normalizing the responsivity to the reference photodetector. This result indicates that the bonding of III-V material on silicon and related post-processes do not degrade the performance of the AWG spectrometer.

MWIR AWG-spectrometer

To extend the operation wavelength of the III-V-on-silicon AWG spectrometer beyond 3 µm, a heterogeneously integrated InAsSb photodetector was

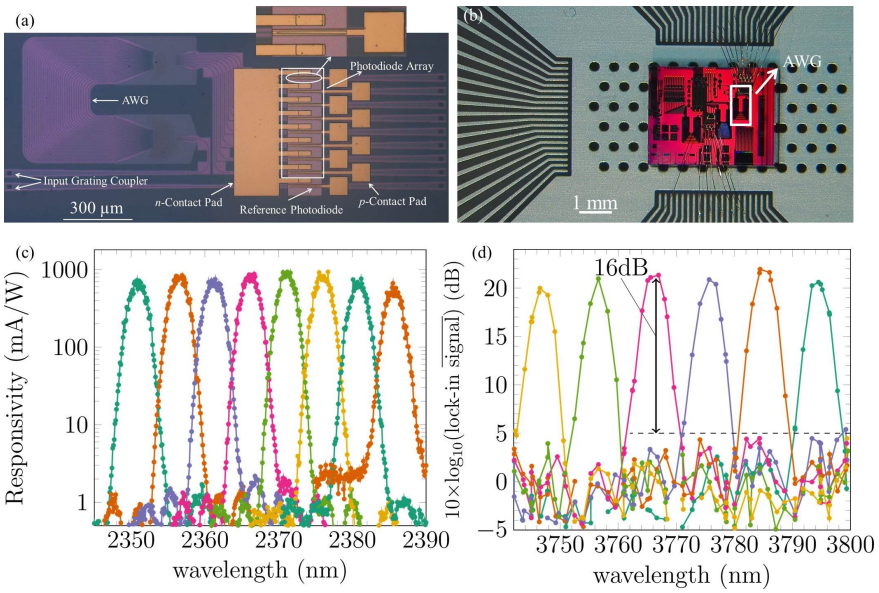

Figure 3.2: Microscope image of the 2.3 µm *AWG spectrometer integrated with a InP-based type-II quantum well photodetector array (a), wire bonded III-V-on-silicon AWG spectrometers on a PCB (b), photo-response of the SWIR (2.3* µm*) AWG (c) and MWIR (3.8* µm*) III-V-on-silicon AWG spectrometer (d). [10]*

developed [15]. By transferring $InAs_{0.91}Sb_{0.09}$ on silicon, a III-V-on-silicon photodetector was realized with a responsivity of 0.3 A/W at 3.8 µm wavelength and a dark current of 170 μA under a bias of -10 mV and 600 μA at -50 mV at room temperature [16].

The optical characterization of devices in the MWIR range is more involved due to the unavailability of widely tunable, fiber-coupled sources. Moreover, it is not possible to use the same telecom optical fibers to characterize the devices. For this purpose, special ZrF_4 single-mode fiber pigtails were used instead [17]. The measurement setup is shown in Figure 3.3. Mid-infrared light from an optical parametric oscillator (OPO) system (Aculight 2400) is routed using a free-space optical setup. The polarization of the light is adjusted to TE using a Babinet-Soleil compensator. The beam is chopped and coupled to a single-mode ZrF_4 fiber after which it is vertically coupled to the PIC under a 15 degrees angle. To compensate for slow fluctuations of the OPO output power, the photodiode response is normalized using a thermopile detector (Thorlabs S401C), which monitors a fraction of the output power in free space. The integrated photodiode response is measured using a pre-amplifier from Infrared Associates (InSb-1000) at

zero bias. To increase SNR, the output of the pre-amplifier is connected to a lock-in amplifier (LIA) (SR 830). To precisely control the wavelength of the OPO unit, custom hardware was built in the workshop that precisely controls the position of the nonlinear crystal using a stepper motor. Further, a python script adjusts the seed laser wavelength and orientation of the intra-cavity etalon of the OPO unit together with the crystal position to realize optimal wavelength tuning. The OPO automation is based on the work presented in [18] and contains further details. The wavelength is measured using a free-space wavemeter (Bristol 621) and the wavelength step of the experiment is approximately 1 nm.

To remove any measurement fluctuations, ten consecutive readings from the LIA are collected per wavelength point. These readings are then averaged and normalized with respect to the average of the reference power measured by the thermopile detector. Due to the relatively large dark current, optical measurements in DC (without chopper modulation) do not reveal the AWG response clearly. Figure 3.2(d) shows the measured photoresponse of the 3.8 µm integrated MWIR spectrometer. A crosstalk of -16 dB was achieved. It is believed that the dark current can be further reduced by adding barriers in the epitaxial layer stack and by further optimizing the detector passivation [15].

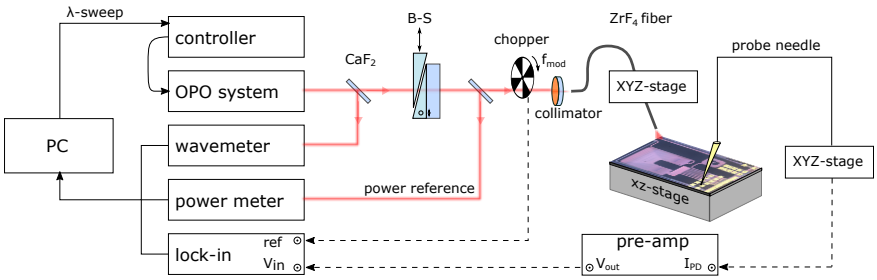

Figure 3.3: Schematic of the optical measurement setup used to characterize the integrated MWIR spectrometer at 3.8 µm *[15].*

3.4 High-resolution AWG

For most sensing applications, high resolution AWGs are beneficial both for TDLAS and dispersive spectrometer systems based on broadband light source. In the former case, multiple laser lines can be multiplexed together to form a single diffraction-limited multi-frequency laser beam, sometimes also called a laser 'engine', which can analyze multiple gas species at once. For example, an array of InP-based DFB laser arrays in the SWIR was

demonstrated with possible applications for CO, NH_3 sensing [19]. Further, mid-infrared quantum cascade- or (QCL) interband cascade- laser (ICL) sources can be used to probe the MWIR/LWIR absorption spectrum [20]. In both cases, each element of the array is a DFB laser which can be thermally tuned over a narrow wavelength range. By small alterations in the fabrication process an array of lasers with different emission wavelengths is fabricated. For practical compact applications it would be beneficial to couple such an array to a single diffraction limited beam using an integrated wavelength multiplexer.

In the case of a lower cost broadband source, analytes such as liquids and solids with broad absorption features can be identified. In one particular case, the methane absorption line at 3.3 µm at room temperature and atmospheric pressure has a relative large FWHM which can still be discerned with a 50 GHz AWG spectrometer which will be explained in more detail in a latter section.
In this context, the resolution of an AWG is considered 'high' if it is capable of resolving individual absorption features or laser engine channels for a particular application.
As apparent from equation (3.3), a high resolution AWG will require longer delay lines (and more of them), which in turn decreases the performance of the device due to phase errors. As the light propagates in the long waveguides, phase errors are accumulated along the path leading to a distorted phase front at the output aperture. The main origin of the phase errors is attributed to small dimensional variations of the waveguide cross-section along the path such as sidewall roughness. Fortunately, in the SWIR/MWIR region of interest, the accumulated phase errors in the waveguide array are less pronounced than in the telecom range because the dimensional variations are progressively smaller compared to the wavelength of the light. Furthermore, the waveguide array portion of the AWG features transitions to expanded waveguides to further reduce the imperfections at the silicon-glass interface.

As an example, different high resolution AWG designs at 3.3 µm with different channel spacings from 200 GHz (7.3 nm) to 50 GHz (1.8 nm) were fabricated.

Experiments
The AWGs have six channels with four different channel spacings {200,140,80,50} GHz, which is equivalent to the spectral resolution of the spectrometer. These four filters have the same star coupler aperture design which is defined by the parameters in table 3.1.
The filters are characterized by using the same optical setup as in Figure

No. of arrayed waveguides	32
free propagation length (µm)	130
waveguide width (µm)	1.125
expanded WG width (µm)	2.2
taper length (µm)	75
bend radius (µm)	50
aperture width (µm)	3.25
arrayed WG spacing (nm)	250

Table 3.1: High-resolution MWIR AWG design parameters, detailed explanation of quantities can be found in [8]

3.3, but now with two single-mode fibers. After going through the PIC, light from the second fiber pigtail illuminates a liquid nitrogen (LN) cooled InSb detector. The LIA now measures the response of this detector at the modulation frequency of the chopper. The AWG response is normalized to the spectrum of a reference waveguide and the results are shown in Figure 3.4. The insertion loss of all four AWGs is between 2 and 3 dB. The crosstalk level, defined here as the highest contribution of unwanted signal within any channel, is better than 20 dB for all four designs.
The waveguide loss is estimated by using a set of four spirals with increasing length from 0.65 cm to 5.5 cm. The waveguide loss at 3.3 µm is estimated to be 2.6±0.2 dB/cm. It is worth noting that after a few days of exposure to ambient air, as opposed to controlled cleanroom environment, the waveguide loss increased to 4.5 dB/cm due to organic contamination from air on the PIC. The loss was decreased back to nominal values by cleaning the chip with acetone and a 15 min O_2 plasma treatment. The performance of the AWGs was further unaffected by the increased loss.

The star coupler aperture is a critical component of the AWG, four different combinations of the star coupler aperture width {2.45,3.25,4.50,6.00} µm and free propagation range {80,130,235,395} µm were investigated for the 200 GHz AWG. The performance variations were found to be insignificant: the insertion loss is -2 dB and the crosstalk varies between 20 and 24 dB.

Conclusion
High resolution MWIR AWGs operating at 3.3 µm can be fabricated in the SOI waveguide platform with low insertion loss, good crosstalk levels and low waveguide loss. AWGs with 50 GHz spacing can potentially be used

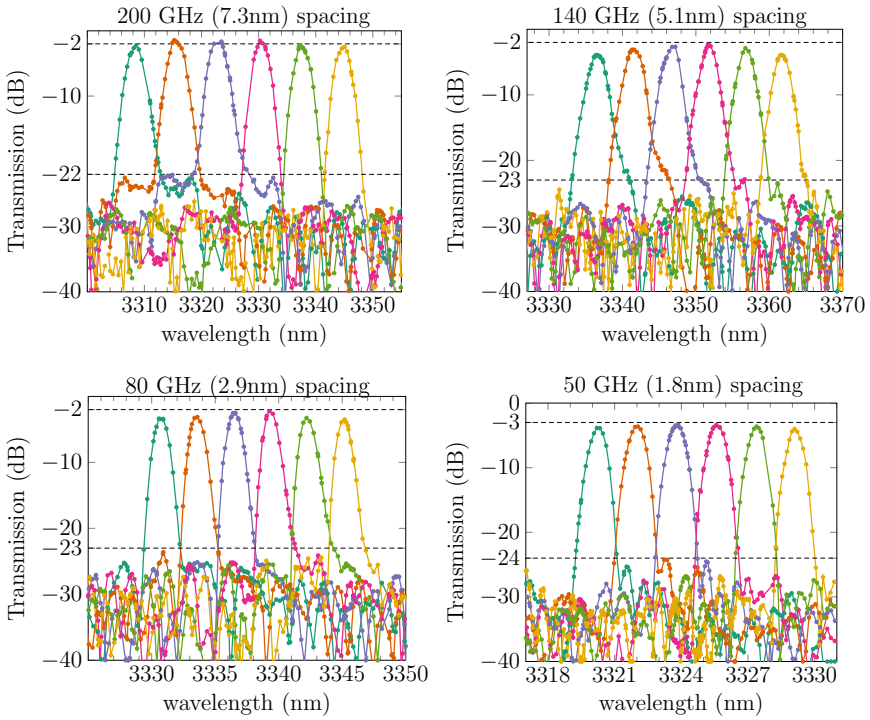

Figure 3.4: Transmission normalized to a reference waveguide of four different SOI AWGs operating in the 3.3 µm *wavelength range. The insertion loss (2-3 dB) and crosstalk levels (20-21 dB) are indicated by the dashed lines.*

as an integrated multiplexer for a future compact laser array spectroscopy system or directly as a spectrometer of broad absorption features such as CH_4 at 3.3 µm. The fabrication tolerances and optimal star coupler design parameters are less stringent than at telecom wavelengths due to the increased optical mode at longer wavelengths. The sidewall roughness at the silicon-glass interface is less pronounced. Further, care must be taken to avoid organic contamination of the PIC surface, any compound containing (C−H)-bonds will dramatically reduce optical transmission through the waveguide. A typical absorption coefficient of organic compounds is in excess of 100-1000 cm^{-1}.

3.5 Single Pixel AWG Spectrometer

3.5.1 Introduction

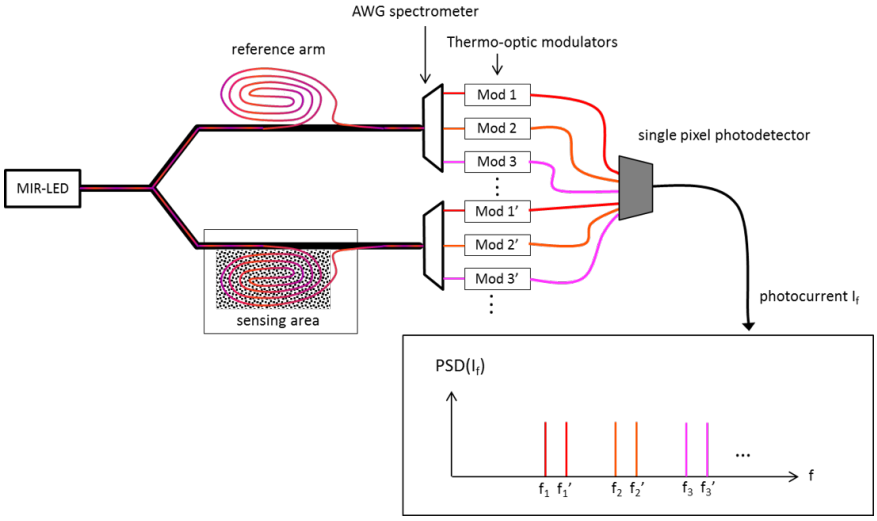

Figure 3.5: Schematic of the single pixel spectroscopy architecture. A mid-infrared broadband source (e.g. operating in the SWIR/MWIR range) is split into a sensing and a reference arm on a photonic IC. After analyte interaction, the output channels of the AWG are amplitude-modulated time-sequentially or at different modulation frequencies. All output channels illuminate a single high performance photodiode simultaneously. Fourier analysis of the time-dependent PD response is further analyzed to retrieve the spectral content of the individual channels.

Section 3.3 shows that integrated III-V photodetector arrays in the MWIR range suffer from large dark currents and are not yet on-par with dis-

crete commercially available, cooled photodetectors. It is therefore useful to explore different sensing architectures that reduce the number of required photodetectors and lower the constraints on overall PIC packaging. The decoupling of the detection functionality from the PIC yields the possibility to use advanced methodologies such as lens immersion, vacuum and (cryogenic) cooling to increase the sensitivity of the device. Furthermore, the packaging and direct integration of MWIR sources on SOI PICs is an ongoing research topic [21, 22] and the field can benefit from alternative packaging strategies. In this context it is believed that the overall size of the device can still be made sufficiently compact and easy to manufacture to justify the following integration approach.

The key approach taken here is to time-multiplex the spectral channels of the MWIR spectrometer on a single photodiode. The schematic of the single pixel spectroscopy architecture is shown in Figure 3.5. A broadband source operating in the SWIR/MWIR range is split into a sensing and a reference arm on a photonic IC. After analyte interaction, the output channels of the AWG are amplitude-modulated time-sequentially or at different modulation frequencies. All output channels illuminate a single high performance photodiode simultaneously. Fourier analysis of the time-dependent PD response is further analyzed to retrieve the spectral content of the individual channels [23].

A demonstration of a single pixel SOI-based AWG spectrometer operating in the SWIR range is given below. A single standard thermistor outline (TO)-can packaged InGaAs PIN photodiode is integrated with a twelve channel AWG with 225 GHz (4 nm) channel spacing. In order to distinguish the different channels, the output arms of the AWG are modulated using on-chip balanced Mach-Zehnder interferometers (MZIs) by thermal tuning [24]. To showcase the miniaturized-spectrometer, the absorption spectrum of PDMS in the 2.3 µm wavelength range is recovered.

3.5.2 Fabrication

The AWG is fabricated on the same 400 nm SOI platform previously mentioned. A thin 0.9 µm layer of SiO_2 is deposited on top. 100/10 nm thick Ti/Au resistors are defined on the arms of the modulators. The resistors measure 200x2 μm^2 and realize a π-phase shift with $\approx$ 50 mW of power dissipation. As a final step, the chip is passivated with a benzocyclobutene (BCB) polymer layer. The circuit is designed for 2.3 µm wavelength and TE polarized light. The AWG has twelve channels with 225 GHz (4 nm) channel spacing and an FSR of 3150 GHz (56 nm). The MZI modulators of the photonic chip are wire bonded to a printed circuit board (PCB) and are addressed by a home-built 16-bit current source through USB. An uncooled

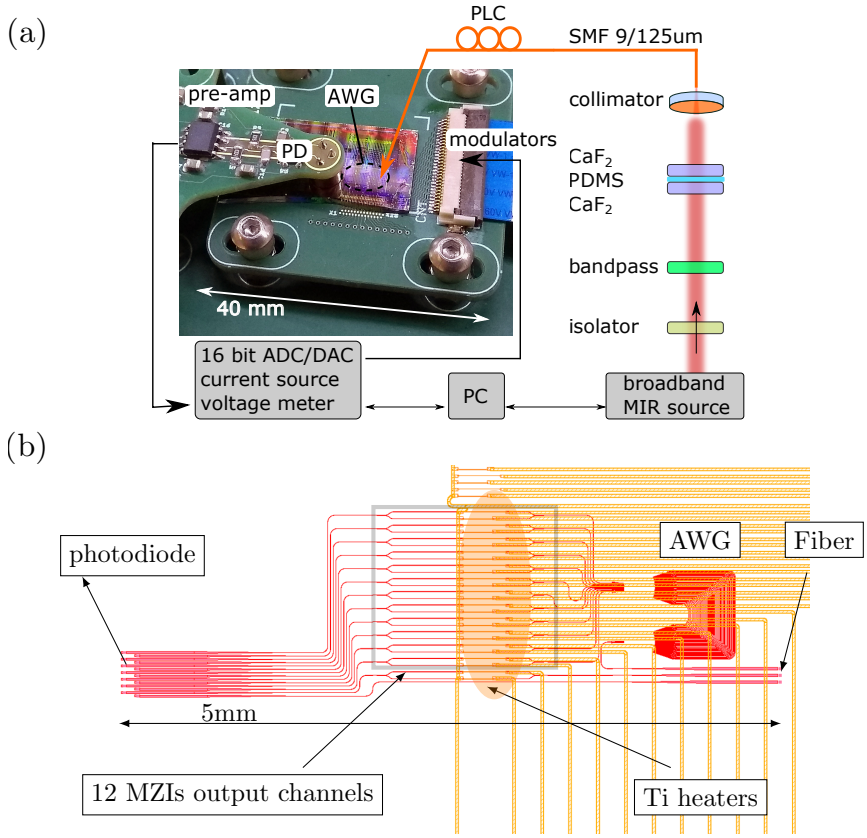

Figure 3.6: Schematic of a SWIR PIC spectrometer experiment using a single external detector (a). A Cr^{2+}:ZnS laser working in ASE mode with a bandpass filter is used as the broadband mid-infrared source to determine the absorption spectrum of a 0.5 mm thick PDMS sheet. After interaction, the light is coupled to a standard 9/125 fiber pigtail. The TO-can with the photodiode is positioned directly on top of the output grating couplers of the chip and collects all twelve output channels of the AWG simultaneously. Design layout of the AWG (b). The output channels are modulated time-sequentially using (balanced) MZI thermo-optic modulators. A π-phase shift in each channel is achieved by dissipating $\approx$ 50 mW power above the optical waveguide using Ti/Au heaters.

Hamamatsu G12183-010K PIN photodiode (PD) is fixed to a pre-amplifier PCB with a variable gain up to 10^6 V/A. The electronics to drive the modulators and read the photodiode response are based on readily available off-the-shelf components. The PD is manually positioned and fixed 0.5 mm above the output grating coupler array of the AWG, see Figure 3.6(a). The output grating array covers an area of 300x140 µm^2 and all the channels

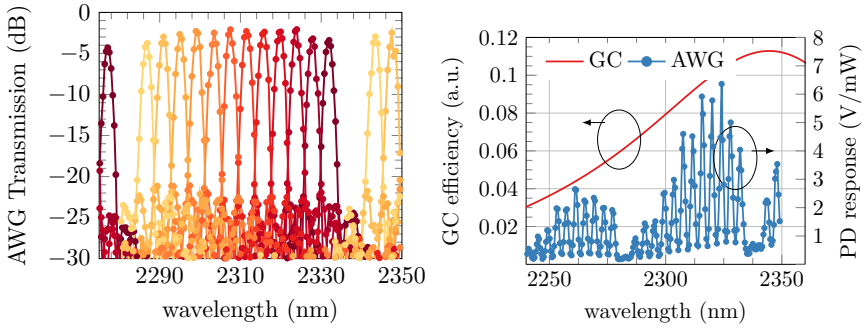

Figure 3.7: The AWG channels from layout Figure 3.6(b) are characterized using a single-mode tunable CW laser and normalized to a reference waveguide (a). The channel spacing is 225 GHz (4 nm) and one FSR spans 3150 GHz (56 nm). The insertion loss is around 2 dB and the crosstalk between channels is 20 dB. The output light is collected with a single mode fiber and the power and wavelength are obtained with an OSA. The grating coupler efficiency is estimated from the reference waveguide measurement (b). The insertion loss is 9 dB at 2340 nm peak wavelength and 18 degrees fiber coupling angle. The AWG response, normalized to the optical power in the fiber, is obtained from all channels simultaneously by using the TO-can PD as the detector. The PD response follows the GC efficiency curve and all twelve channels are visible. An additional envelope is observed due to limited dimensions and exact position of the PD on top of the output GC array.

are simultaneously collected by the photosensitive area of the PD, 1 mm in diameter. The PD response is read-out using the aforementioned 16-bit ADC. A microcontroller is programmed to send the read/write commands in blocks with a resulting PD sampling rate of approximately 24 kSa/s. A 0.5 mm thick PDMS foil was prepared using the Sylgard 184 (10:1) elastomer kit and a suitable mold.

3.5.3 AWG characterization

The performance of the photonic circuit is characterized using a CW single mode Cr^{2+}:ZnS solid state laser (IPG Photonics). The free space output power from the laser is coupled to a standard 9/125 µm single mode fiber as in Figure 3.6(a) but without the bandpass filter, PDMS and PD. The power in the fiber is between one and few tens of mW depending on the laser wavelength. A second single mode fiber collects the output light from the PIC and an optical spectrum analyzer (OSA) (Yokogawa AQ6375) was used simultaneously as a sensitive detector and wavelength meter. A

cooled extended InGaAs photodetector (Thorlabs PDA10DT) was used as a reference, connected to a 1/99 fiber splitter to compensate for slow time-fluctuations of the laser power. The AWG response with the MZI modulator arms is normalized to a reference waveguide and the results are shown in Figure 3.7(a). The channel spacing is 225 GHz (4 nm) and one FSR spans 3150 GHz (56 nm). The insertion loss is around 2 dB and the crosstalk between channels is 20 dB. The grating coupler efficiency is calculated to be around -9 dB/GC at 2340 nm peak wavelength with 18 degrees fiber coupling angle, see Figure 3.7(b). By switching the output fiber with the single pixel PD, the combined response of the AWG channels is retrieved. The PD voltage is normalized to the power in the fiber towards the chip, calculated using the laser source reference detector. All twelve channels are clearly distinguishable. The combined AWG response follows the grating coupler trend with an additional envelope. The relative position of the output GC array to the PD and the finite aperture of the PD determine this envelope, see also Figure 3.6(a). When the PD is positioned in the center of the GC array, the outer channels are captured less efficiently. The position of the PD is fixed with M4 screws and can be readjusted along x- and y-slits.

The MZI modulators are characterized using the same method as above but now the wavelength is fixed to peak transmission of each AWG channel and electrical power is dissipated through the resistor on the corresonding arm of the MZI. The increased local temperature of the Si waveguide induces a change in effective index through the thermo-optic effect. The applied voltage and power are set with a voltage source (Keithley 2400), see Figure 3.8(a). The resistance is approximately 1200 Ω for all heaters and the extinction ratio is more than 30 dB. A π-phase shift is obtained when P_π=49 mW power is dissipated. In the spectroscopy experiment where all twelve channels are collected simultaneously by the PD, the dissipated heat P_π on one channel causes a drop of $1.5/1.68 \approx 11/12$ of the amplified PD response as expected, see inset in Figure 3.8(a). Due to small variations in fabrication, P_π varies between 48-56 mW and the corresponding V_π between 6-7 V for the 12 channels of the AWG.
The AWG channel transmission is shown when the heater is switched on $V = V_\pi$ and when it is off $V = 0$, see Figure 3.8(b). The pitch between the MZI channels is 100 µm and no thermal cross-talk between adjacent channels was observed and therefore must be lower than the optical crosstalk of the AWG, see Figure 3.7(a).

3.5.4 Absorption spectroscopy of PDMS

To showcase the single pixel mini-spectrometer, the absorption spectrum of PDMS in the 2.3 µm wavelength region is probed using three different

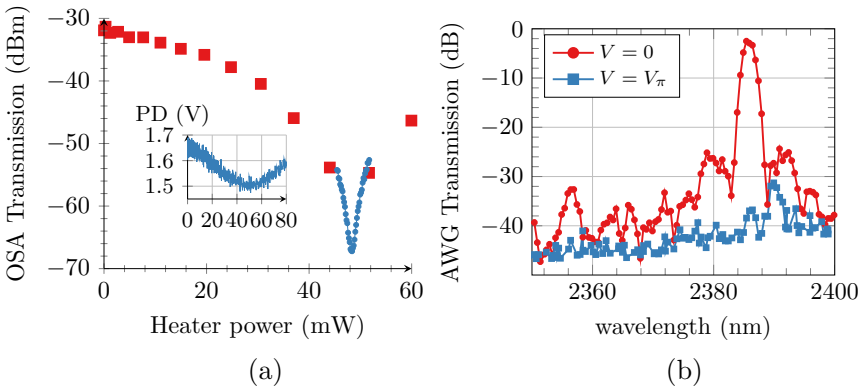

Figure 3.8: The characterization of a MZI modulator as a function of dissipated power is shown for one channel of the AWG (a). A coarse and a fine voltage sweep is performed to find the minimum transmission of the channel at 2386 nm wavelength. The inset shows the amplified PD response as a function of dissipated heat on one channel when all twelve channels are collected simultaneously by the single pixel for the setup as in Figure 3.6. The resistance is approximately 1200 Ω for all heaters and the extinction ratio of the MZI is more than 30 dB. A π-phase shift is obtained when P_π=49 mW power is dissipated. Due to small variations in fabrication, P_π varies between 48-55 mW and the corresponding V_π between 6-7 V for the 12 channels of the AWG. The channel transmission is shown when the heater is switched on ($V = V_\pi$) and when it is off ($V = 0$) (b).

methods. First, the absorption spectrum is determined using an FTIR (Agilent 680) benchtop spectrometer in transmission, see Figure 3.9(a). The importance of the 2-3 µm wavelength range is indeed also valid in this case as can be seen from the increased absorption cross section as compared to the 1.5-2 µm wavelength range.

Secondly, the PDMS sheet is placed between two 4 mm thick CaF_2 windows in the beam path of the Cr^{2+}:ZnS laser operating in amplified spontaneous emission (ASE) mode. The fiber coupled power is measured by the SWIR OSA with 0.1 nm resolution both with (PDMS), and without (Ref) the PDMS sample. The measured total optical power is 11.5 µW and 31.4 µW respectively. When PDMS is introduced in the beam path, the collimator has to be realigned to a new optimum. The spectrum shows spectral ripple due to residual thin film interference effects of the bandpass filter. The normalized FTIR transmission of the PDMS sample and the bandpass filter is also shown in Figure 3.9(b).

Lastly, the AWG is used as a dispersive spectrometer to recover the response of PDMS at the AWG peak wavelengths, marked as black crosses on the top

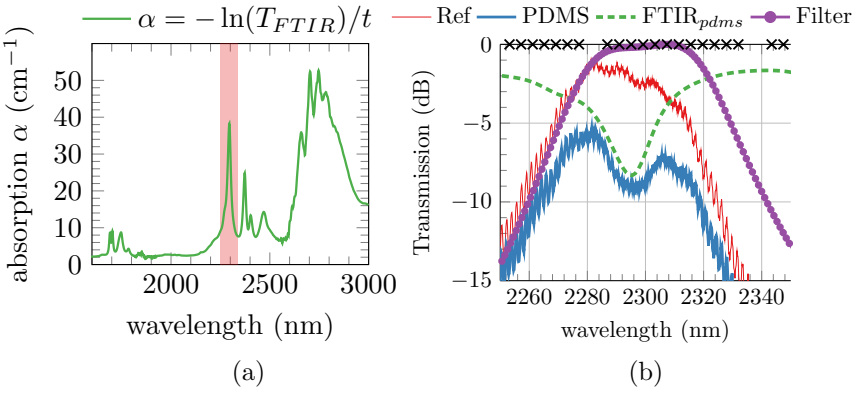

*Figure 3.9: The absorption coefficient of PDMS in the near- to mid-infrared wavelength region is estimated using the Lambert-Beer law and the FTIR transmission spectrum of a (t =0.5 mm) thick PDMS foil (a). The wavelength region for the AWG spectroscopy experiment is colored. After passing the bandpass filter, see also Figure 3.6(a), the optical spectrum coupled into the fiber is measured using the OSA: in the case when PDMS is present (**PDMS**) and when it is removed (**Ref**) (b). The measured total optical power is 11.5 μW and 31.4 μW respectively. The normalized FTIR transmission of the PDMS sample (**FTIR**$_{pdms}$) and the bandpass (**Filter**) is also shown. The black crosses on the top axis show the AWG peak wavelengths. The OSA measurements are shifted by +30 dB for clarity.*

axis in Figure 3.9(b). Ideally, the AWG response would be limited to within one FSR closest to the PDMS absorption feature. The available bandpass filter is centered at 2305 nm with a Full Width at Half Maximum (FWHM) of 50 nm and overlaps unintentionally with the next FSR on the blue side of the PDMS absorption peak. As a result, the longer wavelength channels of the AWG spectrometer will show additional crosstalk.

The combined output from the channels of the AWG results in a PD signal of 3.7 V for the reference measurement and 1.4 V when PDMS is introduced. The optical power inside each channel can be recovered by modulating each channel time-sequentially. The modulation depth of the heaters is chosen such that it corresponds closely to a π-phase shift for each MZI. Slight differences in fabrication lead to drive voltages V_π that are spread between 6 and 7 V and the corresponding switching power varies between 48-56 mW. An example of modulation of one such channel is shown in Figure 3.10(a). For each heater bias point, four consecutive PD value are collected and averaged. The PD output is collected for 1 second for each channel consecutively with a sampling rate of 24 kSa/s. This corresponds to the response to 50 sinusoidal heating cycles for each channel. After sweeping the twelve

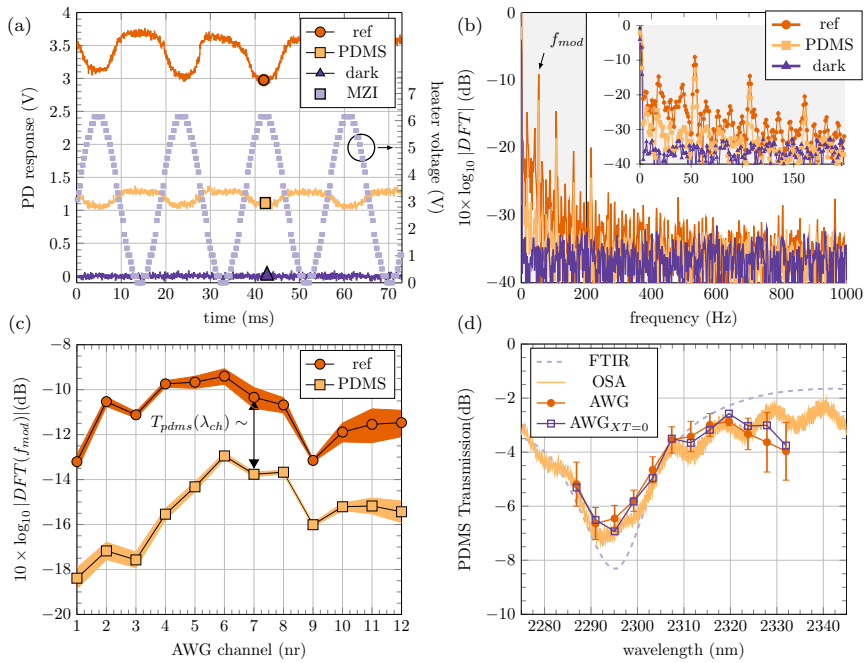

Figure 3.10: Response of the PD to a sinusoidal modulation of one AWG channel. The first thousand sample points are shown for three cases: prior to the chip, the light passes through a 0.5 mm thick PDMS sheet, a reference measurement without PDMS and a dark measurement without the light source (a). The sample points are collected by a microcontroller with an approximate sampling rate of 24kSa/s. The logarithmic DFT spectrum of the PD response is shown (b). The difference in maxima between the 'PDMS' and 'ref' measurement at the modulation frequency f_{mod} is used to determine the spectral response of PDMS at the peak wavelength of each AWG channel (c). The colored region boundaries are the $\mu \pm \sigma$ values for seven different measurements. The optical modulation depth difference of the PD between the PDMS and reference measurement is plotted for each AWG channel with the corresponding channel peak wavelength (d). The results agree well with the results obtained by measuring the PDMS transmission using the benchmark SWIR OSA. Main cause of variation is power and alignment drift of the source to the spectrometer. Taking the OSA spectrum as the true response of PDMS in this setup, calculations show that an idealized AWG with zero crosstalk XT would produce almost identical results.

channnels of the AWG, the discrete Fourier Transform (DFT) of the signal is performed on the four-piece averaged output using the fast-fourier transform (FFT) algorithm with a Kaiser smoothing window. The result for one channel is shown in Figure 3.10(b). The absolute value of the DFT

spectrum at the modulation frequency is proportional to the optical power modulation of that channel. This value is obtained for each of the twelve channels for the case when there is no PDMS in the free space beam path and when it is introduced (ref), see Figure 3.10(c). The difference between the two is a measure for the absorption spectrum of PDMS, sampled at the peak wavelengths of the AWG channels. The colored region boundaries are the $\mu \pm \sigma$ values for seven different measurements where the main cause of variation is power and alignment drift of the source to the spectrometer. The absorption spectrum of PDMS obtained in this manner corresponds well to the OSA benchmark measurement, see Figure 3.10(d). A slight discrepancy for the longer wavelength channels is observed as expected. This is due to the fact that the central wavelength of the bandpass filter is not exactly centered to one FSR of the AWG, see Figure 3.9(b). Taking the OSA spectrum as the true response of PDMS in this setup, calculations show that an idealized AWG with zero crosstalk and insertion loss would produce almost identical results. The idealized AWG is taken as an array of dirac functions centered at the AWG channel peak positions, see black crosses in Figure 3.9(b).

The SNR for each channel of the system is found by comparing the signal strength at the modulation frequency in the reference measurement with the noise power in dark conditions at f_{mod}, see Figure 3.10(b). The SNR is between 24-28 dB for 1s integration time per channel. Using the input optical power spectrum from Fig.3.9(b) and the SNR for each channel, it is estimated that the lowest power change ΔP that can be detected (with SNR=1) is between -57.2 dBm/nm and -69.2 dBm/nm. For a given spectroscopic application where one would want to detect a minimum transmission change ΔT of 0.1% (-30 dB) with SNR=1, a broadband source with a minimum power density of -27.2 dBm/nm or a total power of ≈-10 dBm within one FSR (50 nm) is required . Although these values are adequate for most applications, there are several ways to further improve the performance of the device.

The detectivity of the photodetector can be increased by active cooling or by using an optical immersion microlens [25]. The input grating coupler can be replaced with a spot-size converter for edge-coupling for higher efficiency and larger optical bandwidth. Moreover, the input fiber should ideally be permanently glued to the PIC to avoid drift of the coupling efficiency to the spectrometer during the measurement.
As indicated in Figure 3.5 The channels can be addressed simultaneously at a different modulation frequency instead of time-sequentially, thus increasing the measurement time per channel, thereby increasing SNR. For testing purposes, the output grating coupler array in this design is sized to match

the mode field diameter of the single-mode fibers. However, the array can be readily shrunk ten-fold for better collection efficiency or to accommodate more output channels.
Finally for applications where large environmental temperature variations are present, the central wavelength of the device will shift by ≈0.125 nm/K at 2.3 µm wavelength, resulting in a small offset of the wavelength corresponding with each channel. To mitigate this, one can either use a temperature controller underneath the photonic chip, use specially designed athermal circuits [26] or use SiN waveguide circuits with a five times lower thermo-optic coefficient [27].

3.5.5 Conclusions

Low-cost and miniaturized spectrometers can be realized by combining an off-the-shelf mid-infrared photodetector with SOI wavelength demultiplexer circuits. A novel approach is shown where a single discrete photodetector is used to characterize the response of a twelve channel mid-infrared AWG at 2.3 µm. The different AWG channels are discerned by time-sequentially modulating the output arms with MZI-based thermo-optic modulators. The driving and read-out of the spectrometer is performed using low-cost standard electronic components. The absorption spectrum of PDMS is recovered at 2.3 µm to good agreement with bench-top OSA measurements. This is a promising approach which can be applied to longer wavelength SOI spectrometers for the 3-4 µm wavelength range where high-performance cooled detectors are needed.

3.6 System-on-a-package AWG spectrometer

As alluded in the previous section, further integration in the MWIR wavelength range (3-4) µm is possible by integrating the single pixel AWG spectrometer PIC as an intrinsic part of a standardized butterfly (BT) package. All photodetectors are typically sealed in a dry or vacuum atmosphere to avoid water condensation on the optical windows when cooling down the detector which would severely attenuate the optical signal. The PIC is fixed on top of a MWIR PD package and acts as part of the lid and spectrometer at the same time, see also Figure 3.11. The spectrometer output grating couplers are aligned such that the thermo-electrically cooled PD captures all the channels simultaneously. Gold alignment markers were processed on the PIC that allow automated positioning, in-line with the assembly process of the PD [28].

The detector used is a MCT photovoltaic detector with 0.8 A/W re-

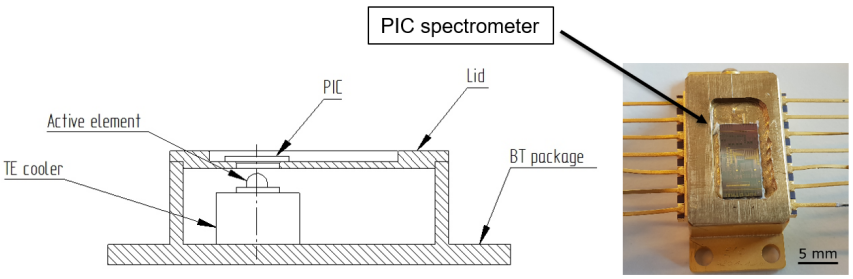

Figure 3.11: Schematic and photograph of a System-on-a-Package integration approach where the PIC spectrometer is part of the lid of the PD package. The PIC is automatically aligned and glued to the butterfly package using alignment markers on the PIC such that the output of the AWG spectrometer illuminates the cooled PD.

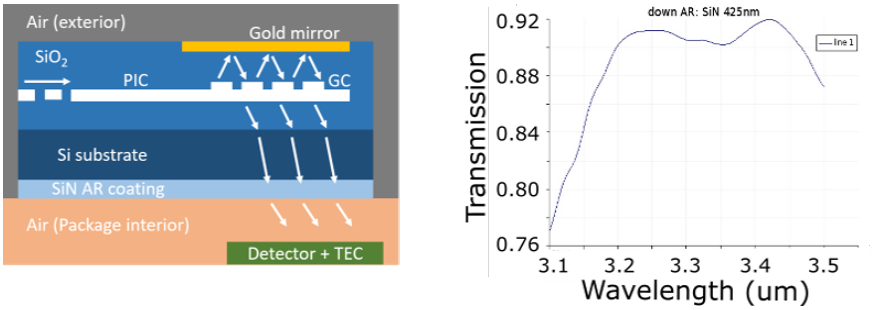

Figure 3.12: The coupling to the PD is enhanced by adding a Si_3N_4 AR coating on the backside and gold mirror on top of the PIC (a). Simulated FDTD transmission spectrum of light reaching the detector (b). The expected insertion loss is less than 10 % for a 425 nm thick Si_3N_4 film.

sponsivity at 3.3 µm from Vigo System S.A., which also carried out the packaging assembly. The coupling efficiency from the PIC to the PD can be greatly improved. A Si_3N_4 anti-reflective (AR) coating was applied to the backside of the SOI PIC. Additionally, a thin gold mirror was fabricated on top the output grating couplers to constructively enhance the light radiation towards the detector, see also Figure 3.12(a). The combined effects of the grating coupler response, AR coating and gold mirror were simulated and optimized using Lumerical 2d FDTD simulation, see also Figure 3.12(b). The PIC can be seen as an IR bandpass window for the PD with transparent response ($<$ 1 dB) in the 3.2-3.5 µm wavelength range.

The PD response is obtained by measuring the voltage provided by a TIA with 7.6 kV/A gain connected to the output of the PD. Taking the

previously measured insertion loss (IL) of the input GC into account (8dB), AWG IL of ≈ 1-2 dB and an IL ≈ 1 dB for the output grating, an overall insertion loss from the fiber to the PD of ≈ 10-11 dB is obtained. The original cross-talk of the AWG (≈ 20 dB) can be recovered by modulating each channel of interest separately, retrieving only the modulated signal on the PD. Compared to previous fiber-to-fiber (2× GC) measurements of the AWG, the insertion loss was measured to be 8 dB lower for the mounted PIC on top of the PD due to the improved coupling efficiency at the output GC.

This result demonstrates the feasibility of integrating PICs and PDs into the same package, while at the same time removing bulky parts such as IR windows and providing additional functionality to PDs. Future steps for a compact MWIR spectroscopic system are outlined in the next section with CH_4 as a possible first target gas.

3.7 Design of a dispersive CH_4 sensor

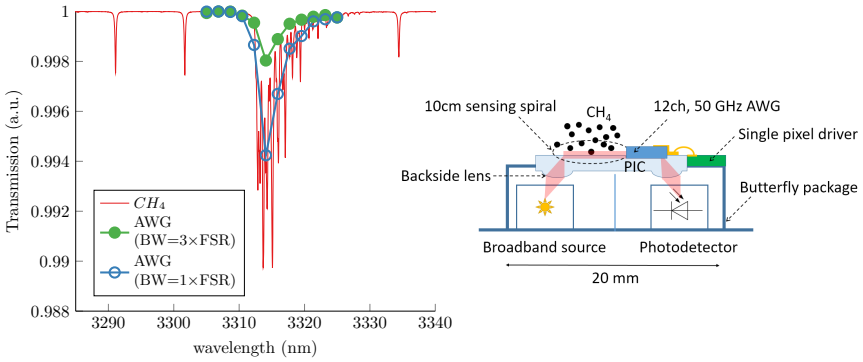

(a) (b)

Figure 3.13: Simulation of a 12 channel, single pixel 50 GHz MWIR AWG response for methane detection at 3.3 µm (a). CH_4 concentration is 100 ppm and the effective optical path length is 2.83 cm, representative of recently demonstrated SOI on-chip methane detection [29]. Even when the broadband source bandwidth is 3 ×FSR of the AWG, the methane line can still be clearly resolved. Schematic of a compact fully-integrated MWIR CH_4-spectrometer-on-a-package is shown (b). The mid-infrared broadband source, detector and spectrometer, are all contained within one butterfly (BT) package. The PIC additionally acts as a lid for the BT and integrated focusing lenses can be processed on the backside of the chip to couple the light to the PIC and back to the PD.

The approach demonstrated in the previous section can be further ex-

panded to an even more compact, fully integrated spectroscopic gas sensing system, see Figure 3.13(b). Methane leak-detection would be an important, yet challenging application that can benefit from this configuration. The absorption line of methane at 3.3 µm at atmospheric pressure conditions is broad enough to be adequately analyzed with a dispersive 50 GHz spectrometer.
Next to the PD, a broadband source such as a mid-infrared LED [30] or MEMS-based thermal emitter [31] can be incorporated into the same butterfly package, or a custom package of similar size and complexity. Additionally, in some applications such as methane, the emission spectrum of a MWIR Fabry-Perot (FP) laser can be considered 'broad' enough to cover the region of interest.
The light can be focused on the PIC grating couplers by using integrated micro-lenses, etched in the backside of the PIC [32]. The PIC can contain spiral waveguides, optimized for evanescent field sensing. For example, methane detection using 10cm long on-chip waveguide spirals, operating at 1650 nm using SOI circuits has been demonstrated [29]. The effective optical path length is on the order of centimeters. In view of the low waveguide loss of the demonstrated 400 nm SOI platform in this work at 3.3 µm, it is expected that optical interaction lengths of similar magnitude are certainly feasible at 3.3 µm. The single pixel configuration from the previous section can then be used to analyze the methane spectrum.

Figure 3.13(a) is a simulation of a 12 channel single-pixel AWG response to 100 ppm methane with a sensing spiral of 2.83 cm effective path length (confinement factor Γ=28.3 %). The channel spacing of the AWG is set to 50 GHz and previous results of measured 6 channel AWGs at 3.3 µm were used for the instrument function in the simulation, taking insertion loss and crosstalk levels into account. The calculation of the AWG was performed, assuming that the bandwidth of the source is 1×FSR (600 GHz) and 3×FSR (1800 GHz). In the latter, the transmission through the neighbouring FSR channels of the AWG will average out the methane line and reduce the signal. Still, even for a source with 70 nm BW source, the methane line can clearly be resolved.
As in the previous discussion, assuming that a transmission change of 10^{-4} can be resolved, this would indicate a sensitivity in the 5-10 ppm regime, making this system attractive for integrated point-sensing applications. The main challenges for this type of spectrometer would be the sensitivity to any contamination on the sensing spirals. Any solid organic compound would have tremendously high absorption coefficient in this wavelength range, such that dust particles can drastically reduce the optical transmission of the waveguides below the noise level of the detector. Additionally, water vapor

can condense on the surface as well and a similar effect will ensue. Possible routes to mitigate this would be to locally heat up the exposed spirals on the chip surface and to use (dust) filter enclosures around the PIC. Additionally, if on-chip sensing is not sensitive enough, the butterfly package with spectrometer can be coupled to a long multi-pass optical gas cell for increased gas interaction [33]. Such systems are for example considered for drone-based inspection and analysis of released gases in fire hazards.

3.8 Conclusions

Integration of the different components to realize a functional, compact spectroscopic system for the SWIR/MWIR is far from trivial. The development and integration of III-V laser sources and detectors on SOI PICs is advancing slowly. Passive spectroscopic components such as the AWG wavelength (de)multiplexer were demonstrated with low insertion loss, low propagation losses and low crosstalk levels in the 2-4 µm wavelength range with resolutions down to 50 GHz. This showcases that the SOI platform is well positioned for SWIR/MWIR sensing applications.

A novel AWG system architecture was demonstrated that uses a single high performance photodetector to analyze multiple spectral channels. The key principle is to apply amplitude-modulation to the AWG output waveguides, simultaneously capture the outputs on a single PD and apply Fourier analysis to retrieve the spectral content of each arm. This technique is especially attractive for MWIR applications where PD array integration is still in its infancy and cooled, expensive photodetectors are required.

A novel system-on-a-package integration strategy has been outlined that shows the benefits of integrating PICs directly onto packaged mid-infrared photodiodes/sources. For instance, the PIC can be made a part of a lid of a butterfly package, coupling a high performance SOI spectrometer directly to a PD package. This enables automatic alignment during PD assembly and improves coupling efficiency.

Further development in this direction would allow for the combination of broadband source, analyte interaction, spectrometer and PD, all in one compact package. As an example, a simulation is given for CH_4-detection using such an integration approach. The main challenges for this types of spectrometer is the sensitivity to surface contaminants such as dust and water which can essentially block the optical transmission of the waveguides in an instant. This should be investigated with care in the future, possible mitigations would envolve using heating elements and dust filters. The souce, PD and spectrometer package can also be coupled to an external, 'off-chip', long multipass gas cell for increased sensitivity.

References

[1] *AQ6376 Three Micron Optical Spectrum Analyzer 1500 - 3400 nm.* https://tmi.yokogawa.com/eu/solutions/products/optical-measuring-instruments/optical-spectrum-analyzer/aq6376-optical-spectrum-analyzer/. Accessed: 2019-12-11.

[2] Jerry Workman Jr. *The Handbook of Organic Compounds, Three-Volume Set: NIR, IR, R, and UV-Vis Spectra Featuring Polymers and Surfactants.* Elsevier, 2000.

[3] Pavel Cheben. *Wavelength dispersive planar waveguide devices: echelle and arrayed waveguide gratings.* In Optical Waveguides, pages 193–250. CRC Press, 2007.

[4] Erwin G Loewen and Evgeny Popov. *Diffraction gratings and applications.* CRC Press, 2018.

[5] Kirk G Bach and Bernhard W Bach Jr. *Large-ruled monolithic echelle gratings.* In Airborne Telescope Systems, volume 4014, pages 118–124. International Society for Optics and Photonics, 2000.

[6] Goran Z Mashanovich, Frederic Y Gardes, David J Thomson, Youfang Hu, Ke Li, Milos Nedeljkovic, Jordi Soler Penades, Ali Z Khokhar, Colin J Mitchell, Stevan Stankovic, et al. *Silicon photonic waveguides and devices for near-and mid-IR applications.* IEEE Journal of Selected Topics in Quantum Electronics, 21(4):407–418, 2014.

[7] Gunther Roelkens, Utsav D Dave, Alban Gassenq, Nannicha Hattasan, Chen Hu, Bart Kuyken, Francois Leo, Aditya Malik, Muhammad Muneeb, Eva Ryckeboer, et al. *Silicon-based photonic integration beyond the telecommunication wavelength range.* IEEE journal of selected topics in quantum electronics, 20(4):394–404, 2014.

[8] Muhammad Muneeb, Xia Chen, P Verheyen, Guy Lepage, Shibnath Pathak, Eva Ryckeboer, Aditya Malik, Bart Kuyken, Milos Nedeljkovic, Joris Van Campenhout, et al. *Demonstration of Silicon-on-insulator mid-infrared spectrometers operating at 3.8 μm.* Optics express, 21(10):11659–11669, 2013.

[9] M. Muneeb, A. Vasiliev, A. Ruocco, A. Malik, H. Chen, M. Nedeljkovic, J. S. Penades, L. Cerutti, J. B. Rodriguez, G. Z. Mashanovich, M. K. Smit, E. Tourni, and G. Roelkens. *III-V-on-silicon integrated micro - spectrometer for the 3 μm wavelength range.* Opt. Express, 24(9):9465–9472, May 2016.

[10] Ruijun Wang, Anton Vasiliev, Muhammad Muneeb, Aditya Malik, Stephan Sprengel, Gerhard Boehm, Markus-Christian Amann, Ieva Šimonytė, Augustinas Vizbaras, Kristijonas Vizbaras, et al. *III–V-on-silicon photonic integrated circuits for spectroscopic sensing in the 2–4 μm wavelength range.* Sensors, 17(8):1788, 2017.

[11] Eva Ryckeboer, Alban Gassenq, Muhammad Muneeb, Nannicha Hattasan, Shibnath Pathak, Laurent Cerutti, Jean-Baptiste Rodriguez, E Tournié, Wim Bogaerts, Roel Baets, et al. *Silicon-on-insulator spectrometers with integrated GaInAsSb photodiodes for wide-band spectroscopy from 1510 to 2300 nm.* Optics express, 21(5):6101–6108, 2013.

[12] Laurent Bizet, Raphael Vallon, Bertrand Parvitte, Mickael Brun, Gregory Maisons, Mathieu Carras, and Virginie Zeninari. *Multi-gas sensing with quantum cascade laser array in the mid-infrared region.* Applied Physics B, 123(5):145, 2017.

[13] Meint K Smit and Cor Van Dam. *PHASAR-based WDM-devices: Principles, design and applications.* IEEE Journal of selected topics in quantum electronics, 2(2):236–250, 1996.

[14] Ruijun Wang, Muhammad Muneeb, Stephan Sprengel, Gerhard Boehm, Aditya Malik, Roel Baets, Markus-Christian Amann, and Gunther Roelkens. *III-V-on-silicon 2-μm-wavelength-range wavelength demultiplexers with heterogeneously integrated InP-based type-II photodetectors.* Opt. Express, 24(8):8480–8490, 2016.

[15] Muhammad Muneeb, Anton Vasiliev, Alfonso Ruocco, Aditya Malik, Hongtao Chen, M Nedeljkovic, J Soler Penades, L Cerutti, Jean-Baptiste Rodriguez, GZ Mashanovich, et al. *III-V-on-silicon integrated micro-spectrometer for the 3 μm wavelength range.* Optics express, 24(9):9465–9472, 2016.

[16] Anton Vasiliev, Muhammad Muneeb, Alfonso Ruocco, Aditya Malik, Hongtao Chen, Milos Nedeljkovic, Jordi Soler-Penades, Laurent Cerutti, Jean-Baptiste Rodriguez, Goran Mashanovich, et al. *3.8 um heterogeneously integrated III-V on silicon micro-spectrometer.* In 18th European Conference in Integrated Optics 2016, 2016.

[17] Thorlabs. *MIR Single Mode Fluoride Fiber Optic Patch Cables*, 2016.

[18] Alexander M. Morrison, Tao Liang, and Gary E. Douberly. *Automation of an Aculight continuous-wave optical parametric oscillator.* Rev. Sci. Instrum., 84(1):013102:1–013102:8, 2013.

[19] Ruijun Wang, Stephan Sprengel, Gerhard Boehm, Roel Baets, Markus-Christian Amann, and Gunther Roelkens. *Broad wavelength coverage 2.3 μm III-V-on-silicon DFB laser array.* Optica, 4(8):972–975, 2017.

[20] Benjamin G Lee, Mikhail A Belkin, Christian Pflugl, Laurent Diehl, Haifei A Zhang, Ross M Audet, Jim MacArthur, David P Bour, Scott W Corzine, Gloria E Hofler, et al. *DFB quantum cascade laser arrays.* IEEE Journal of Quantum Electronics, 45(5):554–565, 2009.

[21] S Nicoletti et al. *Challenges in the realization of a fully integrated optical lab-on-chip.* In IEEE Sensors, pages 649–652. IEEE, Nov 2014.

[22] Eric J Stanton, Alexander Spott, Jon Peters, Michael L Davenport, Aditya Malik, Nicolas Volet, Junqian Liu, Charles D Merritt, Igor Vurgaftman, Chul Soo Kim, et al. *Multi-spectral quantum cascade lasers on silicon with integrated multiplexers.* In Photonics, volume 6, page 6. Multidisciplinary Digital Publishing Institute, 2019.

[23] Roeland Baets, Danaë Delbeke, Günther Roelkens, and Wim Bogaerts. *Integrated spectrometers with single pixel detector*, July 31 2018. US Patent App. 10/036,625.

[24] Anton Vasiliev, Muhammad Muneeb, Jeroen Allaert, Joris Van Campenhout, Roel Baets, and Günther Roelkens. *Integrated silicon-on-insulator spectrometer with single pixel readout for mid-infrared spectroscopy.* IEEE Journal of Selected Topics in Quantum Electronics, 24(6):1–7, 2018.

[25] J Piotrowski, W Galus, and M Grudzien. *Near room-temperature IR photo-detectors.* Infrared Phys., 31(1):1–48, 1991.

[26] Linghua Wang et al. *Athermal arrayed waveguide gratings in silicon-on-insulator by overlaying a polymer cladding on narrowed arrayed waveguides.* Appl. Opt., 51(9):1251–1256, 2012.

[27] Michael Belt, Jock Bovington, Renan Moreira, Jared F Bauters, Martijn JR Heck, Jonathon S Barton, John E Bowers, and Daniel J Blumenthal. *Sidewall gratings in ultra-low-loss Si 3 N 4 planar waveguides.* Optics express, 21(1):1181–1188, 2013.

[28] Anton Vasiliev, Fabio Pavanello, Muhammad Muneeb, J Jurenczyk, A Jurenczyk, M Liebert, and Günther Roelkens. *Novel approach for the integration of photonic circuits with mid-IR detectors.* In 44th Freiburg Infrared Colloquium, pages 1–1, 2019.

[29] Lionel Tombez, EJ Zhang, JS Orcutt, Swetha Kamlapurkar, and WMJ Green. *Methane absorption spectroscopy on a silicon photonic chip.* Optica, 4(11):1322–1325, 2017.

[30] L Scholz, A Ortiz Perez, S Knobelspies, J Wöllenstein, and S Palzer. *MID-IR LED-based, Photoacoustic CO2 Sensor.* Procedia engineering, 120:1233–1236, 2015.

[31] Alexander Lochbaum, Yuriy Fedoryshyn, Alexander Dorodnyy, Ueli Koch, Christian Hafner, and Juerg Leuthold. *On-chip narrowband thermal emitter for mid-IR optical gas sensing.* ACS photonics, 4(6):1371–1380, 2017.

[32] Jeroen Missinne, N Teigell Benéitez, Nivesh Mangal, Jing Zhang, Anton Vasiliev, Joris Van Campenhout, Bradley Snyder, Günther Roelkens, and Geert Van Steenberge. *Alignment-tolerant interfacing of a photonic integrated circuit using back side etched silicon microlenses.* In Silicon Photonics XIV, volume 10923, page 1092304. International Society for Optics and Photonics, 2019.

[33] Kun Liu, Lei Wang, Tu Tan, Guishi Wang, Weijun Zhang, Weidong Chen, and Xiaoming Gao. *Highly sensitive detection of methane by near-infrared laser absorption spectroscopy using a compact dense-pattern multipass cell.* Sensors and Actuators B: Chemical, 220:1000–1005, 2015.

4

Digital FTIR spectrometer for wavelength monitoring

Fully *integrated devices based on laser sources can greatly benefit from on-chip laser wavelength calibration. In this chapter, a digital Fourier Transform InfraRed (FTIR) architecture is demonstrated for a silicon photonic chip in the 2.3* µm *wavelength range. Sparse regularization methods are used to extend the operation bandwidth of the fabricated device.*

Contents

4.1 Introduction

Integrated dispersive AWG and ECG elements from the previous chapter are widely used to build robust spectrometers [1–3]. However, if a large bandwidth and high resolution are required, these elements can require quite

a large footprint on the PIC. A different popular Fourier Transform-based approach is called spatial heterodyne spectroscopy (SHS) where the operation principle is similar to an FTIR without moving parts [4–7]. The core element of this method is an array of Mach-Zehnder Interferometers (MZI) which have a cosine-shaped spectral transmission $T(\lambda)$ depending on the optical path delay between the interferometer arms ΔL.

$$T(\lambda, \Delta L) \sim \cos^2\left(\frac{\pi}{\lambda} n_{eff} \Delta L\right) \tag{4.1}$$

with n_{eff} the effective index of the waveguide mode and no losses are included. The photodiode response $y(\Delta L)$ is found by integrating $T(\lambda)$ over all wavelengths. The cosine frequency is an increasing function of the OPD ΔL between the two arms. For an unknown input spectrum $x(\lambda)$, the photodiode response for a multitude of different OPDs is collected, forming an interferogram. This is similar to the working principle of a FTIR but with (fewer) discrete number of OPDs. The cosine Fourier transform of the interferogram will then, in theory, yield the unknown input spectrum. In practice however, the fabricated SHS device features imperfections such as loss, phase errors and dispersion effects which prohibit the direct use of the simple cosine Fourier transform to recover the spectrum. Instead, compensation methodologies can be applied to calibrate out the discrepancies and apply the transform. A more elegant approach is to acknowledge that the MZI array circuit represents a general **linear**[1] transformation. Therefore a simple relationship holds between the interferogram output intensity $y(\Delta L)$ and the unknown input spectrum $x(\lambda)$

$$y(\Delta L) = A(\Delta L, \lambda) x(\lambda) \tag{4.2}$$

where in the idealized SHS case, the calibration matrix A will contain the cosine spectral responses in the columns. In practice, it is possible to measure the matrix A and invert the relation to obtain x. However, this is often an ill-posed problem and regularization methods are needed to properly invert the equation.

For example, this SHS FT approach based on an array of separate MZIs with linearly increasing optical path delays (OPDs) was demonstrated [6]. The footprint of this device scales linearly with the number of channels as well as the number of output ports. Compressive sensing algorithms can reduce the number of required MZIs to achieve a given resolution, however the scaling behavior remains still linear. To address this linear scaling behaviour, a new approach named digital FTIR (dFTIR) spectrometer was proposed by [8]. The concept is schematically represented in Figure 4.1.

[1] unitary in the general case

The difference to the previous SHS device is that in the dFTIR architecture, the number of physical delay spirals is exponentially reduced. The key principle is that the effective OPD of the device is controlled by directing the light through different optical switch combinations re-using a fixed set of delay arms. This yields a reduction in overall size of the device at the expense of total measurement time needed to perform the optical switching operation. In fact, the number of channels scales exponentially (base 2) with the the number of switch-elements providing the effective OPD [8].

Diving into more detail, this approach is based on a cascade of unbalanced MZIs where each of the stages comprises a switch. Depending on the specific configuration of each switch, OPDs between the top and the bottom arms of the dFT spectrometer can be modified in a reconfigurable manner. In fact, if the stages are switched purely in a binary way i.e. light is sent only in one of the two arms of each MZI stage, then $N = 2^j$ configurations are possible where j represents the number of switches. The expected resolution according to the Rayleigh criterion is then [9]

$$\delta\lambda \approx \frac{1}{2^N} \frac{\lambda^2}{n_g \Delta L} \tag{4.3}$$

with n_g the group index, ΔL the incremental OPD and λ the central wavelength. This exponential scaling property paves the way to potentially build very compact spectrometers which can provide, with a limited number of stages and footprint, sub-nm spectral resolution according to the Rayleigh criterion [10, 11].

The dFTIR approach has been recently experimentally demonstrated near 1550 nm wavelength on an SOI platform over a bandwidth of 20 nm [8, 9]. For an arbitrary input spectrum, machine learning and regularization methods were required to ensure a reasonable spectral reconstruction. In this work, the goal is to investigate the dFTIR spectrometer approach for wavelength tracking in the 2.3 µm wavelength range for applications such as Vernier-based widely tunable lasers stabilization, which require wavelength monitoring as a feedback mechanism [12, 13]. Furthermore, this approach allows for the monitoring of multiple closely (sub-nm) spaced laser lines or 'mode-hopping' of a laser mode at the same time. There are other approaches for integrated wavelength monitoring, however they are generally characterized by a reduced bandwidth, large footprint, limited resolution or use multiple photodetectors [13–17]. Besides, they are only suitable to monitor only a single line.

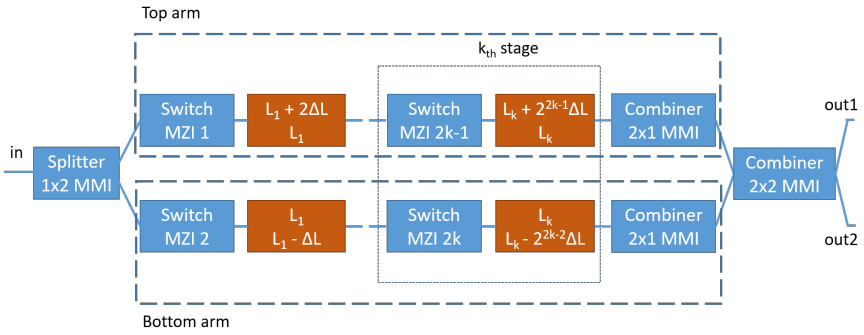

Figure 4.1: The dFTIR spectrometer is a reconfigurable MZI circuit, consisting of k switches in the 'top' and 'bottom' arm in such a way that each combination results in a unique optical path difference between the two main arms. This MZI re-uses a fixed set of delay paths to exponentially decrease the total number of delay spirals on the chip. In this way, the effective OPD is exponentially (base 2) distributed over $N = 2^{2k}$ values. Every stage has a top and a bottom arm with same lengths. $k = 1, 2, 3$ with $L_k = L_1 + 2^{2k-2}\Delta L$.

4.2 Operation principle and design

The working principle of the dFTIR spectrometer approach (see Fig. 4.1) consists of acquiring the stationary interferogram for N different OPDs of the reconfigurable MZI from which the input can be reconstructed using FT-based methods [4]. Delay lines in the lower arm allow a negative (with respect to the common arm of length L_k in every stage) delay of $-2^{2k-2}\Delta L$, while those in the upper arm allow a positive (with respect to the common arm length L_k) delay of $2^{2k-1}\Delta L$, where ΔL is obtained from Eq. 4.3. Here, L_k is equal to $L_1 + 2^{2k-2}\Delta L$ with L_1 a constant offset. A calibration step is performed which measures the exact wavelength response for each state of the reconfigurable spectrometer. The NxM calibration matrix A represents the system response for $N = 2^j$ configurations of switches (all the binary combinations available) at M wavelength points. In this work j is 6 as we used 3 stages allowing $N = 64$ binary configurations. Several techniques can be adopted to retrieve the spectral response depending on the characteristics of the input signal. In this work only wavelength monitoring applications are targeted and therefore it is assumed that $x(\lambda)$ is a sparse vector. The unknown spectrum is computed using two methods: the first one involves the calculation of the Moore-Penrose least-squares (LSQR) inverse of A and the second one takes the sparsity into account by solving the convex optimization problem using the least absolute shrinkage and

selection operator (LASSO) [6, 9]:

$$\min_{x_1,..,x_M \geq 0} \quad ||Ax - y||_2 \qquad \text{subject to} \qquad ||x||_1 \leq \tau \tag{4.4}$$

with τ a pre-specified parameter which scales with the sparseness of the solution. For $\tau \to \infty$, the LSQR solution is found. The problem is solved efficiently using the non-negative spectral projected-gradient algorithm (SPGL) in Python [18, 19]. The design layout of the dFTIR is shown

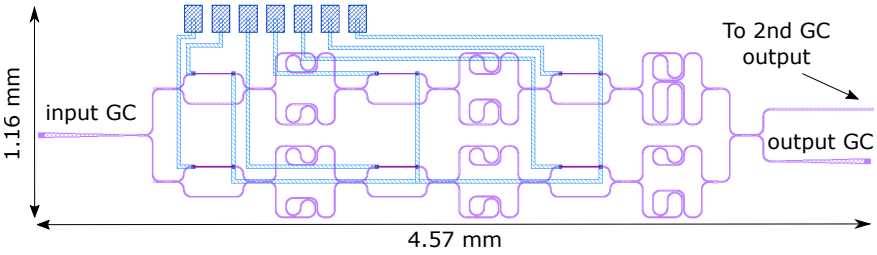

Figure 4.2: Layout of the 3-stage dFTIR spectrometer. A complementary port, 1.45 mm away for the output grating, is not reported for drawing clarity.

in Figure 4.2. A 400 nm thick silicon device layer and 3 µm thick buried oxide (BOX) layer have been used. A single-mode 800 nm wide rib waveguide, defined with a 180 nm deep etch depth, has been used for the MZIs and the routing, while the bending radius was 40 µm. The grating couplers are designed for 2.28 µm wavelength using a single partial etch step. The minimum optical path length difference ΔL was 10.825 µm and it was set by using eq. 4.3 with a group index $n_g = 3.75$ and a spectral channel bandwidth $\delta\lambda = 2$ nm. The constant offset $L_1 = 770$ µm in each spiral corresponds to the minimum dimension in correspondence with the designed inter-spiral spacing and bending radius. Grating couplers are used for input/output coupling. DC pads 150 µm x 100 µm wide are used to drive the thermo-optic switches. The idealized optical transmission of the MZI is shown in Figure 4.3 along with the ideal calibration matrix in the lossless and dispersion-free case. At the Littrow wavelengths, the optical phase delay at each MZI is an integer multiple of 2π and the transmission is equal to unity for all configurations, provided that all delays are an integer multiple of ΔL_0.

4.3 Fabrication

For fast prototyping purposes, the patterning of the 400 nm thick device layer has been performed with e-beam lithography [12]. However, all the

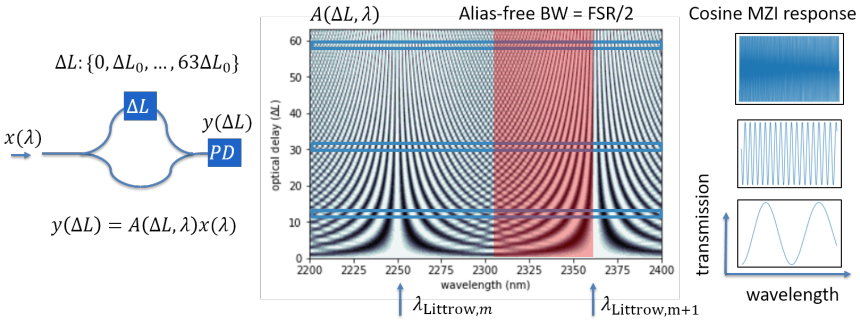

Figure 4.3: Schematic and ideal transmission simulation of an integrated SWIR MZI with 64 discrete optical delays ΔL with the same design parameters as for the fabricated device. The different delays produce an interferogram signal at the PD $y(\Delta L)$ for an unknown input spectrum $x(\lambda)$. The expected cosine response matrix $A(\Delta L, \lambda)$ of a lossless and dispersion-free dFTIR device is given, indicating the alias-free bandwidth and Littrow wavelengths.

minimum feature size dimensions can be achieved using industry-standard silicon fabrication tools. A 180 nm deep etching has been carried out using reactive ion etching to define rib waveguides. The layout has been matched to a 500 x 500 µm^2 grid in order to minimize stitching issues due to adjacent patterning fields. These issues would impact the insertion loss of the device and have been minimized by placing grid lines onto MMIs central multimode sections or onto 2 µm wide waveguides (with respective tapers) in other critical locations to increase the device tolerance and to reduce the insertion loss. Afterwards, a 1.5 µm thick SiO_2 layer has been deposited to enable heater integration. Heaters are based on a 150/10 nm thick Ti/Au bi-layer. Au wires and pads are then fabricated by UV lithography. The device is finally passivated with 700 nm thick BCB layer with openings on pads and grating couplers for probing. The overall footprint (complementary output excluded) is 4.57 mm x 1.16 mm. Heaters are placed on one arm and 2x2 MMIs are used at the input/output of the switches. A straight 2 µm wide waveguide with input/output grating couplers has been added to estimate the on-chip insertion loss.

4.4 Measurements and analysis

The measurements were performed using a Yokogawa AQ6375 OSA and the IPG photonics SFTL-Cr-ZnS/Se laser [12]. A 26 pin DC probe from GGB industries has been used to drive the heaters through an in-house designed 64 channel power supply, same one as the one used for the single

pixel experiment. The required P_π power for the heaters is estimated at

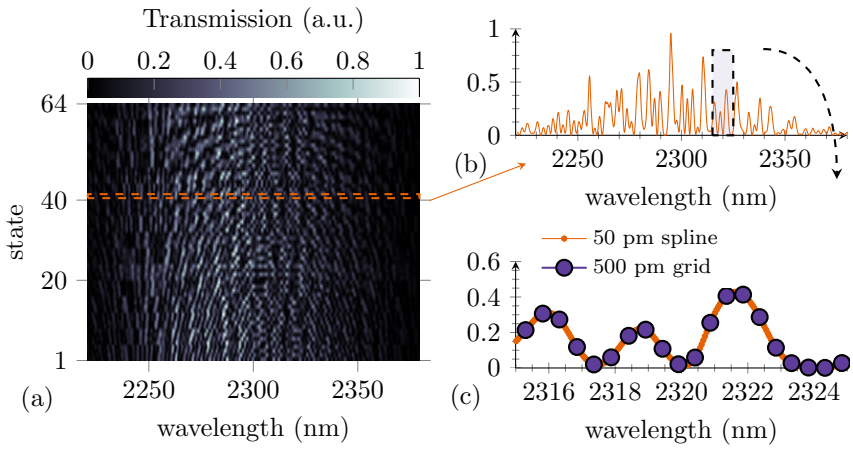

Figure 4.4: Normalized calibration matrix for all 64 switch combinations (a). The broad wavelength dependency is due to the grating coupler bandwidth. The data is collected over the course of a few hours and without temperature control of the chip. An example for the switch state combination corresponding to 411 µm *OPD is shown (b). The calibration data is collected on a 500 pm wavelength step grid and interpolated using a spline function to a 50 pm regular grid (c).*

52 mW and was obtained from measuring an isolated 2x2 reference MZI with an extinction ratio larger than 30 dB. It is worth mentioning that the actual switching power for each stage is slightly different because of different heater resistances. However, such a difference does not impact the correct operation of the system as observed in our measurements. The on-chip insertion loss measured at the maximum transmission envelope for all the combinations was between 7 and 8 dB over a 130 nm wavelength span.

The calibration matrix A was collected on a wavelength grid spanning 160 nm with 0.5 nm steps, see also the normalized transmission in Figure 4.4(a). An example of a spectrum for a given state is provided in Figure 4.4(b). The collection was performed once at ambient room temperature over the course of few hours. The switching stages are not monitored and the splitting power ratio varies among the switches decreasing the visibility of the interferometric fringes. Nonetheless, the linear system is proven to be remarkably robust against these issues. However, in this case it is not possible to observe a clean single frequency sinusoid for any given state.

It was found that the accuracy of the spectral recovery can be further increased from 500 pm to 100 pm by interpolating the calibration matrix data points onto a finer 50 pm grid using a spline function, see also Figure 4.4(c). In what follows, a 64 x 3200 calibration matrix is therefore employed,

spanning 160 nm with 50 pm wavelength grid spacing.

For wavelength tracking applications where the spectrum is sparse and the laser operation is in a single longitudinal mode, it is sufficient to record only the peak wavelength of the reconstructed spectrum. To this end, the LSQR solution already provides a reasonable estimate. Two examples of spectral retrieval obtained from $N = 64$ consecutive optical power measurements are shown in Figure 4.5. The LSQR solution has clearly more artifacts in the retrieved spectrum than LASSO, however the peak wavelength is close to the actual wavelength for both methods when limited to the operational bandwidth of 130 nm. When the input spectrum is located near the edge as in Figure 4.5(b), aliasing is introduced, leading to erroneous wavelength readings. To estimate the accuracy of the device, 40 random wavelengths were selected for the laser input, spanning from 2220 nm to 2380 nm. A single interferogram was collected in each case and the calibration matrix was used to compute the LSQR and LASSO solutions. The global maximum of the normalized solution is then compared to the reading of the OSA, see Figure 4.6(a). The parameter τ controls the maximum allowed L_1-norm of the reconstructed spectrum and influences the spectral ripples of the reconstructed spectrum. It was found empirically that $\tau = 3.8$ was optimal to simultaneously track a single laser line and to resolve two lines for all conducted measurements. Alternatively, machine learning techniques could be used to search for the optimal parameter for each measurement separately without a priori knowledge of the examined spectrum at the cost of computational time [9]. The aliasing-free region for LASSO solutions is 130 nm and the wavelength accuracy of the method is about 100 pm. The zero-offset in Figure 4.6(b) is due to the fact that the calibration was performed at different ambient temperature from the actual interferogram measurements. The temperature dependence of the spectrometer was measured to be 110 pm/^{o}C.

It is believed that further improvement in accuracy can be readily achieved with active temperature stabilization of the chip and by fixing the optical input / output. The latter is obviously self-fulfilled for the case of a wavelength monitor for an integrated laser fabricated on the same chip. Besides, by using athermal MZIs configurations, the required power for active stabilization (if still necessary) can be further reduced.

To assess the wavelength tracking of a fine wavelength sweep of a laser, the emission wavelength of an OPO source was tuned piezo-electrically to successfully track the wavelength over a 600 pm window with the same 100 pm accuracy, see also Figure 4.6(c). It is worth noting that without interpolation of the calibration matrix, the accuracy goes back to 500 pm (the measurement grid).

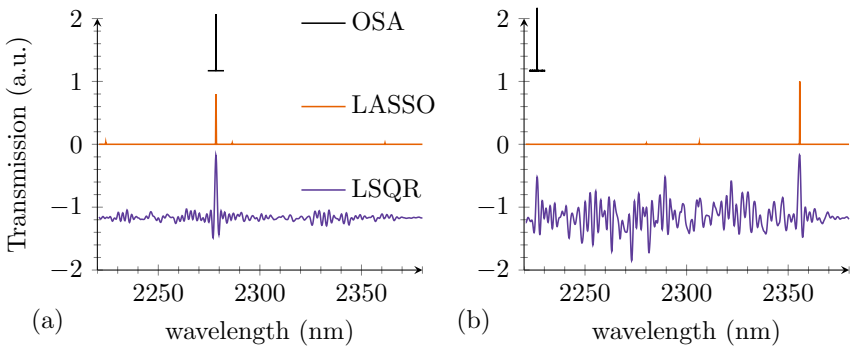

Figure 4.5: Reconstructed spectra for an unknown laser input in the calibration span. The global maximum is used to assert the unknown laser wavelength. (a) Both LSQR and LASSO can recover the peak wavelength accurately within the operating bandwidth (FSR). (b) Aliasing occurs when the laser wavelength is outside of the FSR. The normalized spectra are shifted vertically for clarity.

To estimate the resolution of the spectrometer, the Cr-ZnS/Se solid state laser was multiplexed with a custom GaSb-based external cavity laser from Brolis Semiconductors and tuned to a predefined line separation, see Figure 4.7. Clearly, the LASSO solution is superior to the LSQR solution for evaluating sparse multimode spectra. The spectrometer can resolve multiple laser lines with a separation down to 1.5 nm in a single iteration and down to 0.5 nm in a two step algorithm. In the second step, the reconstruction algorithm is limited to a bandwidth window of 20 nm centered at the peak wavelength determined in the first step. This presents opportunities for the monitoring of mode-hopping phenomenon in laser systems, given that the dFTIR can be swept on a sufficiently fast timescale. For this purpose, fast electro-optic Mach-Zehnder modulators and fast PDs can be potentially used.

In the context of single mode wavelength monitoring, the presented dFT spectrometer can be made more efficient by leaving out a number of used OPD states. In this way, it is possible to reduce the required measurement time (dissipated power), computational resources and footprint without suffering any penalty on the accuracy. Due to the compressive sensing nature of LASSO, about 12 random states (12 rows, roughly 20% of all the states) can be omitted from the calibration matrix A, whilst retaining the same accuracy as shown in Figure 4.6(d). The root-mean square error (RMSE) on the recovered wavelength is calculated for different total number of states (randomly selected) of the matrix A.

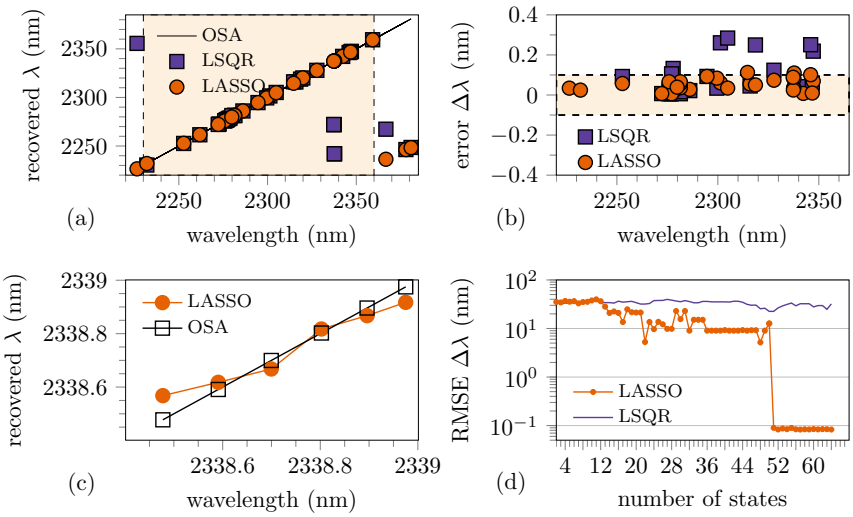

Figure 4.6: Spectrometer performance in terms of tracking accuracy. (a) The wavelength is recovered without aliasing over a bandwidth of 130 nm. (b) The LSQR algorithm produces outliers more frequently than LASSO. The accuracy is within 100 pm for 40 measurements within the bandwidth. The sparseness parameter is set to $\tau = 3.8$ for all measurements. The average error is not zero as the measurements were performed at a different ambient temperature with respect to the calibration. (c) Wavelength tracking of OPO laser module for a fine-tuning of the wavelength. The spectrometer can follow a 100 pm step sweep of the wavelength (calibration on a 500 pm grid). (d) The RMSE is calculated for all the measurements (40) within a 130 nm bandwidth. The compressive sensing (LASSO) algorithm makes it possible to reach optimal accuracy even when less than 64 states are used for the reconstruction, i.e. certain states are omitted randomly. The LSQR algorithm is less reliable due to a higher outlier count.

4.5 Conclusion

In conclusion, a mid-infrared dFTIR spectrometer was demonstrated for wavelength monitoring applications around 2.3 µm with a broad bandwidth of 130 nm. Although the spectrometer is fabricated with e-beam lithography, the same design can be readily used with deep-UV lithography, therefore supporting its CMOS-compatibility. The results demonstrate its potential to retrieve a given laser line with an accuracy of 100 pm. The low insertion loss and the large scalability showcase its potential as a wavelength monitor for mid-infrared applications spanning hundreds of nanometers.

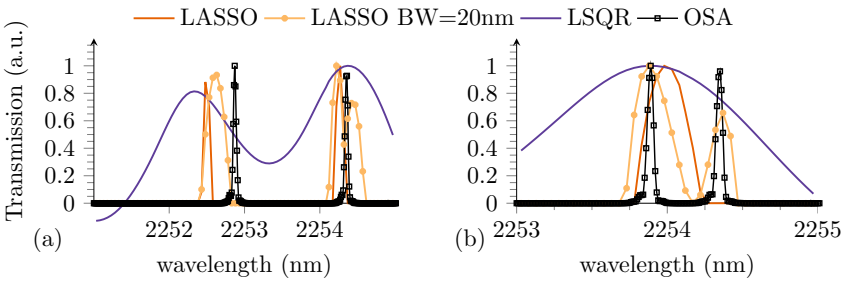

Figure 4.7: The spectrometer can resolve multiple laser lines with a separation down to 1.5 nm in one iteration (a) and down to 0.5 nm in two steps (b). In the second step, the reconstruction algorithm is limited to a bandwidth window of 20 nm centered at the peak wavelength determined in the first step.

References

[1] Aditya Malik, Muhammad Muneeb, Yosuke Shimura, Joris Van Campenhout, Roger Loo, and Gunther Roelkens. *Germanium-on-silicon planar concave grating wavelength (de)multiplexers in the mid-infrared.* Applied Physics Letters, 103(16):161119, 2013.

[2] Pierre Barritault, Mickael Brun, Pierre Labeye, Jean-Michel Hartmann, Fahem Boulila, Mathieu Carras, and Sergio Nicoletti. *Design, fabrication and characterization of an AWG at 4.5 m.* Optics Express, 23(20):26168, oct 2015.

[3] Anton Vasiliev, Muhammad Muneeb, Jeroen Allaert, Joris Van Campenhout, Roel Baets, and Gunther Roelkens. *Integrated Silicon-on-Insulator Spectrometer with Single Pixel Readout for Mid-Infrared Spectroscopy.* IEEE Journal of Selected Topics in Quantum Electronics, 24(6):8300207, 2018.

[4] Miroslaw Florjanczyk, Pavel Cheben, Siegfried Janz, Alan Scott, Brian Solheim, and Dan-Xia Xu. *Multiaperture planar waveguide spectrometer formed by arrayed Mach-Zehnder interferometers.* Optics Express, 15(26):18176, dec 2007.

[5] Milos Nedeljkovic, Aitor V. Velasco, Ali Z. Khokhar, Andre Delage, Pavel Cheben, and Goran Z. Mashanovich. *Mid-Infrared Silicon-on-Insulator Fourier-Transform Spectrometer Chip.* IEEE Photonics Technology Letters, 28(4):528–531, feb 2016.

[6] Hugh Podmore, Alan Scott, Pavel Cheben, Aitor V. Velasco, Jens H. Schmid, Martin Vachon, and Regina Lee. *Demonstration of a compressive-sensing Fourier-transform on-chip spectrometer.* Optics Letters, 42(7):1440–1443, 2017.

[7] Riki Uda, Kohei Yamaguchi, Kazumasa Takada, and Katsunari Okamoto. *Fabrication of a silica-based complex Fourier- transform integrated-optic spatial heterodyne spectrometer incorporating 120 optical hybrid couplers.* Applied Optics, 57(14):3781–3787, may 2018.

[8] Derek M. Kita, Hongtao Lin, Anu Agarwal, Kathleen Richardson, Igor Luzinov, Tian Gu, and Juejun Hu. *On-Chip Infrared Spectroscopic Sensing: Redefining the Benefits of Scaling.* IEEE Journal of Selected Topics in Quantum Electronics, 23(2), 2017.

[9] Derek M Kita, Brando Miranda, David Favela, David Bono, Jérôme Michon, Hongtao Lin, Tian Gu, and Juejun Hu. *High-performance*

and scalable on-chip digital Fourier transform spectroscopy. Nature Communications, 9(4405):1–7, 2018.

[10] Hongtao Lin, Zhengqian Luo, Tian Gu, Lionel C Kimerling, Kazumi Wada, Anu Agarwal, and Juejun Hu. *Mid-infrared integrated photonics on silicon: A perspective.* Nanophotonics, 7(2):393–420, 2017.

[11] Brian Smith. *Fundamentals of Fourier transform infrared spectroscopy.* CRC Press, mar 2011.

[12] Fabio Pavanello, Anton Vasiliev, Muhammad Muneeb, and Günther Roelkens. *Broadband Digital Fourier Transform Spectrometer for On-Chip Wavelength Monitoring in the 2.3-μm Wavelength Range.* IEEE Photonics Journal, 11(3):1–9, 2019.

[13] M. Muneeb, A. Ruocco, A. Malik, S. Pathak, E. Ryckeboer, D. Sanchez, L. Cerutti, J.B. Rodriguez, E. Tournié, W. Bogaerts, M.K. Smit, and G. Roelkens. *Silicon-on-insulator shortwave infrared wavelength meter with integrated photodiodes for on-chip laser monitoring.* Optics Express, 22(22):27300, 2014.

[14] W. H. Chung, H. Y. Tam, M. S. Demokan, P. K.A. Wai, and C Lu. *Wavelength and power monitoring of DWDM systems using scanning F-P filter calibrated with a F-P laser.* Optics Communications, 210(3-6):219–224, 2002.

[15] Domenico D'Agostino, Thibault Desbordes, Ronald Broeke, Martijn Boerkamp, Jan Mink, Huub Ambrosius, and Meint Smit. *A monolithically integrated AWG based wavelength interrogator with 180 nm working range and pm resolution.* In Advanced Photonics for Communications, page IM2A.4, Washington, D.C., jul 2014. OSA.

[16] D. D'Agostino, R Broeke, M Boerkamp, J Mink, H.P.M.M. Ambrosius, and M.K. Smit. *AWG based wavelength-meter with pm resolution.* In Proceedings of the 17th European Conference on Integrated Optics and Technical Exhibitionan, 19th Microoptics Conference(ECIO-MOC), volume 2, pages 3–4, 2014.

[17] Céline Duchemin, Fabrice Thomas, Bruno Martin, Eric Morino, Renaud Puget, Robin Oliveres, Christophe Bonneville, Thierry Gonthiez, and Nicolas Valognes. *Development of an integrated sub-picometric SWIFTS-based wavelength meter.* In Yakov G. Soskind and Craig Olson, editors, SPIE proceedings, Photonic Instrumentation Engineering IV, volume 10110, page 1011016. International Society for Optics and Photonics, feb 2017.

[18] Ewout Van Den Berg and Michael P. Friedlander. *Spgl1: A solver for large-scale sparse reconstruction.* http://www.cs.ubc.ca/labs/scl/spgl1.

[19] Ewout Van Den Berg and Michael P. Friedlander. *Sparse Optimization with Least-Squares Constraints.* SIAM Journal on Optimization, 21(4):1201–1229, oct 2011.

5

PhotoThermal Spectroscopy

The goal of this chapter is to elucidate a compact, contactless photothermal spectroscopy sensor on an integrated platform that can potentially reach sub-ppm sensitivities for gas detection. The different factors affecting the limit of detection will be discussed together with proof-of-concept experimental results.

Contents

5.1 Introduction: photothermal effect

Photothermal spectroscopy (PTS) is an agglomeration of several highly sensitive measurement methods that probe the optical absorption spectrum through its thermal response. The analyte is illuminated and the absorbed light energy leads to sample heating. This energy transfer due to optical absorption can be probed by measuring the photo-induced temperature-, pressure- or density change of the sample through various means. For instance, when the density of the medium is increased, light propagates slower through the analyte which is described by an increase in the refractive index. This thermo-optic effect is quite common and is not only observed on microscopic level. In fact, on a hot sunny day, it is quite common to observe the so-called mirage effect, see also Figure 5.1. Sunlight is absorbed on the road and this results in surface heating which in turn heats up the air right above it. The density of the air above the surface becomes lower than the ambient air which results in a refractive index gradient increasing upwards from the road surface. A person observing the surface at an acute tangent angle does not see the road but rather light rays refracted from the sky above the surface.

The photoacoustic effect is observed when the photo-induced tempera-

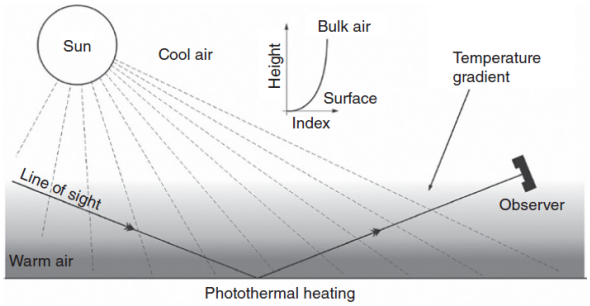

Figure 5.1: Example of common photothermal effect, mirage effect on a hot sunny road. A person observing the surface at an acute tangent angle does not see the road but rather light rays refracted from the sky above the surface. The road is heated photothermally, which increases the air's temperature above the road causing a refractive index gradient. [1]

ture change occurs faster than the relaxation time needed for the medium to expand or contract. In this case, a pressure change or acoustic wave is observed which can be detected with a microphone. In fact, Bell has used this photoacoustic effect in 1880 [2] to construct a photophone. Audible sound can be generated from a container filled with optically absorbing ma-

terial (e.g. gas). Modulation of the light impinging on an absorbing gas, constrained to a certain volume, will produce acoustic waves or pressure modulation through the photothermal effect.

These two examples play a pivotal role in the current academic frontier on miniaturized photothermal sensors. For photothermal systems measuring the refractive index, both fiber- and etalon-based interferometers have been shown with great performance and high dynamic range for trace gas sensing [3, 4]. For photoacoustic systems, the main research focus is now geared either towards augmenting the read-out signal with an ultra-sensitive optical cantilever pressure sensor or through the use of a quartz tuning fork with piezo-electric readout (QEPAS) [5, 6]. Limit of Detection (LOD) values of parts-per-trillion (ppt) have been demonstrated [5, 7]. These methods demonstrate a highly sensitive and promising sensor approach. However, many challenges remain for large scale integration. One inherent drawback of photoacoustic methods is that the signal can experience (de)amplification depending on the composition of the gas matrix surrounding the analyte and on the exact gas species under test. For example, the presence of water vapor in air affects the relaxation dynamics of methane trace gas. Dual laser wavelength calibration methods are needed to decouple the influence of water on the retrieved methane signal, providing accurate concentration results [6]. Note that this signal interference or cross-talk can occur even if the excitation wavelength tuned to the absorption line of the analyte (methane) is optically transparent to the gas matrix (water vapor).

Secondary challenges for further miniaturization are of engineering nature. Cantilever-based methods require a carefully designed buffer volume to reduce air flow noise and influence from external acoustic sources [8, 9]. Integrated quartz 'tuning fork'-like methods need to be carefully designed such that the excitation beam does not illuminate the tuning fork arms. Unwanted photothermal heating of the arms leads to a non-negligible background signal. This implies that fully integrated system require a precise and preferably pre-aligned method to deliver the excitation pump beam to the gas volume between the tuning fork prongs whilst avoiding the surface of the tuning fork arms [10, 11]. Additionally, piezo-electric readout is prone to electromagnetic interference and is not safe in highly explosive environments. Future development of all-optical, interferometric-based readout is therefore pursued [12].

With these challenges in mind, a different integrated photothermal transducer is proposed in this chapter benefiting from the photothermal sensitiv-

ity enhancements while still utilizing the high-volume CMOS supply chain.

5.2 Photothermal enhancement

Contrary to optical transmission measurements where a change in transmission is an *indirect* indication of the optical absorbance as the light undergoes multiple other effects such as scattering and multiple reflections, photothermal spectroscopy probes solely the *direct* consequence of optical absorption [1]. This makes this method ideally suited for applications where scattering and reflections are known to be an issue, e.g. in the presence of aerosol particles [13].

Furthermore, PTS can be engineered to be more sensitive compared with conventional TDLAS methods, which is one of the main drivers to explore this route for miniaturized sensors [1]. The various enhancement effects compared to TDLAS and routes to improve them are now discussed.

One way to theoretically quantify the photothermal advantage was first proposed in the context of a photothermal lens spectroscopy experiment in 1979 [14]. This particular PTS experimental setup is almost identical to a normal transmission TDLAS experiment. The difference is that, after passing the sample, only the central portion of the laser beam is detected by limiting the field of view of the detector with a pinhole. The photothermal effect increases the temperature of the sample on the central axis of the beam and subsequently a weak refractive index gradient is formed which acts as a focussing (or defocussing) lens. The enhancement factor E_{PTS} in this context was defined as the ratio of the photothermal lensing signal to that obtained using conventional TDLAS (without the pinhole), assuming weakly absorbing media and that both measurements have the same limiting noise. Although this comparison is only strictly applicable for pinhole-based PTS experiments, it can still be used as a relative figure of merit for all other linear[2] photothermal spectroscopy methods since the physical origin of the output signal is common for all methods. This enhancement factor has the following general form, regardless of the exact photothermal mechanism [1]:

$$E_{PTS} = \frac{\Delta\mathfrak{T}_{PTS}}{\Delta\mathfrak{T}_{TDLAS}} = \frac{\mathcal{S}_{PTS}}{\mathcal{S}_{TDLAS}} = K\left|\left(\frac{dn}{dT}\right)\right|\frac{P_{pump}\gamma}{\lambda_{probe}\kappa} \tag{5.1}$$

with K a proportionality constant dependent on the exact geometry and

[1] Some classify PTS as an indirect method. In this definition, the term 'indirect' is used with respect to the optical measurement itself and not with respect to the optical absorbance.

[2] linear in the sense that the output signal is linear with optical power and concentration

photothermal transduction method, dn/dT the thermo-optic coefficient of the material, P_{pump} the optical excitation power, γ the thermal yield or the fraction of absorbed power not lost to radiative processes, λ_{probe} the wavelength used to probe the temperature change and κ is the thermal conductivity. The temperature change can be probed with the excitation beam (pump) as well, but as will become clear in this chapter, it is highly beneficial to use a secondary and much more cost-efficient (near-infrared) laser system instead. The photothermal signals are assumed to be linear with concentration (weakly absorbing) and therefore the same relation is true for the ratio of the sensitivities $\mathcal{S} = \partial\Delta\mathcal{T}/\partial C$. PTS can be designed through geometry in such a way as to maximize the perceived photothermal enhancement way beyond what TDLAS systems can achieve. This sensitivity advantage is further examined for the proposed on-chip photothermal spectroscopy sensor.

There is a second argument in favor of using PTS for weakly absorbing samples. Intuitively, weak light signals are easier to detect on top of a pitch black background as opposed to a tiny intensity drop on top of a strong light background. In a sense, PTS is a zero-baseline method. When there is no absorption, the detected signal is expected to be exactly zero. This SNR advantage for PTS systems can be modelled assuming that the absorption and detection processes are shot-noise limited and follow a Poisson statistic. For a pump-probe photothermal deflection spectroscopy configuration, representative of many PTS methods, it can be shown that the limiting SNR of the photothermal signal is given by [1]:

$$SNR_{PTS} = T\alpha L\sqrt{< n >}\sqrt{\frac{1}{(1-T)+(1-T)^2}} \tag{5.2}$$

with $T = e^{-\alpha L}$ and <n> the average number of photons. Using similar limitations, the following is found for conventional transmission spectroscopy.

$$SNR_{TDLAS} = \alpha L\sqrt{< n >}\sqrt{\frac{T}{1+T}} \tag{5.3}$$

The two methods are compared in Figure 5.2 (a) for $< n >= 1$. Under shot-noise limited conditions, the photothermal method outperforms TDLAS when transmission is larger than 50 % ($\alpha L < 0.7$) by a factor K_{SNR}, shown in Figure 5.2 (b). In the limit of weakly absorbing samples ($\alpha L << 1$) this factor is simplified to [1]:

$$K_{SNR} = \frac{SNR_{PTS}}{SNR_{TDLAS}} \sim (\alpha L)^{-1/2} \tag{5.4}$$

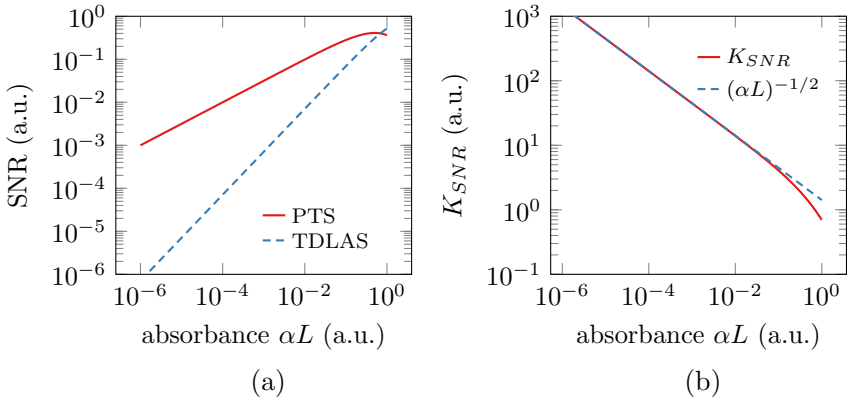

Figure 5.2: Theoretical comparison of Signal-to-Noise Ratio for shot-noise limited photothermal deflection spectroscopy (PTS) and conventional transmission spectroscopy (TDLAS), SNR values estimated for <n>=1 (a). The photothermal method outperforms TDLAS for weakly absorbing samples by a factor K_{SNR} (b).

which is independent of thermo-optical material properties.

Lastly, the choice of the probe-beam for detecting the photothermal effect is independent of the excitation pump beam. In the case of mid-infrared TDLAS applications, expensive cooled detectors are often required to detect the lower frequency photons. It is therefore advantageous to circumvent this need and greatly reduce the overall system cost by using standard, telecommunication band near-infrared lasers as the optical probe.

5.3 Integrated photothermal spectrometer

A possible implementation of photothermal mid-infrared spectroscopy in the SOI platform is outlined. The photothermal response is proportional to the optical absorption cross-section of the analyte and the spectroscopic information of the sample can be retrieved by scanning the wavelength of the optical excitation pump beam and recording the photothermal signal at each wavelength using a near-infrared optical probe. This approach circumvents the need of a costly and cooled mid-infrared detector and enhances the photothermal signal using a high Q microring resonator. By functionalizing the chip surface with a porous gas adsorbing coating it is possible to detect trace gas analytes.

Operation principle and signal model

The microring resonator (MRR) on the PIC is an optical notch filter

which is highly sensitive to tiny variations in the refractive index induced by the photothermal effect. The sensing principle is outlined in Figure 5.3. The analyte is deposited in the annular region of the microring resonator. For trace gas applications, the MRR is coated with a pre-concentrating porous coating to capture and trap the molecules to facilitate the thermal relaxation towards the PIC. A near-infrared (1550 nm) probe laser is coupled to the MRR and the wavelength λ_{probe} is tuned to the operation point where the the optical transmission $\mathcal{T}$ has the highest slope $\mathcal{T}' = d\mathcal{T}/d\lambda$. The wavelength selective absorption of mid-infrared radiation by the analyte gives rise to a wavelength selective temperature increase $\Delta T(\lambda_{pump})$ which is transferred to the resonator. In turn, the increase in temperature causes a change of effective index n_{eff}. The change Δn_{eff} is read out by monitoring the near-infrared probe transmission of the MRR. The resonance shift of the MRR is transduced to an observed transmission change $\Delta\mathcal{T}$ of the detected probe signal. By modulating the mid-infrared pump power, the MRR resonance shift will result in a modulated probe power $\Delta P_{probe}(\lambda_{pump})$ on a near-infrared detector, which can be read out sensitively using a lock-in type detection. A possible practical implementation of this PTS method is outlined at the end of this chapter. For proof-of-concept experiments, single mode fibers and grating couplers (for the probe beam) are used to deliver the laser beams to the chip.

A simple expression for the PTS signal and sensitivity can be derived assuming **small signal** modulation of the MRR filter. This resonance wavelength shift $\Delta\lambda_{probe}$ due to temperature increase $\Delta T(\lambda_{pump})$ of the ring waveguide is given by [15].

$$\Delta\lambda = \frac{\lambda_{res}}{n_{eff}}\left(\frac{\partial n_{eff}}{\partial T}\Delta T + \frac{\partial n_{eff}}{\partial \lambda}\Delta\lambda\right) + \lambda_{res}\epsilon\Delta T$$

with $\partial n_{eff}/\partial T$ the thermo-optic coefficient of silicon, $\partial n_{eff}/\partial\lambda$ the material dispersion and ϵ the thermal expansion coefficient. In silicon, ϵ ($\approx 2ppm/K$) is two orders of magnitude lower than the thermo-optic coefficient (180 ppm/K) and is therefore neglected. Together with the definition of the group index $n_g = n_{eff} - \lambda\partial n/\partial\lambda$ this reduces to

$$\Delta\lambda_{res} = \frac{\lambda_{0,res}}{n_g}\frac{\partial n}{\partial T}\Delta T(\lambda_{pump}) = a_T\Delta T(\lambda_{pump}) \tag{5.5}$$

with a_T the temperature sensitivity of the MRR resonance wavelength. The photothermally induced temperature modulation $\Delta T(\lambda_{pump})$ of the ring waveguide depends on the excitation power and material properties through

$$\Delta T = \gamma P_{pump} f\left[R_{ring}, \omega(\lambda)\right] R_{th} \overbrace{\left(1 - e^{-\alpha(\lambda_{pump})L_{eff}}\right)}^{\approx\alpha(\lambda_{pump})L_{eff}} \tag{5.6}$$

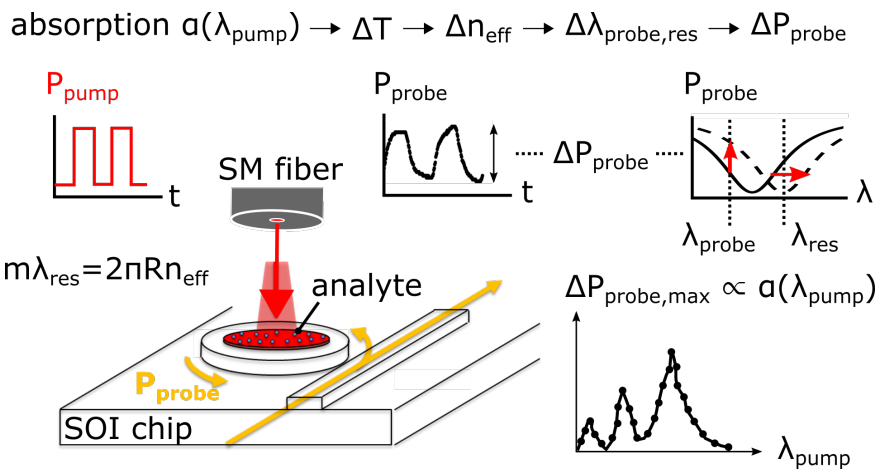

Figure 5.3: The heat generated through absorption of the mid-infrared pump beam increases the temperature of the ring resonator. Through the thermo-optic effect, the effective index of the waveguide changes, hereby changing the resonance wavelength λ_{res} of the microring. For a fixed probe wavelength λ_{probe}, a change in probe power ΔP_{probe} is measured using a near-infrared detector. The absorption spectrum of the analyte can be reconstructed by scanning the pump wavelength and recording the maximum probe modulation $\Delta \mathcal{T}_{probe,max}$.

with γ the thermal power yield which is the fraction of the absorbed power that is converted to heat. $(1-\gamma)$ is the fraction of the absorbed power re-emitted through luminescence processes [1]. P_{pump} is the total emitted pump power, f is the fraction of the pump power of a Gaussian beam contained within a radius R_{ring} for a beam with waist $\omega(\lambda)$, R_{th} is the effective thermal resistance between the absorbing analyte region and the ring waveguide cross-section, L is the effective thickness of the analyte and α is the total effective absorption coefficient of the analyte which includes background absorption of the medium and takes the enrichment factor E_c of the coating into account.

$$\alpha = \alpha_g E_c C + \alpha_{background} \tag{5.7}$$

with α_g the absorption coefficient of the pure analyte and C the volumetric concentration, for example expressed in ppm: liter gas volume/total air volume. The confinement factor in this case equals unity as the pump light is not evanescently coupled to the medium but passes through it. Note that only the steady-state temperature response is considered here. In subsequent experiments, the modulation frequency of the excitation beam was achieved using a mechanical chopper with a maximum frequency up to 10 kHz. This low-frequency range was found experimentally to have a com-

pletely flat response. For higher modulation frequencies closer to the thermal time constant limit of the device, the full dynamic response should be taken into account. The thermal time constant is estimated to be in the µs range. The complete Combining eq. 5.5 and 5.6, the observed probe beam transmission modulation amplitude $\Delta\mathcal{T}$ at the modulation frequency is then found with $\Delta\mathcal{T} = \mathcal{T}'\Delta\lambda_{res}$

$$\Delta\mathcal{T}_{probe} = \frac{d\mathcal{T}}{d\lambda}(\lambda_{probe})a\Delta T(\lambda_{pump}) \tag{5.8}$$

$$= \gamma a_T f P_{pump} R_{th} \mathcal{T}'(1 - e^{-\alpha L}) \tag{5.9}$$

On the photodetector side, the transmission modulation is transduced to a measurable voltage. The time-modulation of the optical probe power $P_{probe}(t)$ is detected using a standard near-infrared photodiode. This detector generates a current signal which is then converted and amplified using a built-in transimpedance amplifier (TIA) to a voltage signal. The voltage signal modulation is recovered sensitively by feeding the voltage time signal to a lock-in amplifier. The lock-in amplifier output $S(\lambda_{pump})$ is the RMS amplitude of the voltage signal at the modulation frequency. The key benefit of using the lock-in amplifier is that all other (noise) terms at other frequencies are highly suppressed. The measured signal at the excitation wavelength is then

$$S(\lambda_{pump}) = \Delta\mathcal{T} P_{probe} G/(2\sqrt{2}) \tag{5.10}$$

with G the net gain of the photodiode and TIA circuit in $[V/W]$ implicitly accounting for the responsivity of the detector

The MRR response, probe and pump powers can be measured at the same time. Assuming that the other parameters can be known or simulated beforehand, it is possible to calculate the analyte absorption spectrum $\alpha(\lambda)$ on-the-fly in an idealized case when there is no background absorption, i.e. the signal is truly zero when there is no analyte. This calculation does not require a pre-calibration step such as gas-purging of the analyte. Furthermore, in contrast to TDLAS, loss of optical alignment can be monitored by the near-infrared probe and accounted for in the calculation of the signal.

The sensitivity $\mathcal{S}$ of the proposed PTS method is estimated and compared to TDLAS (see also eq. 2.5) by differentiating eq. 5.9 with respect to analyte concentration.

$$\mathcal{S}_{PTS} = \left|\frac{\partial\Delta\mathcal{T}}{\partial C}\right| = \gamma a_T f E_c P_{pump} R_{th} \mathcal{T}' \alpha_g L e^{-\alpha L} \tag{5.11}$$

$$= E_{PTS} \times \mathcal{S}_{TDLAS} \tag{5.12}$$

where E_{PTS} is the net photothermal enhancement compared to optical transmission spectroscopy methods.

$$E_{PTS} = \gamma a_T f E_c P_{pump} R_{th} \mathcal{T}' \tag{5.13}$$

Note that the expression is similar to the general expression in eq. 5.1. In what follows, the terms of this equation are closely examined to yield optimal design with the highest enhancement factor.

5.4 Transmission slope of MRRs ($\mathcal{T}'$)

5.4.1 Basic operation

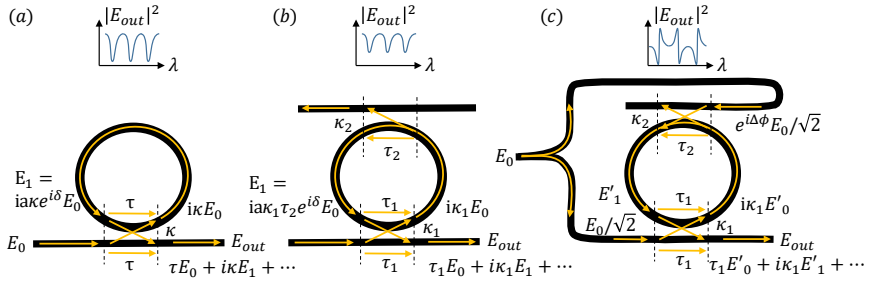

Figure 5.4: Schematic of optical microring resonators. Simplest all-pass filter (APF) (a), add-drop filter (ADF) (b) and add-drop design to induce Fano-like asymmetric resonances (c).

Microring resonators are an essential building block of silicon photonics and have contributed greatly to the success of silicon photonics, especially for WDM applications. The SOI platform is capable of fabricating ring resonators of unprecedented small size thanks to the high index contrast between silicon and the silicon dioxide and therefore ultrasmall bend radius. A generic MRR consists of a closed loop optical waveguide where the light is in resonance when the optical path length is exactly an integer number of the wavelength. The MRR therefore supports a multitude of resonances.

$$m\lambda_{res}/n_{eff} = 2\pi R \qquad m \in \mathbb{N} \tag{5.14}$$

In order to make a useful optical filter the ring waveguide must be coupled to the rest of the photonic circuit. Typically, this is achieved by evanescently coupling the optical mode to a single mode bus waveguide. As will be shown, the transmission spectrum features sharp Lorentzian-like dips around the resonance wavelengths [15]. This is essential for our PTS transducer as we

are looking for an optical filter with the highest possible transmission slope $\partial\mathcal{T}/\partial\lambda$ to maximize the sensitivity. Design and properties of MRRs are discussed in detail in [15]. Here, only a select number of key concepts relevant for the transducer design are reviewed.

5.4.2 All-Pass Filter

Simplest MRR circuit is a ring waveguide with a single coupling section that can evanescently couple the optical mode from the loop to a bus waveguide, see also Figure 5.4(a). All light in the access waveguide is transmitted except for those wavelengths λ_{res} that are resonantly coupled to the ring waveguide. This type of circuit is therefore called an all-pass or notch filter. Light close to λ_{res} is 'trapped' in the ring waveguide and makes approximately Q-number of optical cycles before the light fades due to scattering, absorption and outcoupling. Q is commonly referred to as the loaded quality-factor of the resonator [3]. The expressions for the transmission and Q-factor can be easily derived following the schematic in Figure 5.4 (a). We assume that the coupling section is reflectionless and lossless, therefore

$$\kappa^2 + \tau^2 = 1 \tag{5.15}$$

with κ and τ the electric field self-coupling and cross-coupling coefficients. After one roundtrip the light accumulates a phase term $e^{i\delta}$ and is attenuated by a:

$$\delta = 2\pi n_{eff} L_r/\lambda \tag{5.16}$$

$$a^2 = \exp\left(-\alpha L_r\right) \tag{5.17}$$

where $n_{eff}L_r$ is the optical roundtrip length and α is the ring waveguide power loss coefficient accounting for scattering, coupling and material losses. The field transmission E_{out} of the bus waveguide can be calculated by adding all the fields at the outputs

$$E_{out} = \tau E_0 + i\kappa E_1 + i\kappa E_2 + ...i\kappa E_n \tag{5.18}$$

$$= \tau E_0 + (i\kappa)^2 E_0 a e^{i\delta}\Big(1 + (\tau a e^{i\delta})^1 + (\tau a e^{i\delta})^2 + ... + (\tau a e^{i\delta})^n\Big) \tag{5.19}$$

$$= E_0\Big(\tau - \frac{\kappa^2 a e^{i\delta}}{1 - \tau a e^{i\delta}}\Big) \tag{5.20}$$

$$= E_0\Big(\frac{\tau - a e^{i\delta}}{1 - \tau a e^{i\delta}}\Big) \tag{5.21}$$

[3] The unloaded Q of a resonator is the theoretical Q-factor of the resonator not coupled to an external bus waveguide.

The transmission can then be further calculated as

$$\mathcal{T}_{APF} = \left|\frac{E_{out}}{E_0}\right|^2 = \frac{a^2 - 2a\tau\cos\delta + \tau^2}{1 - 2a\tau\cos\delta + (\tau a)^2} \tag{5.22}$$

It is instructive to approximate this expression near the resonance condition $\delta = m2\pi + \epsilon$ to second order in ϵ using $\cos\delta \approx 1 - \epsilon^2/2$

$$\mathcal{T}_{APF} = 1 - \frac{\kappa^2(1-a^2)/a\tau}{(1-a\tau)^2/a\tau - \epsilon^2} \tag{5.23}$$

This is further expressed in terms of wavelength shifts $\Delta\lambda$ near resonance using eq. 5.16

$$\Delta\lambda = \frac{\lambda_{res}^2}{2\pi n_g L_r}\epsilon \tag{5.24}$$

with n_g the group index of the waveguide. The transmission then has a Lorentzian form near resonance with the following Full Width at Half Maximum (FWHM)

$$\mathcal{T}_{APF} = 1 - \kappa^2 \frac{1-a^2}{(1-a\tau)^2}\frac{(FWHM/2)^2}{(FWHM/2)^2 + \Delta\lambda^2} \tag{5.25}$$

$$FWHM = \frac{(1-a\tau)\lambda_{res}^2}{\pi n_g L_r \sqrt{a\tau}} \tag{5.26}$$

From the expression, the ring is critically coupled when the transmission drops to zero ($a = \tau$), the extinction ratio is then maximal. For transducer applications we are interested in the slope of the filter $\partial\mathcal{T}/\partial\lambda = \mathcal{T}'$. The Lorentzian function eq. (5.26) has inflection points at $\lambda_{res} \pm \sqrt{3}/6 \times FWHM$ (-6dB point in transmission) with maximum slope

$$\left|\mathcal{T}'_{APF}\right|_{max} = \frac{3\sqrt{3}}{4}\kappa^2\frac{1-a^2}{(1-a\tau)^2}\frac{Q}{\lambda_{res}} \overset{a\to 1}{\approx} \frac{3\sqrt{3}}{4}\frac{Q}{\lambda_{res}} \approx 1.3\frac{Q}{\lambda} \tag{5.27}$$

which clearly scales with the Q-factor of the MRR. The quality factor and FWHM are related through $Q = \lambda_{res}/FWHM$ [16]. In order to maximize the transducer sensitivity, it is crucial to increase the Q-factor of the cavity. Eq. (5.26) suggests that a better Q-factor is obtained for large rings and small cavity losses. These two terms however are not independent as the propagation loss per roundtrip scales with the cavity length. A more detailed analysis on the optimal length as function of loss can be found here [15]. For a given ring size however, it is crucial to reduce the propagation, bend and coupler losses. This is achieved by high quality lithography and etching processes on the SOI platform as well as limiting the optical field intensity at the air-cladding interface by using rib waveguides, see also Figure 5.5 [17, 18]. The coupler losses are reduced by designing adiabatic, spline

bends instead of circular ones that allow for a smooth transition between the straight waveguide optical mode and circular waveguide mode [19]. In this way, there the reflections at the transition points are minimized leading to weaker *etalon* fringes in the output spectrum.

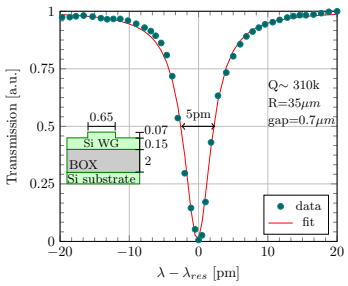

*Figure 5.5: Measured high-Q all-pass ring resonance at 1550 nm in the SOI-platform with ring radius R=35*µm *and coupling gap of 0.7*µm*. (b) The inset shows the rib waveguide cross-section, all dimensions are in* µm*.*

5.4.3 Add-Drop Filter

By adding a second bus waveguide to the ring, an add-drop filter is created which is widely used for WDM applications. At resonance, the incoming light is partially coupled to the drop port. Additionally, input from the 'add'-port can be added to the output at resonance. The transmission for the 'out' or 'pass'-port can be derived analogous to the APF transmission.

$$\mathcal{T}_{ADF} = \left|\frac{E_{out}}{E_0}\right|^2 = \frac{a^2\tau_2^2 - 2a\tau_1\tau_2\cos\delta + \tau_1^2}{1 - 2a\tau_1\tau_2\cos\delta + (a\tau_1\tau_2)^2} \tag{5.28}$$

For symmetrical coupling ($\kappa_1 = \kappa_2$,$\tau_1 = \tau_2$, the transmission spectrum is identical to that of APF, eq. (5.22) but with an increased net loss by a factor τ such that $a' = a\tau$. For a given waveguide platform and processing, the ADF will always produce lower Q-factors and therefore lower sensitivities compared to an APF.

5.4.4 Asymmetric Fano filter (AFF)

Fano resonances in microresonators have attracted considerable interest for sensing and fast optical switching application in the literature due to their asymmetric steep transmission feature and small wavelength range required for tuning from zero to full transmission [20–23]. However, it will be shown

that when analyzed in detail theoretically and experimentally, this benefit for our proposed PTS transducer is marginal or even worse when compared to APF under similar processing conditions. The benefit gained from the asymmetric lineshape is counteracted due to increased net round-trip loss a and therefore decreased Q-factor.

It is widely known that Fano-type resonant phenomena occur in microphotonics whenever a continuum of states coherently interacts with a multitude of discrete states [24, 25]. To understand how this occurs in the MRR, consider the APF in Figure 5.4(a) where the field incident on the coupler is split into a part which continues to travel in the bus waveguide and a part which circulates in the ring. The first part represents a continuum of optical modes in the bus waveguide and the second one is a summation of discrete localized states satisfying the resonant condition of the MRR. However, strangely enough no Fano-lineshape is observed in the APF configuration. Any Fano resonant phenomenon can be expressed with the following normalized Fano-Anderson equation for the absorption spectrum $\sigma(h\nu)$ in terms of the Fano asymmetry parameter $q = \cot\theta$ which is defined as the cotangens of the phase difference θ between the continuum and discrete states

$$\sigma(h\nu) = D^2 \frac{(q+\Omega)^2}{1+\Omega^2} \tag{5.29}$$

with ν the wavenumber, Ω the reduced frequency and $D = 2\sin\theta^2$ [24]. The reduced frequency centers the frequency axis on the resonance and scales it to the width (FWHM) of the resonance

$$\Omega(\nu) = \frac{2h(\nu - \nu_{res})}{FWHM} \tag{5.30}$$

The asymmetry is maximal whenever $q \pm 1$ and therefore occurs when the phase shift θ is an integer multiple times $\pi/4$. Now for the APF case, consider eq.(5.19) where it is clear that the phase shift is equal to $\theta_{APF} = \pi(2m+1)$ and therefore $q_{APF} \pm \infty$ for which the Fano-Anderson equation, eq. (5.29), reduces to a Lorentzian lineshape.

In order to obtain a Fano-like transmission spectrum we need to induce a phase shift in the bus-waveguide continuum or the discrete states. Reflections in the bus-waveguide can be used to achieve this [20, 22, 23]. Alternatively, an air-hole in the coupling section can induce the required fixed phase offset [25]. However, a more flexible and fabrication tolerant device can be made through two-beam interference in the MRR [21], see also Figure 5.4(c). In this circuit, the input field is split with a power splitter into two equal portions which couple to the input- and add-port of an ADF. By inducing a phase shift $\Delta\phi = \pi/2$ in one of the two input arms, the required phase shift $\theta \pm \pi/4$ between the continuum and MRR states can be achieved.

The expression for the output field are easily derived following the schematic in Figure 5.4(c) where we assume symmetric and lossless coupling sections $\tau = \tau_{1,2}, \kappa = \kappa_{1,2}$.

$$E_{out} = \tau E_0' + i\kappa E_1' + i\kappa E_2' + ...i\kappa E_n' \tag{5.31}$$

$$= \frac{\tau E_0}{\sqrt{2}} + (i\kappa)^2\sqrt{a}e^{i\delta}E_0\Big(\frac{\sqrt{a}\tau + e^{i(\Delta\phi-\delta/2)}}{\sqrt{2}}\Big)\Big(1 + ... + (\tau^2 a e^{i\delta})^n\Big) \tag{5.32}$$

$$= \frac{E_0}{\sqrt{2}}\Big[\tau - \Big(\frac{\kappa^2\sqrt{a}e^{i\delta}}{1-\tau^2 a e^{i\delta}}\Big)\Big(\sqrt{a}\tau + e^{i(\Delta\phi-\delta/2)}\Big)\Big] \tag{5.33}$$

Note now that the phase shift of the continuum E_0' with respect to the discrete states E_n' at resonance ($\delta = 2\pi m$) is now

$$\theta_{AFF} = \pi + 2\pi m + \arg(a\tau + \sqrt{a}e^{i(\Delta\phi - \pi m)}) \tag{5.34}$$

$$\overset{(a,\tau)\to 1}{\approx} \pi + 2\pi m + \frac{\Delta\phi}{2} - \frac{\pi m}{2} \tag{5.35}$$

$$\overset{\Delta\phi=\pi/2}{=} [2 + (-1)^{m+1}]\frac{\pi}{4} \tag{5.36}$$

so that the Fano parameter q is equal to ± 1 and the asymmetric lineshape for the transmission profile is expected. Note that the required phase shift of $\Delta\phi = \pi/2$ is only exact in limit of low loss and weak coupling $(a, \tau) \to 1$. The transmission can be further calculated with

$$\mathcal{T}_{AFF} = \Big|\frac{E_{out}}{E_0}\Big|^2 = \frac{1}{2|1-a\tau^2 e^{i\delta}|^2}\Big|\tau - a\tau e^{j\delta} - \sqrt{a}\kappa^2 e^{i(\Delta\phi+\delta/2)}\Big|^2 \tag{5.37}$$

It is instructive to approximate this expression near the resonance condition $\delta = m2\pi + \epsilon$ to first order in ϵ using $e^{i\delta} \approx 1 + i\epsilon$. The transmission is further simplified to

$$\begin{aligned}\mathcal{T}_{AFF} =& \frac{1}{2(1-a\tau^2)^2}\Big(\tau^2(1-a)^2 + a\kappa^4 - 2\tau(1-a)\sqrt{a}\kappa^2\cos\phi \\ &+(-1)^m[\sqrt{a}(1+a)\kappa^2\tau\sin\phi]\epsilon\Big)\end{aligned} \tag{5.38}$$

where it is clear that the maximum slope occurs when $\phi = \pi/2$. Expressing ϵ with respect to $\Delta\lambda$ gives the maximum wavelength sensitivity

$$\Big|\mathcal{T}'_{AFF}\Big|_{max} = \frac{Q_{ADF}}{\lambda}\frac{(1-\tau^2)(1+a)}{1-a\tau^2} \overset{(a,\tau)\to 1}{\approx} 2\frac{Q_{ADF}}{\lambda} \tag{5.39}$$

where the sensitivity is expressed in terms of a Q-factor of the same MRR in an ADF configuration. Comparing this to eq. (5.27) suggests a 50% increase in the maximum slope compared to the APF filter with equal coupling parameters. However, by introducing the second coupling section, the losses

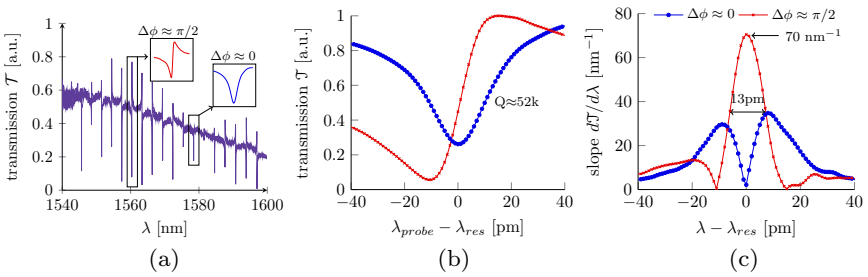

Figure 5.6: Measured transmission spectrum of an asymmetric Fano-resonant filter (a), realized using a co-directionally coupled ADF, see also Figure5.4. By utilizing the waveguide dispersion, a resonance can always be found with a phase shift of $\Delta\phi = \pi/2$ between the input- and add-port resulting in an asymmetric Fano lineshape (b). The maximum slope is twice as high compared to a resonance where $\Delta\phi = 0$ (c).

will increase and therefore Q_{ADF} will always be lower than Q_{APF}. Further numerical analysis with optimal $\tau_{optimal}$ for each configuration shows that, for a given loss condition a, the asymmetric Fano design will indeed outperform the ADF configuration marginally but not the APF, see also Figure 5.7.

This has been experimentally verified by fabricating both APF and AFF circuits on the same waveguide platform and therefore comparable intrinsic loss parameters a. For the circuit proposed in Figure 5.4 (c), the required phase delay $\Delta\phi$ is achieved through waveguide dispersion by making one arm after the initial splitter longer. Similar to eq. (5.24), the dispersion scales approximately linearly with wavelength and optical path delay ΔL. For practical applications, this is a more easy and passive solution than active phase tuning with heaters as in [21]. The lower arm of the splitter is chosen to be $8\mu m$ longer such that phase delay changes by $\Delta\phi/\Delta\lambda \approx \pi/35nm^{-1}$. By using a MRR with a roundtrip length of 220 µm the FSR is approximately 3.1 nm. This results in a sampling of about ten resonances between $\Delta\phi = 0$ and $\Delta\phi = \pi$, see aslo Figure 5.6(a) [26]. In this manner, it is always possible to find a resonance peak corresponding to the desired asymmetric Fano shape $\Delta\phi = \pi/2$ with an accuracy of $\approx \pi/20$. Unsurprisingly, when comparing the Fano resonance to the one with $\Delta\phi = 0$, the slope is about twice as high, see also Figure 5.6(b,c). However, APF filters were fabricated on the same chip with measured Q-factors in excess of 300k which have even higher slope values. Hypothetically, it is possible to achieve better sensitivity than an APF configuration by adjusting the phase balance in the coupling section by etching nano-scale air holes therein [25]. Next to practical challenges for large scale fabrication, initial results suggest a

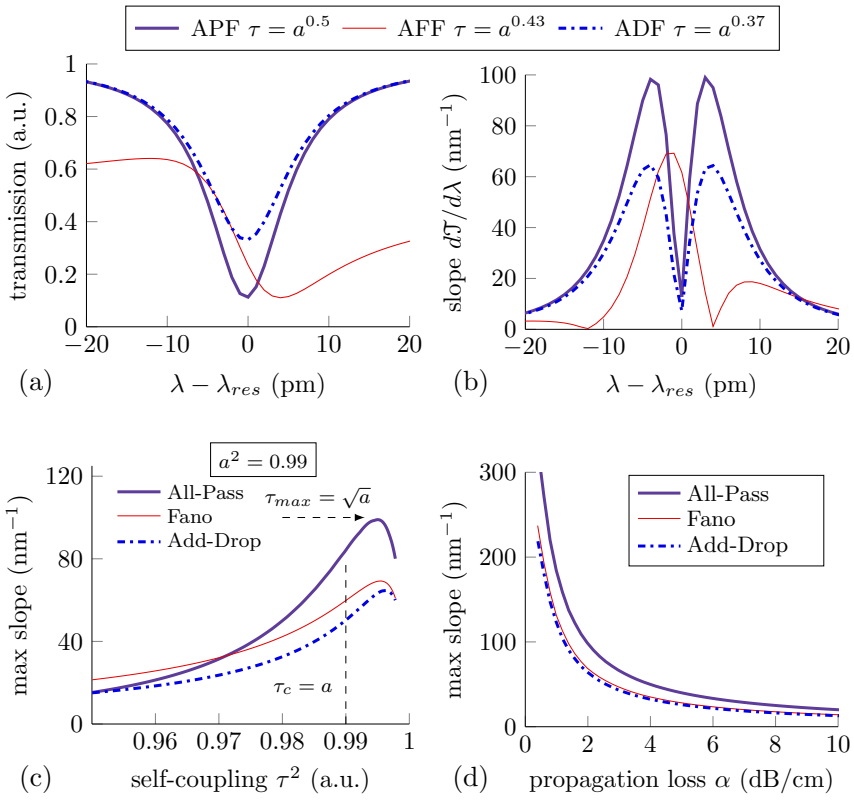

Figure 5.7: Simulated transmission spectrum of different MRR configurations: APF, ADF and AFF, see also Figure 5.4 for a MRR of 35 µm *ring radius and propagation loss α=2dB/cm (a^2=0.99) (a). The slope of the transmission is proportional to the PTS signal (b). The optimal self-coupling constant τ is chosen such as to maximize the slope of the transmission (c). Note that this does not correspond to a critically coupled MRR but an undercoupled ring with reduced extinction ratio. The parameters for the APF correspond with a loaded Q-factor of 250k. The slope is maximized by reducing the waveguide propagation losses (d). For a given loss, the APF outperforms other configurations.*

significant insertion loss increase.

5.4.5 Design guidelines and conclusions

It is clear that a high Q-factor resonator is desirable as it will result in higher sensitivity for the PTS transducer, see also eq.(5.13). To achieve this, propagation and coupling losses have to be minimized. Ultra high-Q disk resonators have been shown [27]. However, from a practical point of view, it

becomes quite difficult to lock the probe wavelength to the maximum slope of the MRR. The 3dB bandwidth ($FWHM'$) of the slope function $\mathcal{T}'(\lambda)$ is approximately 0.6 times smaller than the $FWHM$ of the APF transmission, which scales inverse proportionally with Q. Given a Q factor of about 300k, this will result in an operational bandwidth for the probe wavelength of the transducer of merely 3pm. The accuracy of typical telecom external cavity lasers is around 1 pm. Therefore it can be argued that MRRs with Q factors below 200k are a good trade-off between sensitivity and practical feasibility without resorting to more advanced control circuits.
In summary

- The All-Pass filter yields the highest slope sensitivity for a given waveguide propagation loss.
- To increase sensitivity it is important to reduce the propagation and coupling losses to a minimum. However, ultra high-Q (>300k) devices become less practical.
- The highest slope occurs when the MRR is slightly undercoupled $\tau \approx \sqrt{a}$.
- The only advantage of Fano-resonant structures is that there is a singular optimal operation point which makes it more practical for self-alignment feedback loops by searching for the global maximum of the photothermal signal.
- For trace gas experiments, a gas adsorbing coating is required. In order to maintain the high Q factor of the MRR, the coating is patterned in the annular region of the MRR, so that the optical mode of the probe and waveguide structures are not perturbed.

5.5 Excited state relaxation and thermal yield (γ)

After optical absorption, the analyte molecules are in an excited state. Typically, the excited state will relax and convert the photon energy to sample heating. Under steady-state conditions, the power absorbed by the sample may be lost through luminescence processes which we take into account with the γ factor [1]. It is however dependent on the type of compound measured and varies slowly with wavelength. To our advantage, the photoluminescence (PL) yield (1-γ) is typically lower in the mid-infrared wavelength range as opposed to VIS or near-IR optical frequencies which increases the sensitivity of the PTS method.

The reason for this is two-fold: the fluorescence rate decreases with the third power of the wavelength while the non-radiative transition rates increase exponentially with wavelength [28]. This can be understood by considering a simple two-level state (1,2) system with radiative processes which are governed by the Einstein coefficients of absorption B_{12} ($J^{-1}m^3s^{-2}$), B_{21} and emission A_{21} (s^{-1}). The spontaneous emission coefficient A_{21} corresponds to the rate of luminescence processes $K_{rad,2}$ in this system and scales with the third power of the wavenumber ν and B_{12}-coefficient of absorption [1, 28].

$$A_{21} = \frac{8\pi h\nu^3}{c^3} B_{12} = K_{rad,2-level} \tag{5.40}$$

This analysis can be extended to polyatomic systems with similar trends for the fluorescence rates: the fluorescence rate is proportional to ν^3 or alternatively λ^{-3} [29]. Secondly, the fluorescence processes are competing with radiationless transitions such as the Internal Conversions (ICs) and Inter System Crossings (ISCs) which represent conversion of electronic energy of an excited state to vibrational energy in a lower-energy electronic state. The rate constants for these processes abide the empirical 'energy gap law' stating that the rates increase exponentially with decreasing energy differences between two electronic states. More detailed information can be found in Chapter 2 of [28] and [1]. Considering these two effects, the luminescence quantum yield (1- γ), which is defined by the ratio of the radiative versus non-radiative rates, is negligible for most materials in the mid-infrared wavelength range.

$$1 - \gamma = PL_{quantum\ \ yield} = \frac{K_{radiative}}{K_{radiative} + K_{non-radiative}} \tag{5.41}$$

As an example, in [30] the quantum yield of HgTe mid-infrared colloidal quantum dots has been rigorously measured in the mid-infrared. Typical values in the 3-4 µm wavelength region are below 2%. As a corollary the non-radiative yield γ is close to unity.
Regarding time-dependent photothermal heating, the thermal energy transfer cannot be viewed as an instantaneous process and consists of several rates related to the different nonradiative relaxation processes (rovibrational relaxation, IC and ISC crossings) with different relaxation rates. For low-concentration samples, the energy receiving matrix surrounding the analyte can be considered as constant and therefore the energy relaxation can be modelled as a sum of pseudo-first order processes. A system in an excited state with added energy $E = h\nu$ will have thermal energy $E_H(t)$ relaxation according to

$$E_H(t) = E \sum^{n} \gamma_n (1 - e^{-k_n t}) = ER(t) \tag{5.42}$$

with k_n the relaxation rate constant and γ_n the nonradiative yield of the n-th process. The time-dependent thermal power impulse response is then simply found with $Q_H(t) = ER'(t)$ with $R'(t) = dR/dt$ the relaxation function. In the general case, the thermal power time-evolution is found by convolving the time-dependent excitation power $P_{pump}(t)$ with the relaxation function [1].

$$Q_H(t) = \int_0^t P_{pump}(\tau)R'(t-\tau)d\tau = P_{pump}(t) * R'(t) \tag{5.43}$$

For continuous excitation, the steady-state heat power is then just $Q_H = P_{pump} \sum \gamma_n = \gamma P_{pump}$. Thermal relaxation rates slower than the optical excitation rate will not yield a measurable temperature contribution. This should be taken into account when modelling time-dependent excitation photothermal phenomena. For example, photoacoustic sensors (PAS) of trace gases such as CO_2 have maximum signal when they operate at modulation frequencies lower than 1kHz, much slower than the molecular relaxation rate. Other gases in the mixture such as water vapor and oxygen can dramatically affect the kinetic relaxation rate of the analyte and therefore the photoacoustic signal even when the contaminant is not absorbing any light at the excitation wavelength [31, 32]. In an unknown gas mixture, the photothermal signal will therefore not only depend on the overlapping optical absorption features but will also depend on the kinetic interactions between the different gas species which can (de)amplify the signal and reduce the SNR of the experiment. Alternatively, when the kinetics are well known a priori, this can be used in a mixture with overlapping absorption features to distinguish between the different components coming from different molecular relaxation rates by varying the modulation frequency and collecting phase information of the signal [33].

5.6 Optical beam overlap (f)

For the proposed photothermal transducer, a tunable mid-infrared source needs to illuminate the gas-containing coating on top of the ring from a certain distance z. Optics in the read-out unit can ensure that a Gaussian beam with a predefined spot size 2ω is incident on the coating[4]. The optical power of the pump contained within a radius r, $P_{pump}(r)$ for a Gaussian

[4] $\geq$ than the focal point beam waist $2\omega_0$

beam[5] is given by:

$$\begin{aligned} P_{pump}(r, \lambda_{pump}) &= P_{pump}(\lambda_{pump})\left[1 - exp\left(\frac{-2r^2}{\omega^2}\right)\right] \\ &= P_{pump}(\lambda_{pump}) f(r, \omega) \end{aligned} \tag{5.44}$$

with P_{pump} the total pump power at the mid-infrared wavelength λ_{pump}. The choice of the beam waist at the coating surface introduces a trade-off between signal level and alignment tolerances. When $\omega > R_{ring}$, the tolerance to misalignment drifts of the pump beam axis and the axis of the ring resonator will be higher but a smaller fraction $f(r, \omega)$ of the pump light is used, giving a lower signal. It is projected that only the case when $\omega > R_{ring}$ will be feasible for practical applications. The optimal beam dimensions and thus $f(r, \omega)$ will depend on the practical realization of the read-out unit together with the beam shaping/scanning optics. In the conducted proof-of-concept experiments, the beam waist is controlled by adjusting the pump fiber distance z to the chip. The fibers are single-mode so that the beam has a Gaussian profile and therefore follows

$$\omega(z) = \omega_0 \sqrt{1 + \left(\frac{z\lambda}{\pi\omega_0^2}\right)^2} \tag{5.45}$$

where $2\omega_0$ is the Mode-Field Diameter (MFD) of the pump fiber. At $\lambda_{pump} = 3.5\mu m$, ω_0 is approximately 7 µm.
For ease of use single-mode mid-infrared fibers are used in subsequent experiments. However, instead of using fibers, collimation optics can be used for the probe and pump beam to produce a collimated beam with a certain waist. A pump beam at 3.5 µm wavelength with a diameter of 1 mm has a Rayleigh range of more than 20 cm which would be sufficient for stand-off measurement applications. The probe beam can flood illuminate the grating couplers used to interface with the ring resonator. The transmitted probe signal could then be collected by a near-IR camera [34]. To further relax the alignment requirements between the pump beam and the microring one benefits from using a larger beam diameter of e.g. 1mm. By flood illumination of the microring, small position variations of the beam would then not affect the average pump power density delivered to the coating. For a 1mm beam diameter on the chip at 3.5 µm wavelength, the power density is within 10% of the maximum value inside a region of 160 µm radius. The fraction of the pump power contained within the microring radius of 25 µm in this case would be equal to $f \approx 5 \times 10^{-3}$. However, it is believed that

[5] 'Real' optical beams are characterized in terms of the beam-quality parameter M^2 which describes how closely the beam matches to a diffraction-limited Gaussian beam.

coating pre-concentration factors E_c can be as high as 10^5 which would compensate for this loss. As only the ring can be illuminated with the mid-IR beam, an optical aperture can be defined on top of the ring resonator sensor, that is aligned with the ring resonator, reflecting or absorbing all other pump light, see also Figure 5.8.

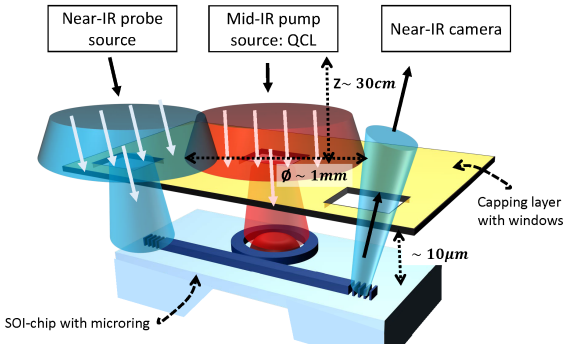

Figure 5.8: Schematic of a possible free-space measurement configuration. The probe and pump sources flood-illuminate the chip from a certain distance, e.g. 30cm. Collimating optics can be devised to ensure a 1mm ⌀ beam diameter on the chip. The SOI-chip is capped with a reflective or absorbing second layer (e.g. gold-coated silicon) with spacers (not shown in schematic). Small apertures (uncoated areas of the capping layer) are aligned on top of the microring and the input/output ports of the probe. The probe signal is collected by a near-IR camera.

5.7 Thermal isolation (R_{th})

The effective thermal resistance R_{th}(K/W) of the MRR is estimated using a 3D-axial symmetric Finite Element Method (FEM) computation in *COMSOL*. The absorbing analyte is modelled as a uniform heat generating cylindrical object in the annular region of the MRR with radius $R_{ring}-2\mu m$. It can be assumed uniform when the pump beam radius is larger than the MRR ($R_{pump} > R_{ring}$) so that the optical intensity is approximately constant over the analyte region, e.g. a coating with adsorbed gas molecules. The steady state temperature distribution is calculated for heat generated on top of the MRR. The average temperature increase in the ring waveguide cross-section is evaluated yielding an effective thermal resistance R_{th} in K/W. Instead of using this lumped approach, it is possible to compute the MRR resonance shift more accurately for an arbitrary temperature distribution over the waveguide cross-section using first-order cavity perturbation

theory [35].

$$\Delta\omega = -\frac{\omega}{2}\frac{\int\int 2n\frac{dn}{dT}\Delta T(x,y)|E(x,y)|^2 dA}{\int\int \epsilon(x,y)|E(x)|^2 dA} \tag{5.46}$$

with ω the optical angular frequency, ΔT and E the distribution of the temperature change and electric field over the ring waveguide cross-section and ϵ is the dielectric constant cross-section of ring waveguide. From FEM simulation, the temperature change profile $\Delta T(x,y)$ over the cross-section is almost exactly constant, so that the expression is reduced to eq. (5.5). Furthermore, for a constant heat power, the thermal resistance scales inversely with the area of the MRR, $R_{th} \sim R_{ring}^{-2}$. Somewhat intuitively, for a given pump power, the highest temperature increase will occur when the beam is focused down to a small MRR with matching waist. However, from a practical point of view this approach is less suitable as explained in the previous section. Moreover, smaller MRRs have higher bending losses which lead to lower Q factors. A good trade-off value for the size of the MRR is found to be about 20-40 µm.
To increase the PT signal it is important to maximize the thermal isolation of the MRR device. Practically, there are two strategies to achieve this on the SOI platform.

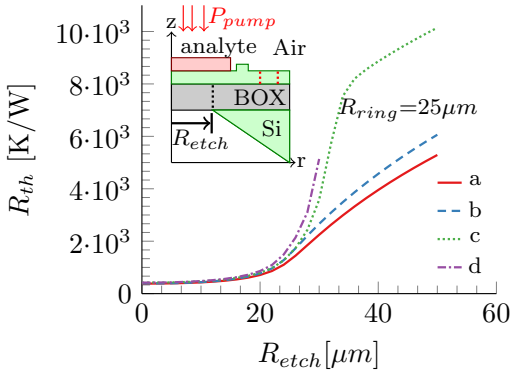

Figure 5.9: 3D-axial symmetric FEM simulation of R_{th} for a thermally isolated MRR by backside Si substrate removal (a) for different opening etch-radii R_{etch}. The inset shows a radial cross-section of the MRR. The ring is further thermally isolated by etching away the BOX underneath (b), by dry etching an opening in the top device layer (c) or both (d), see also the dashed etch-lines in the inset. In case (d), the MRR is supported only when R_{etch}<R_{ring}.

- Frontside etching. The BOX layer underneath the MRR is etched away with liquid- or vapor HF through openings in the top silicon

device layer so that the MRR is surrouned by air (thermal insulator) as much as possible. The etch-openings to the BOX can be predefined in the top Si layer in the center and at the rim of the MRR. However, SiO_2 pedestals or Si tethers are then still required to support the MRR structure which will inevitable reduce the thermal isolation value. There is an additional risk that the membrane will stick to the silicon substrate which is an added fabrication complexity.

- Backside etching. The silicon substrate is removed locally through anisotropic wet etching in a KOH-solution. This is a well-known and highly used process for MEMS fabrication [36]. A Si_3N_4 hardmask is patterned on the polished backside of the chip and wet etching is performed in a sealed teflon holder to protect the top silicon device layer, see also Figure 5.9. Alternatively, this can also be realized using Deep Reactive Ion Etching (DRIE) [37]. Afterwards, the MRR is ideally only connected to the bulk of the chip through the remaining BOX membrane. Inevitably, the access waveguides of the MRR on the top surface will leak a portion of the thermal heat away to the bulk of the chip.

Simulation results for backside etching show that by locally etching away the silicon substrate, one can improve the thermal resistance up to around 10^4 K/W for a 25µm ring, a two order of magnitude signal improvement. From simulation, frontside etching is not advised as similar thermal isolation values can only be achieved with ultra short pedestals, which cannot be reliably realized in practice as precise etching times are required. The BOX removal with KOH-etching is a much more reliable process, as the etch selectivity of SiO_2:Si is more than 1:100 so that the etch effectively stops at the BOX boundary.

5.8 Gas adsorbing coatings (E_c)

Inorganic and polymer coatings have been studied extensively in the past two decades as gas sensitive materials for a variety of applications such as catalysis, electrochemistry and sensors [34, 38–41]. The fundamental process involved is the enrichment of the target analyte at the surface of the adsorbent. In particular, thin films with nanoscale pores can have a tremendously large surface area per unit volume which boosts the apparent gas concentration inside the coating as compared to the headspace environment leading to more sensitive devices. Nanoporous materials are typically characterized based on the pore dimension: microporous ($<$ 2nm), mesoporous (2-50nm) and macroporous ($>$50 nm). Furthermore, various func-

tionalization molecules can be deposited onto the high surface area nanoporous structure for enhanced response and specificity towards a specific gas molecule [34, 39, 42]. The porous structures can be synthesized in many different types of materials such as metal oxides, zeolites, silicates, metal-organic-frameworks (MOF) and polymers where sol-gel or colloidal chemistry techniques are typically used.
A great deal of chemical insight is needed to select the best possible coating for the application at hand. Porous silica films are the most attractive choice for functionalizing SOI chips in view of their optical transparency in the NIR and SWIR[6], mechanical stability, precise thickness-, homogeneity- and pore size control [43]. Spincoating of silica-based films is the preferred approach for the functionalization of SOI chips. A smooth homogeneous porous thin film does not detriment the Si device layer properties significantly in terms of waveguide loss at NIR (probe wavelength range) wavelengths because the induced surface roughness at the interface is kept to a minimum. Several different types of coatings were developed in the context of the CheckPack project at "Centrum voor Oppervlaktechemie en Katalyse" (COK), KULeuven which target a specific chemical group of gases present in the headspace of MAPs. Some of these were successfully patterned and coated onto MRR chips with some preliminary trace gas PTS results. The most promising coatings for on-chip applications are

- *COK, KULeuven*: **Microporous silica alumina**. A microporous silica matrix where a portion of the Si atoms is replaced by Al. This increases the specificity towards N-containing compounds such as amines due to the acid-base interaction with Al. These have been successfully demonstrated for refractive index based gas sensing in previous works [39, 41].

- *COK, KULeuven*: **Metal organic framework (Cu-BTC)**. Crystalline structures built from metal ions and organic ligands. Volatile sulphur compounds can irreversibly bind to the Cu-ion of the MOF, hereby collapsing the crystalline structure leading to remarkably large changes in the refractive index [41].

- *COK, KULeuven*: **Hydrophobic spherosilicates**. Spherosilicate building blocks made up of a cubic silica structure with hydrophobic functional side groups [$-$O$-$Si$-$R$_4$] [41]. Preliminary results show heavily reduced uptake of water compared to mesoporous silica.

- *TUWien*: **Mesoporous silica with HMDS**. Aspecific mesoporous

[6]compared to other coating types such as polymer coatings which absorb heavily in the IR.

silica coating suitable for many hydrocarbon- and aromatic trace gases with sufficiently **low** vapor pressure, e.g. toluene and hexane. An extra hydrophobic thin film of hexamethyldisilazane (HMDS) is defined on top of the coating [40].

An in-depth discussion on the design, fabrication and characterization of the coatings developed at COK, KULeuven can be found in [39, 41].

5.8.1 Adsorption isotherm

The adsorption and desorption of molecules on the surface is a dynamic process and can be modelled in the quasi-static equilibrium. The number of gas molecules physisorbed and/or chemically bound to the porous surface will depend on the coating properties, gas species and the gas pressure[7]. A distinction is made between physical, reversible weak adsorption through Van der Waals forces (physisorption) and chemical strong binding to the coating surface (chemisorption). The former is a fast reversible process while the latter is partially reversible at elevated temperatures. The relationship between the total amount of adsorbed molecules at a given temperature and the gas pressure is called the **adsorption isotherm**. For low gas concentration (low pressure) it is common to use the the Langmuir theory for adsorption which considers that only a monolayer of adsorbents is formed on the available surface area inside the pores [40, 44].

$$q_c = \frac{q_m K_L c}{1 + K_L c} \tag{5.47}$$

where q_c is the adsorbed mass (g/l), q_m the maximum adsorption capacity (g/l), K_L the Langmuir constant (l/g) and c the analyte concentration (g/l). For low concentrations, the gas enrichment factor for the PTS signal E_c follows from the Langmuir constant $E_c = q_m K_L$. Example of an adsorption isotherm for microporous silica coating functionalized with Al for enhanced affinity towards amines (NH_3) is given in Figure 5.10(a). The Langmuir isotherm is calculated with parameters from experimental data in [41]. A maximum reversible adsorption capacity of q_m=117 g/l at 1000 ppmv NH_3 was observed[8] with apparent concentration enhancement $> 10^5$ in the low concentration range. The units of adsorbed amount q_m can be expressed in terms of ppmv[9] by multiplying with $M_w^{-1} V_m$, where M_w is the molar weight of NH_3 and V_m the molar volume of the gas. When appropriate,

[7] which is proportional to the gas volume concentration in the headspace.

[8] 117 g/l estimated from 2.6 mmol/(gram coating) and converted to [g/l] using molar mass and coating density values from [41]

[9] the volume that the gas molecules would occupy when desorbed from 1 L of coating volume

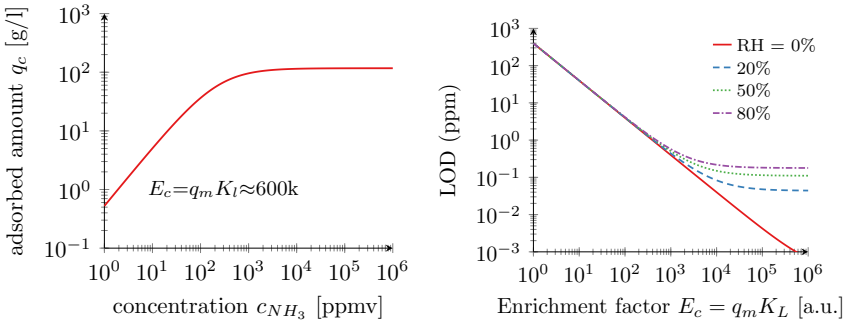

Figure 5.10: Adsorption isotherm for microporous silica coating functionalized with Al for enhanced affinity towards ammonia NH_3. Langmuir isotherm calculated with parameters from experimental data in [41], physisorbed adsorption capacity q_m=117 g/l at 1000ppmv NH_3 (a). Estimated LOD for coating-enhanced TDLAS of NH_3 at 3µm for different relative humidities at 300K, with α_{wg}=2dB/cm, $\Delta\mathfrak{T}_{min} = 10^{-4}$ and constant saturation concentration q_m=117g/l (b).

multilayer adsorption phenomena and the limits for high concentration can be modelled more accurately using the Brunauer–Emmett–Teller (BET) theory of adsorption [45]. This theory is an extension of the Langmuir theory to multilayer adsorption using the following key assumptions. The gas molecules only interact with adjacent layers, each layer is treated using the Langmuir theory. The adsorption enthalpy energy for the first layer is constant and greater than the subsequent layer. The evaluation of this model is outside the scope of this work.

5.8.2 Influence of water background

The main drawback of any coating element is that other (unwanted) molecular species will compete for the population of the adsorption sites. In particular, ubiquitous water molecules are the main source of competition. To model multi-species adsorption, a common approximation is that the adsorption sites can only accommodate one molecule of each type but not both and that they do not interact with each other. In many practical applications, the concentration of water vapor is many orders of magnitude higher than the analyte (trace gas) and all other contaminants so that in most cases the influence of water will be the main contribution. This leads to the following Langmuir expression for the fractional site occupancy θ of

the adsorption process.

$$\theta_c = \frac{q_c}{q_m} = \frac{K_L c}{1 + K_L c + K_w c_w} \tag{5.48}$$

$$\theta_w = \frac{q_w}{q_m} = \frac{K_w c_w}{1 + K_L c + K_w c_w} \tag{5.49}$$

with K_w the Langmuir constant for water and c_w the water concentration. The concentration of water vapor is many orders of magnitude higher than the analyte (trace gas) so that the apparent enrichment factor for the gas of interest is reduced to

$$E_c = \frac{q_c}{c}\Big|_{c\to 0} = \frac{q_m K_L}{1 + K_w c_w} \tag{5.50}$$

Furthermore, any absorption coming from the water molecules will add up to the background absorption coefficient $\alpha_{background}$ and deteriorate the sensitivity further, see also the exponential factor in eq. (5.12).

$$\alpha_{total} = \alpha_g E_c c_g + \overbrace{\alpha_w E_w c_w + \alpha_{wg} + \alpha_{coating}}^{\alpha_{background}} \tag{5.51}$$

The negative influence of water is a persistent problem for spectroscopy in general as the absorption lines are closely packed across the full IR spectrum apart from a few windows.

There is quite some interest in the literature to use gas adsorbing coatings for on-chip TDLAS sensors in order to alleviate the problem of the small optical interaction length available on-chip. In particular, use of coatings in the mid-infrared wavelength range for on-chip TDLAS holds promise to break the sub-ppm limit [40, 46]. It is instructive to calculate the theoretical LOD with realistic parameters. Predictions for ammonia gas detection in the $3\mu m$ wavelength region as a function of enrichment factor E_c is shown in Figure 5.10(b), assuming $\Delta\mathcal{T}_{min} = 10^{-4}$, α_g=1.58 cm^{-1}, $\alpha_w \approx 2{\cdot}10^{-2}$cm^{-1} and α_{wg} = 2 dB/cm with the assumption that the coating matrix itself is transparent. The influence of water in % relative humidity (RH) is modelled using the competitive Langmuir model with equal affinity $K_L = K_w$ and measured coating parameters from Figure 5.10(a). It is clear that even in this simple model, the presence of water will significantly limit the LOD. Note that the LOD for PTS systems is expected to follow the same trend as in Figure 5.10(b) but shifted to lower LODs by the photothermal enhancement factor E_{PTS}, eq. (5.13). In order to mitigate water interference, it is essential to introduce hydrophobicity to the coating material. Two approaches were investigated. The Spherosilicate porous coatings developed at COK have a surface which is inherently hydrophobic. However, thin film patterning and porosity control is still an ongoing research topic [41].

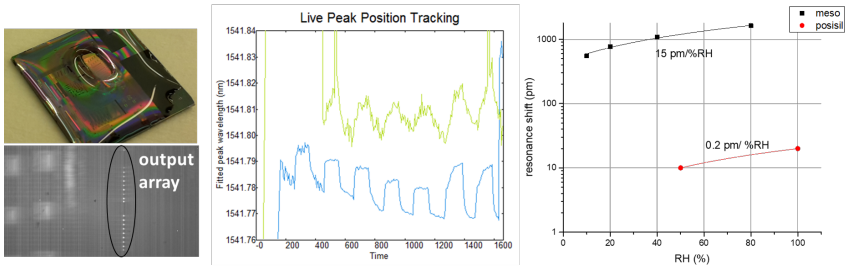

Figure 5.11: Refractive index experiment to evaluate the hydrophobicity of the PoSiSil coating (spherosilicate). An infrared laser and camera system track the resonance wavelength of several MRRs which are coated and exposed to water vapor. Adsorbed molecules change the refractive index inside the coating (density change) which is measured as a resonance shift. The photograph shows that the coated region has a high contact angle with water. The spherosilicate coating has two orders of magnitude lower response to water than a comparable mesoporous coating.

Some preliminary experiments were conducted to characterize the water hydrophobicity using a refractive index sensing experiment, with the exact same setup as in [39]. Chips containing MRRs were uniformly coated with a thin 100 nm layer of the spherosilicate coating such that any change in refractive index inside the pores due to analyte uptake would translate to a resonance shift of the MRR. This static change of the resonance is monitored live using a Xenics IR camera, collecting several MRR responses at the same time. More information on the intricacies of the refractive index setup and fabrication parameters of the coating are found in [39, 41]. The results for water adsorption compared to mesoporous Al coatings are given in Figure 5.11. The adsorption slope and maximum adsorbed amount of water for the spherosilicate is two orders of magnitude lower. The sensitivity, expressed as MRR resonance shift/%RH at room temperature, of the hydrophobic coating is lower towards target analytes such as ethanol (130pm/%RH) and acetone (120pm/%RH) compared to mesoporous Al coating towards ammonia (6000pm/%RH). However, the comparative SNR in humid conditions is stil a factor ≈ 5 better for the un-optimized spherosilicate coating. Further improvement is expected by improving the porosity of the coating [41]. The advantage is even higher when compared to non-functionalized mesoporous silica coatings, e.g. without the Al sites.

A different approach is to deposit a thin film such as HMDS that is water-repellant but is still thin enough to allow for diffusion of the trace gas analyte. The latter has produced the most promising initial results for on-chip PTS of toluene gas.

The main challenge for practical **quantitative** analysis of trace gases using gas adsorbing coatings is the fact that the apparent concentration enhancement is a highly non-linear function in the multi-parameter space of temperature, humidity, exact pore size, thickness and fabrication parameters, gas pressure, analyte type and multi-species interaction. For practical applications, all these effects would need to be analyzed and calibrated for. It is clear that high inter-dependency of compounds will translate to a very small region in the parameter space where $E_c(c)$ can be linearized, limiting the dynamic range of the sensor. It is therefore beneficial to focus on developing an array of coatings with different specificity functionalizations that could help to resolve the inter-dependency. A second major issue involved in the practical use of coatings is the ageing of the coating, putting severe constraints on recalibration of the sensor. In practice, it was found that mesoporous Al coatings lose their properties in ambient (humid) environment after a few months and have to be stored in desiccators.

5.9 Proof-of-Concept experiment

In order to test the proposed PTS transducer and evaluate the experimental LOD, a mock-up analyte was patterned inside the MRR annular region instead of the gas adsorbing coating [47]. The chosen analyte is a polymer photoresist with organic absorption bands in the SWIR (3-4µm) wavelength range which were accurately determined for comparison using conventional bench-top spectroscopic tools. Furthermore, the thickness is precisely controlled with the spincoating process.

5.9.1 Fabrication

The air-clad ring resonator devices were fabricated using a Multi Project Wafer service (MPW) in the 200 mm CMOS-pilot line at imec. [48] The silicon device layer is 220 nm thick and rests on a 2 µm thick buried thermal oxide (BOX). The TE-polarization grating couplers are defined using a 70 nm etch step. To achieve high-Q factor resonators, rib waveguides were used with an etch depth of 70 nm and 650 nm waveguide width. The ring resonators have a radius of 25 µm. A gap of 750 nm between the bus waveguide and ring resonator was chosen to obtain critical coupling. A positive photoresist AZ5214 from MicroChem was used as the mock-up analyte for the experiments. The resist was spin-coated and patterned in the annular region of the resonators using standard photolithography methods to obtain a uniform disk 1.35µm thick.

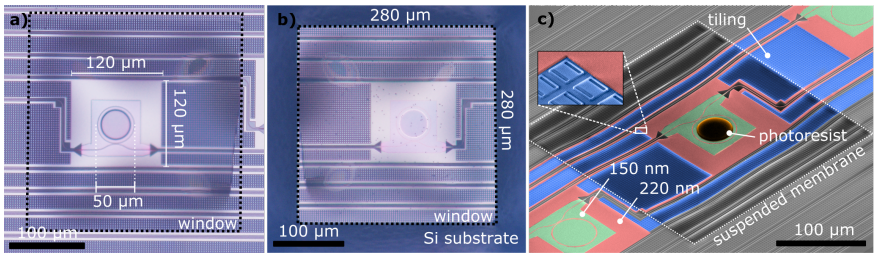

*Figure 5.12: (a) Microscope image of suspended ring resonator with R=25*µm *and 1.35* µm *thick AZ5214 photoresist patterned in the annular region. (b) Backside image of the same device shows that a* $280 \times 280 \mu m^2$ *window was opened in the silicon substrate. The dark blue regions are the sidewalls of the anisotropically etched silicon substrate. (c) The various regions are indicated by partially coloring the tilted (52°) SEM image. The inset shows a detail of the tiling.*

To increase the effective thermal resistance of the MRRs, windows were opened on the backside of the chip in the silicon substrate by anisotropic etching in a KOH-solution. The PICs were first thinned down from 700 µm to 150 µm thickness and consecutively polished. A SiN/SiO_x (400/500 nm) thick rectangular hard mask was patterned on the backside of the samples. The samples were etched in a KOH-solution (80°C/ 20% concentration) for 180 minutes. A specially designed teflon holder prevents the etchant from reaching the top device layer. The top device layer was additionally protected by using a photoresist layer to prevent spurious KOH-leakage from damaging the top surface. The opened windows are 280 µm wide with an unintentional slight offset of $\sim$ 25 µm from the center of the ring resonators, as seen in Figure 5.12.

After substrate removal, the front side protection layer is removed in O_2 plasma and a 1.35 µm thick disk of AZ5214 is lithographically patterned on top of the suspended membrane resonators inside the annular region with a radius of 21 µm.

5.9.2 Infrared reflection absorption spectroscopy

To evaluate and benchmark the photothermal spectroscopic method, the absorption spectrum of the analyte was evaluated using Infrared Reflection Absorption Spectroscopy (IRRAS). This is a popular spectroscopic method that can accurately characterize thin polymer films on metals. It is quite challenging to quantitatively characterize the absorption spectrum of a thin film in transmission due to Fabry-Perot-like interference fringes when measured in transmission. Any transparent substrate will add additional inter-

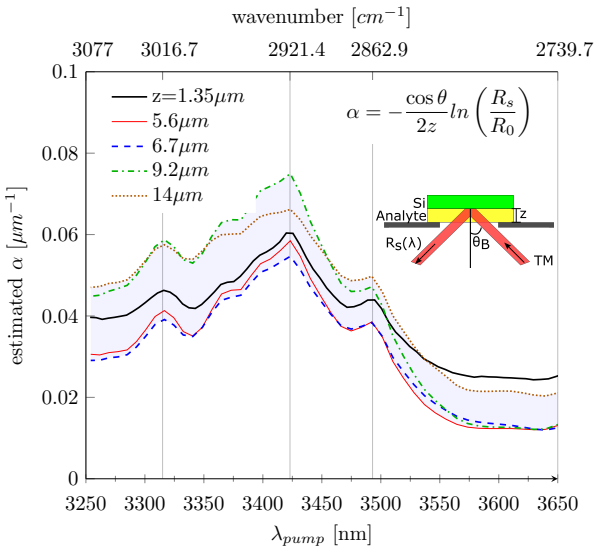

*Figure 5.13: Measured FTIR transflectance absorption spectrum of AZ5214 photoresist (z=1.35*µm*) and AZ9260 (z={5.6,6.7,9.2,14}*µm*). The absorption is estimated by comparing the reflectance spectrum of the analyte to reflectance spectrum of silicon, formula in the inset of the figure. Measurements are performed under the Brewster angle (58 degrees) and TM polarization to eliminate fringes of the transflectance spectrum.*

faces leading to more interference effects and increased background signal which are difficult to decouple from the analyte with a simple reference measurement. To circumvent this, IRRAS is applied where the analyte (on a reflective substrate) is measured in reflection under the Brewster angle with TM polarized light. In this configuration, the specular reflection from the air/polymer interface is eliminated such that only the beam reflected off of the reflecting substrate (e.g. silicon or gold) is collected. The sample is therefore measured in so-called transflectance mode [49, 50]; the light effectively traverses the sample twice with minimal fringe interference effects[10], see also the inset of Figure 5.13. This was evaluated for the mock-up analyte using a FTIR spectrometer. The incidence angle was adjusted using the Veemax accesory from Pike to the Brewster angle of 58 degrees for the polymer/air interface. A ZnSe wire grid polarizer is used to obtain TM polarization. Different positive photoresists were spincoated onto silicon wafers with different thicknesses. The absorption spectrum is estimated by

[10]The silicon-air interface on top of the chip does not produce a significant fringe etalon. The FSR of this thicker film (700 µm) etalon is lower than the FTIR resolution and the beam coming from the top surface is partially blocked by the aperture.

assuming the Beer-Lambert law and comparing the reflectance spectrum $R_s(\lambda)$ to the reflectance $R_0(\lambda)$ of a plain silicon wafer under identical conditions.

$$\alpha = -\frac{\cos\theta_B}{2z} \ln \frac{R_s}{R_0} \tag{5.52}$$

The absorption coefficient α is on the order of 500cm^{-1}. There is some spread ($\pm 0.01\mu\text{m}^{-1}$) on the absolute value of the absorption spectrum among the four samples due to measurement variability and the limitations of the Beer-Lambert law for optically thick samples $z = 9.2, 14\mu m$ where optical saturation can occur, giving rise to a non-linear relationship between the absorbance and path length [51]. For the photothermal experiments, a thinner ($1.35\mu m$) version photoresist AZ5214 was used.

5.9.3 Experimental setup

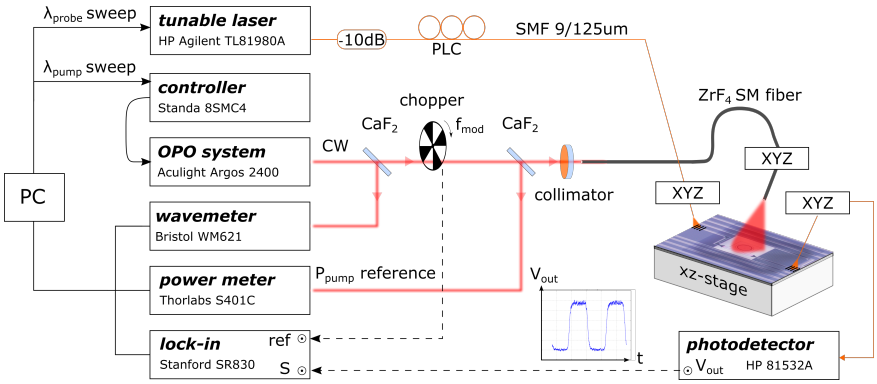

Figure 5.14: Schematic of the photothermal spectroscopy measurement setup. A tunable near-infrared laser source at 1550 nm is vertically coupled to the ring resonator after passing a 10dB attenuator and a polarization controller. The operating wavelength λ_{probe} is set at the point with the highest slope $\mathcal{T}'$ of the MRR spectrum. A free-space modulated tunable mid-infrared source (OPO) is step-scanned across the absorption spectrum 3250-3600 nm. At each λ_{pump}, the generated heat is transduced to a change in NIR probe power ΔP_{probe} which is read-out using a lock-in amplifier at the modulation frequency. A fraction of the OPO power P_{pump} is monitored with a free-space splitter (details not shown for clarity) while the OPO wavelength is monitored by a wavemeter.

The measurement setup is schematically shown in Figure 5.14. An Optical Parametric Oscillator (OPO) system from Aculight was used as the mid-infrared pump source. The mid-infrared emission wavelength is swept by adjusting the intra-cavity etalon angle and the position of the periodically poled Lithium Niobate (PPLN) crystal. The wavelength tuning of

the module has been automated in-house with a stepper motor, more details about the automation of the wavelength tuning process can be found here [52]. The OPO light is focused into a ZrF_4 single mode fiber using a fixed focus collimator. The output fiber end is cleaved and positioned $\sim 160\mu m$ above the ring resonator. The mode field diameter of the SM fiber is about $15\mu m$ at 3.3µm. The tunable probe laser Agilent TL81980A is vertically coupled to the chip. The input power is attenuated by 10 dB in order to avoid nonlinear effects in the high Q ring resonator device. The on-chip probe power is estimated to be around -23 dBm. A polarization controller is used to ensure that TE-polarized light is coupled to the chip. The analog output of the probe power meter HP81532A is coupled to a Stanford SR830 lock-in amplifier.
The mid-infrared pump wavelength is tuned from $3.25\mu m$ to $3.6\mu m$. Two different devices were measured with different parameters and resolution $\Delta\lambda_{pump}$, as seen in Figure 5.15 and table 5.1. The lock-in amplifier records 10 consecutive data points for each λ_{pump} using an integration time of 100 ms and a filter slope of 18dB/oct. The modulation frequency is 300 Hz. The reference power levels are collected simultaneously. The reported variation of the Mode-Field Diameter (MFD) of the SM mid-infrared fiber in the measured wavelength range is taken into account for the calculation of f [53]. The resulting function f increases ∼20% in absolute value from 3250 nm to 3600 nm. Typical parameters used for the experiment are listed in table 5.1.

5.10 Results and discussion

Figure 5.15 shows the measured photothermal spectrum with the absorption spectrum calculated using equations 5.10 and 5.6 and the comparison with the FTIR spectrum. The peak positions (3016.7, 2921.4 and 2862.9 cm^{-1}) corresponding to the aliphatic C−H stretching vibration frequencies agree well with the results obtained from IRRAS [54].
The magnitude of the measured absorption coefficient also corresponds quite well with the IRRAS results. Figure 5.15 also shows that two different devices measured under different conditions produce the same absorption spectrum by normalizing the signal to the measurable quantities in table 5.1. This shows that as long as the position of the pump fiber to the chip is reasonably known and controlled, the variability of on-chip devices (e.g. Q-factor) can be accounted for. An estimate of the error on the parameters used for the calculation of the absorption is given in table 5.1. A safe value of 10% was assumed for the fitting algorithm to retrieve the Q-factor and derivative from the measurement. By considering the worst case scenario

parameter	I	II	error	unit
$P_{probe,max}{}^{a}$	-32.3	-28.8	0.1	dBm
$\lvert d\mathcal{T}/d\lambda\rvert_{max}{}^{b}$	122	63	10%	nm^{-1}
Q^{b}	166k	77k	10%	
$\lambda_{res}{}^{a}$	1550.076	1549.232	0.001	nm
$P_{pump}(2921.4cm^{-1})^{a}$	0.45	0.35	0.04	mW
$\Delta T(2921.4cm^{-1})$	11.0	9.8	20 %	mK
$\alpha(2921.4cm^{-1})$	745.2	646.6	25 %	cm^{-1}
$f[R_{ring},$ $\omega(2921.4cm^{-1}, 100\mu m)]^{c}$	0.86	0.64	10 %	
$R_{th}{}^{c}$	142	273	1%	K/W
R_{ring}	35	25		µm
resolution	5	20		nm
total time	35	10		min
z	160		10	µm
G	10^6			V/W
$n_g{}^{b}$	3.71		5%	
$\partial n/\partial T$	7.6 $\times 10^{-4}$			K^{-1}
L_{eff}	2.8		0.01	µm
integration time	100			ms
f_{mod}	300			Hz

[a] measured directly; [b] fit from measurements; [c] from simulation;

Table 5.1: Parameters used to calculate the photothermal absorption spectrum and some typical values for the two measurements from Figure 5.15. An error estimate is given where applicable.

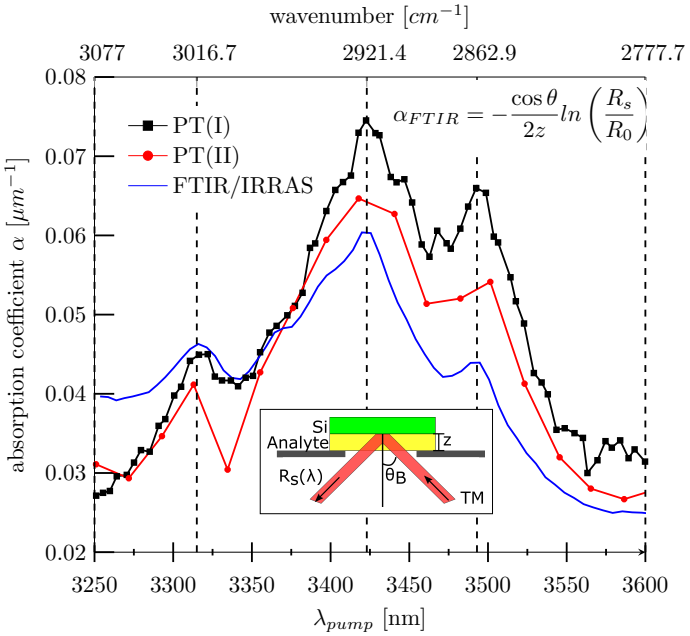

Figure 5.15: Comparison of the absorption spectrum of the photoresist AZ5214 recovered by the photothermal method (PT) for two different devices under different measurement conditions I and II (see table 5.1) to the absorption spectrum measured with the FTIR. The PT absorption coefficient is estimated using equations 5.10 and 5.6. For the FTIR measurement, the inset shows that the absorption coefficient α_{FTIR} is estimated by comparing the reflectance spectrum of the analyte to the reflectance spectrum of silicon (see formula in graph). Measurements are performed under the Brewster angle (58 degrees) and TM polarization to eliminate fringes of the transflectance spectrum.

for the error addition in the calculation, it is estimated that α at 2921 cm^{-1} for experiment II in Figure 5.15 lies within the extreme bounds of 500-870 cm^{-1}.

Even after taking the beam waist wavelength dependency into account, there are minor discrepancies in the relative peak heights of the photothermally recovered spectrum and the FTIR spectrum. This is due to the fact that the photothermal technique probes the non-radiative absorption directly whereas the FTIR technique is influenced by optical scattering effects [1]. It is well known that optical scattering is stronger for shorter wavelengths and this could explain why the FTIR technique overestimates the nonradiative absorption at shorter wavelengths.
The device acts as a wavelength-selective bolometer for the mid-infrared

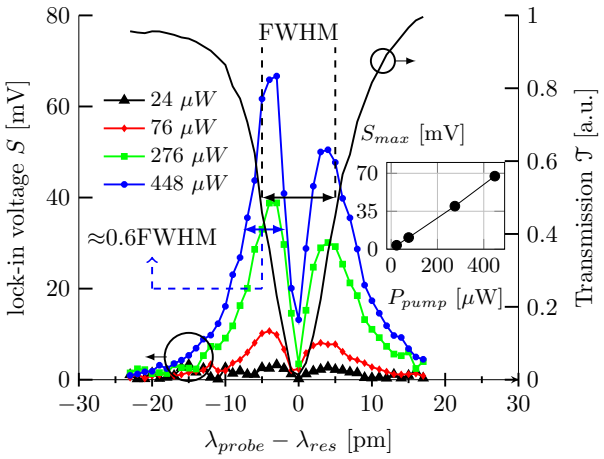

Figure 5.16: Photothermal signal on the lock-in amplifier for increasing P_{pump} corresponding to measurement I in Figure 5.15 at $\lambda_{pump} = 2921.4cm^{-1}$. P_{pump} is the power exiting the mid-infrared fiber facet towards the resonator. The device can be viewed as a thermal detector for the mid-infrared source with a sensitivity S/P_{pump} of 150 V/W for $P_{probe} \approx 1.6\mu W$. The FWHM of the optical resonator is 10 pm. The FWHM of the photothermal signal is $\approx 0.6\times$ smaller.

source. The sensitivity S_{max}/P_{pump} is estimated in Figure 5.16 and equals 150 V/W at the peak absorption wavelength of the polymer of $2921.4cm^{-1}$ with $\alpha_{2921.4cm^{-1}} \approx 750cm^{-1}$ for a non-suspended resonator. The probe power $P_{probe,max}$ for the measurement is 1.6 µW. Further improvements can be achieved by thermally isolating the ring resonators.
In the current setup, the measurement time is on the order of 10 minutes. The scanning time of the experiments can be greatly reduced by considering a different mid-infrared source and reducing the measured wavelength range. An External Cavity-Quantum Cascade Laser (EC-QCL) can be used which can achieve kHz scanning rates in a $\sim$ 7 cm^{-1} wavelength range or 20-40 Hz rates in a $\approx$ 100-150 cm^{-1} wavelength range [55, 56].

5.10.1 Thermal isolation

Thermal isolation of the ring resonators can greatly increase the photothermal signal response. Thermal steady-state FEM simulations were performed using *COMSOL*. The effective thermal resistance R_{th} was estimated by calculating the average temperature increase in the ring waveguide for a given power dissipation.
In Figure 5.17, the results of a 3D axial symmetrical model are given with the axis of symmetry in the center of the ring and normal to the surface. As

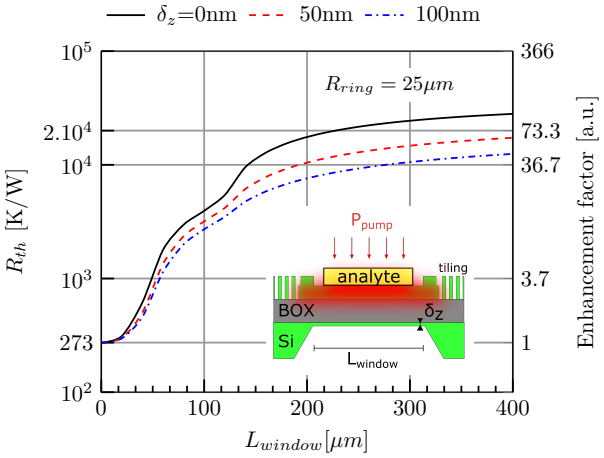

Figure 5.17: 3D-axial symmetrical FEM simulation of the effective thermal resistance of suspended ring resonators. The expected increase in thermal resistance R_{th} for a window of $280 \times 280\mu m^2$ is on the order of $\times 100$. A thin, sub-micron thick δ_z remaining silicon slab on the backside of the membrane can significantly reduce the isolation factor. The influence of the tiling (indicated in blue in Figure 5.12 (c)) has been accounted for by adding concentric Si rings with a period of 3µm and 70% fill factor on top of the BOX. The value for $L_{window} = 0$ corresponds to experiment I in Figure 5.15

seen in the microscope and SEM images in Figure 5.12, the top silicon slab is only continuous in a square $120 \times 120\mu m^2$ area. Beyond this slab, the top layer is filled with tiling, which thermally disconnects the top silicon layer. This tiling layer is included in the simulation by adding a periodically etched slab beyond the $60\mu m$ radius with a period of 3 µm and a fill factor of 70%, hereby modeling the tiling as concentric rings. From Figure 5.17 it is clear that care has to be taken that the silicon substrate is etched completely up to the BOX for maximum effectiveness. The heat dissipation to the silicon substrate is the dominant heat loss mechanism. From the microscope and SEM images in Figure 5.12, one should also consider that (a) the opened window is unintentionally shifted by $25\mu m$ with respect to the center of the ring and (b) the ring resonator area is thermally connected to the rest of the silicon slab on the device layer by $\approx 5\mu m$ wide strips along the access waveguides, which contribute to the heat spreading to the sides (indicated in red in Figure 5.12(c)). Full 3D simulations (without the tiling layer) indicate a decrease of the enhancement factor by 10% to account for (a) and an additional 20% decrease to account for (b). For $L_{window} = 280\mu m$, the expected enhancement factor from Figure 5.17 is corrected to ≈ 57 for better correspondence with the structure depicted in Figure 5.12.

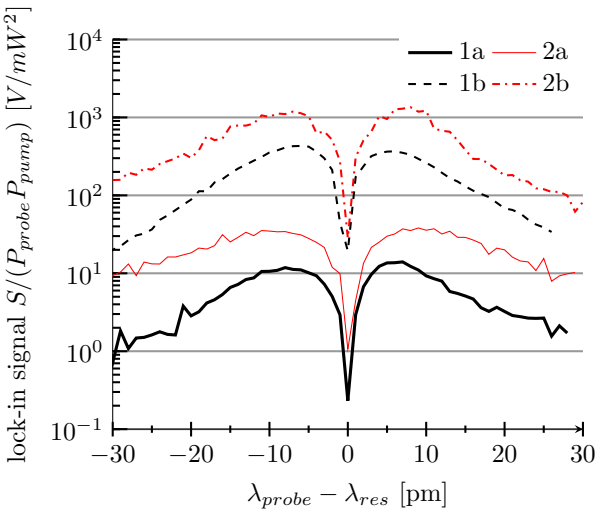

Figure 5.18: Normalized photothermal signal modulation S of 1.35μm thick AZ5214 photoresist at $\lambda_{pump} = 3419nm(2925cm^{-1})$ for (a) supported and (b) suspended ring resonators. Two different ring resonators were compared. The maximum photothermal signal is enhanced by more than 10 dB in both cases.

device	1	2
$\mathcal{T}_{probe,B}/\mathcal{T}_{probe,A}$	1.014	1.445
$\left\|\frac{d\mathcal{T}}{d\lambda}\right\|_{max,B} / \left\|\frac{d\mathcal{T}}{d\lambda}\right\|_{max,A}$	0.72	1.0
$[S_{max}/P_{probe}P_{pump}]_B \,/\, [S_{max}/P_{probe}P_{pump}]_A$	30.8	34.5
$R_{th,B}/R_{th,A}$	43.1	34.5

Table 5.2: Performance comparison of suspended (B) resonators to supported ones (A). Quantities are expressed as ratios (B/A).

The fabricated membrane ring resonators were compared to identical devices on silicon substrate with the same measurement setup. The acquired maximal lock-in signal S for a certain λ_{pump} is normalized to the reference pump power P_{pump} and P_{probe}, see Figure 5.18. In order to evaluate the photothermal enhancement, differences between the maximal slopes of the two ring resonators are taken into account by normalizing the maximal photothermal response to the corresponding maximal slope $|d\mathcal{T}/d\lambda|_{max}$. The performance ratios of the suspended resonators as compared to the supported ones are given in table 5.2. The best measured enhancement factor $E = R_{th,B}/R_{th,A}$ of 43 is slightly lower than what is expected from simulations. FEM simulation suggests that even a very thin remaining layer of

100 nm can halve the thermal resistance enhancement.

5.10.2 Reference power and MRR tracking

In practice one needs to know the exact pump power $P_{pump}(\lambda_{pump})$ at all times during the experiment in order to correctly retrieve the absorption spectrum $\alpha(\lambda_{pump})$. It was noticed that the fiber coupling efficiency varied irregularly as a function of time, and this is believed to be due to a irregular beam quality coming from the output of the OPO due to thermal effects. Therefore a free space beam splitter was built after the coupling to the first collimator, see Figure 5.20(b). In contrast to the free space path before the collimator, the beam is confined to a single mode so that any power splitting beyond this point will provide a consistent power reference, see also Figure 5.19. The free space reference power splitter was placed after the coupling

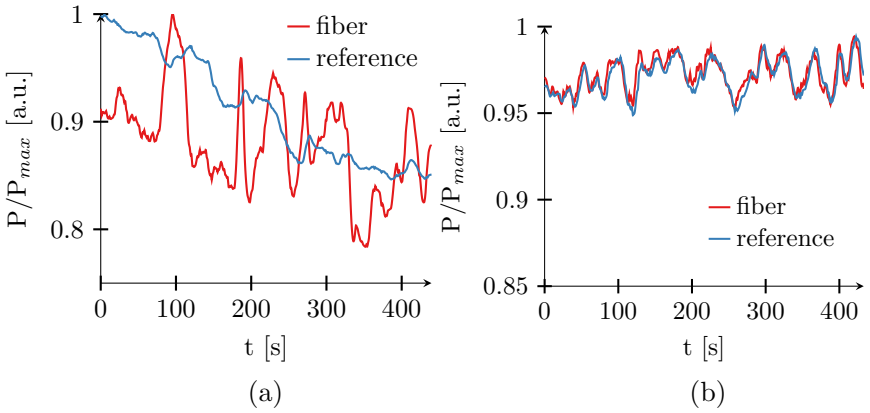

*Figure 5.19: Simultaneous measurement of the normalized reference OPO power, measured with a free space detector, and the power inside the single mode fiber. The fiber coupling efficiency varies with time and cannot be captured adequately with a reference detector in the beampath **before** the collimator (a). A free-space beam splitter was built **after** the first collimator which gives a stable reference power over time (b).*

to the first collimator. A fraction of the OPO power is monitored in free-space using a thermopile detector S401C from Thorlabs. The source power is monitored by splitting the beam using free space optics. The ratio $\chi(\lambda_{pump})$ between the power coming out of the fiber towards the chip $P_{pump}(\lambda_{pump})$ and the reference power $P_{ref}(\lambda_{pump})$ is characterized beforehand. This ratio $\chi(\lambda_{pump})$ is wavelength dependent because of the involved optics. $\chi(\lambda_{pump})$ is shown in Figure 5.20.

$$P_{pump}(\lambda_{pump}) = P_{ref}(\lambda_{pump})\chi(\lambda_{pump}) \tag{5.53}$$

In the experiment, also the slow ambient temperature drift of the MRR

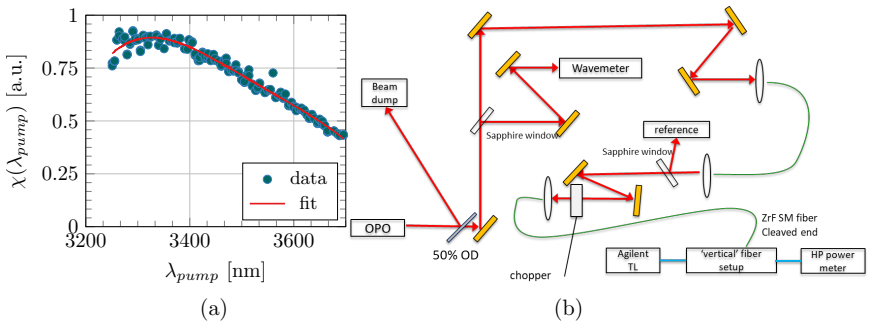

Figure 5.20: Measurement of the ratio between mid-infrared power launched towards the chip and reference power (a). Schematic of the OPO setup showing the free-space beam path and free space splitter after the first single mode collimator (b).

resonance must be tracked. The probe wavelength λ_{probe} is re-optimized at each pump wavelength by searching for the local maximum of the photothermal signal using a step-wise hill-climbing algorithm, see also Figure 5.21. Other, more advanced and faster laser locking feedback loops are possible to implement [57]. This would reduce the total measurement time of the spectrum, but in this experiment the mid-infrared source tuning speed is the limiting factor.

5.10.3 Suspended membranes

The optical properties of the suspended microrings were practically unaltered by the processing as can be seen in Figure 5.22, therefore not affecting the experiment significantly. However, the membrane introduces an interface where the probe light sees a slight change in effective refractive index when passing from the unsuspended region to the membrane. This introduces some additional minor reflection fringes which can be seen in Figure 5.22(a) and in the transmission (2b) in Figure 5.22(b). For more accurate results, the slope of the actual spectral response Figure 5.22, containing the etalon, can be taken into account in the calculation of the absorption coefficient. In future chip designs, care should be taken to enlarge the optical waveguide mode at the membrane transition region to minimize the reflections.

The insertion loss for suspended devices was almost exactly the same as for supported ones. The ratio of the transmitted power under similar measurement conditions shows that the insertion loss of the two chips is almost

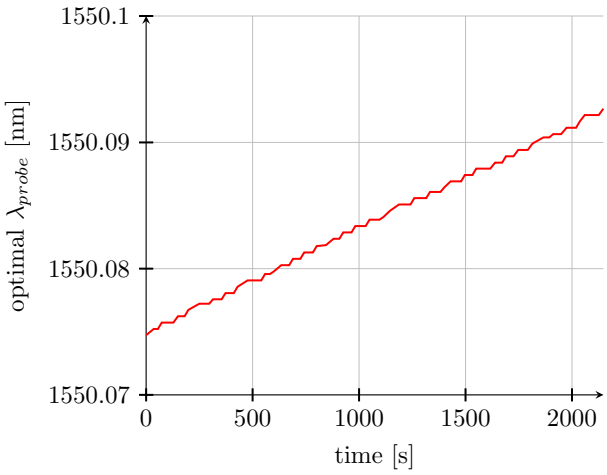

Figure 5.21: Time evolution of the optimal probe wavelength during the measurement of experiment I in Figure 4 in the main text. The slow ambient temperature change pushes the ring resonance towards longer wavelengths. The probe wavelength adjustments are on the order of 1-2 pm every 40s.

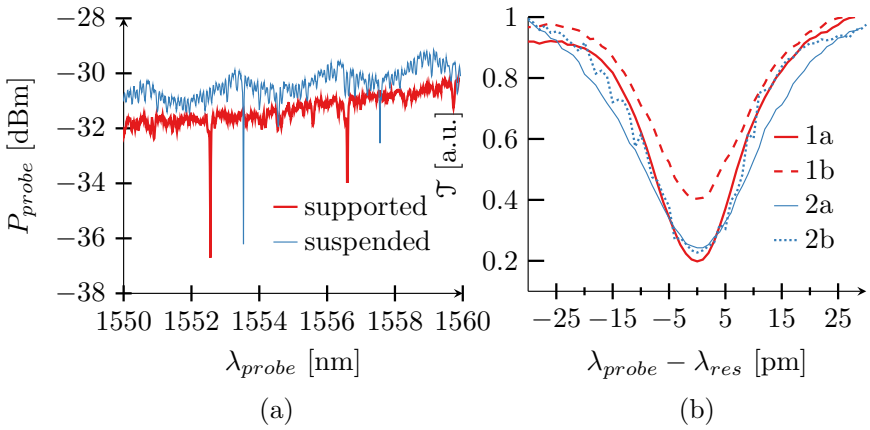

Figure 5.22: Probe transmission of the same microring resonator on a die where the ring has been suspended as opposed to one where the chip is not processed (a). Minor fringes can be observed in the suspended case. Zoom-in on the resonances of two different rings on two separate dies (b). Transmission of MRRs 1 and 2 on a die where the substrate has not been removed (1a,2a) and one where the ring resonators are suspended (2a,2b). Q-factors are around 80k.

identical. The ratio of the Q-factors of the microrings is also similar and is proportional to the ratio of the maximal slopes.

5.10.4 Thermal noise limit

The device can be viewed as a thermal detector or bolometer, where the polymer acts as a 'perfect' absorber. It is interesting to consider the ultimate sensitivity of such a device. The bolometer sensitivity limit can be expressed as the Noise Equivalent optical Power (NEP) which is ultimately governed by the thermal background- or phonon fluctuations of the microstructure itself. This thermal fluctuations are similar in nature to Brownian motion of electrons and cannot be distinguished from absorbed excitation light. It can be shown that the NEP is limited by the effective thermal resistance and temperature, analogous to electronic resistor (Johnson) noise [58].

$$NEP_{phonon}/\sqrt{BW} = \sqrt{4k_B/R_{th}}T \tag{5.54}$$

with k_B the Boltzmann constant. At room temperature, the NEP is about 15 pW/Hz$^{0.5}$ for $R_{th} = 2\times10^4$ K/W, using the estimated thermal resistance of the fabricated membranes. In order to reach helium-cooled bolometer performance of $\approx$ 10 fw/Hz$^{0.5}$, used for terahertz detectors, the thermal isolation needs to be increased to $R_{th} = 10^9$ K/W. This isolation increase is challenging to achieve, but there are indications that this is possible through careful engineering [58].

5.10.5 Mechanical stability

The suspended structures did not break nor crack during the handling and experiments. Although no standardized mechanical stability tests were performed on the devices, it is estimated through FEM simulation that the device membranes can withstand a mechanical shock that corresponds to a level 10 severity threshold according to the American National Standard S2.62-2009 which corresponds to an inelastic free fall from a height of 5 m [59], see also Figure 5.23. This should be sufficient for all practical applications of the transducer.
The standard shock test is simulated in the time-domain in COMSOL by applying a half-sine wave acceleration with a duration of 30 ms and 53g peak acceleration to the fixed membrane. The acceleration is normal to the membrane in vacuum. The values emulate a free fall inelastic drop from a height of approximately 5 m. The transient response yields a maximal principal stress value of 0.9 MPa at the edges of the interface where the silicon substrate has been removed. The limiting factor is the tensile strength of the Buried Oxide (BOX) layer, which is around 100 MPa. It can be seen that the membrane stress response follows the half-sine wave closely, the membrane experiences the shock pulse as a quasi-static load. This is

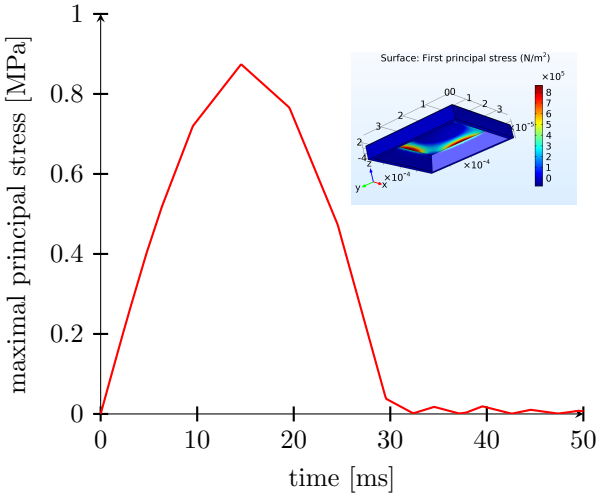

Figure 5.23: Time-domain FEM simulation of maximal stress developed in the $280 \times 280 \mu m^2$ fixed membrane during a half-sine acceleration shock time-function. The duration of the applied load is 30ms with a 53g peak acceleration. This load corresponds to a free fall drop from about 5m.

because the first natural period of the membrane is much smaller than the pulse duration.

5.10.6 Limit of Detection

The LOD is evaluated for the thermally isolated device (1b), as shown in Figure 5.12 and whose measurement results were previously shown in Figure 5.18. The RMS deviation of the lock-in signal S (as defined in equation 5.10) at the optimal probe position is $0.49mV$ for a 100 ms integration time, $P_{probe,max} = 0.5\mu W$ and gain $G = 10^6 V/W$. This corresponds to a minimal detectable change in probe transmission of $\Delta\mathcal{T}_{probe} = 5 \times 10^{-4}$, which is a reasonable estimate for lock-in type detection schemes. Given the increased thermal resistance of approximately $R_{th} \sim 1.2 \times 10^4 K/W$ this leads to an estimated normalized noise equivalent absorption coefficient (NNEA=$\alpha_{min} P_{pump}/\sqrt{\Delta f}$) of $7.6 \times 10^{-6} cm^{-1} W/Hz^{1/2}$ for $P_{probe,max} = 0.5\mu W$. The on-chip probe power cannot be chosen too large as the thermal non-linear effects would affect the response of the ring resonator. With a fiber power P_{pump} of 50 mW, $P_{probe,on-chip} = 0.5$ µW and 1 Hz measurement bandwidth, a minimal detectable absorption coefficient α_{min} of $1.5 \times 10^{-4} cm^{-1}$ is predicted.
Typical absorption values of trace gases in the 3-4µm wavelength region are

of the order of 30 cm^{-1} at 1 atm and room temperature [60]. Even without assuming gas pre-concentration inside the coating, this gives a LOD estimate of $c_{min} = 5ppm$. To compare with TDLAS systems, this corresponds to an PT enhancement factor E_{PTS} on the order of 10^4. The performance in terms of NNEA (with $E_c = 1$) reported here is modest compared to state-of-the-art minuaturized optical sensors such as some QEPAS examples where NNEA values as low as $10^{-10}cm^{-1}W/Hz^{1/2}$ have been shown [61, 62]. However the proposed transducer shows that non-contact all-optical interrogation is possible which can be a key requirement in certain applications, e.g. sensors incorporated in food packages. Additionally, the next step is to coat the MRRs with a gas-adsorbing porous coating with pre-concentration factors $>10^4$ [34, 38, 63], which would boost the enhancement factor for sub-ppm trace gas sensing applications.

5.11 Photothermal spectroscopy of toluene

From the previously described coatings, the mesoporous and spherosilicate coatings developed at COK, KULeuven were not suitable for PT spectroscopy. For the mesoporous (Al) silicate coatings, cross-contamination with water in the pores is believed to be the main reason why no trace gas signal could be discerned from the background. The hydrophobic spherosilicates on the other hand have higher inherent background signal due to their structure. Combined with the relative lower enrichment factor, they did not produce any meaningful PT signal.
Results for toluene in gas and liquid phase were obtained by using a mesoporous coating developen at TUWien. It was shown that the HMDS water repellant layer was essential in order to obtain meaningful results.

Experimental setup and preliminary results

To test the PT signal with single mode fibers, the setup from the PoC experiment was adapted to accommodate a gas flow cell. The chip was enclosed in a custom built airtight aluminum enclosure with a thin 0.5mm sapphire optical window which can be mounted on a YZ-stage, see also Figure 5.24. Sapphire was chosen because it is quite rigid even at low thicknesses and is transparent in the VIS- (to align with the camera), NIR- (to interface with the probe beam) and SWIR wavelength range (for the pump beam). The distance from the fiber facets to the chip surface was kept to a minimum, about 0.7-1 mm to reduce the insertion losses. The added insertion loss compared to close contact fiber measurement is about 30 dB for the probe signal and 15 dB for pump signal (due to beam spreading). In a practical application, lens imaging systems could be employed instead with

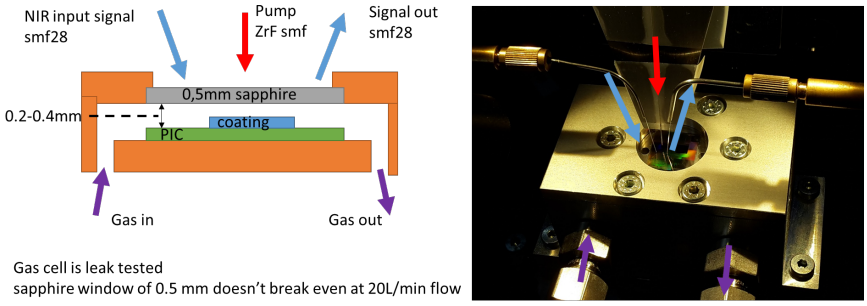

Figure 5.24: Optical gas-cell for trace gas PT experiment. The chip is enclosed in a portable gas flow cell with a thin 0.5mm thick sapphire window for optical interfacing. The fiber to chip distance is less than 1 mm both for the near-IR probe and mid-IR pump.

much higher efficiency. The lenses can be processed even on the Si substrate itself, enabling interaction with the chip through the backside [64].
The gas cell was filled using the gas generator setup from [39] and a toluene bubbler to create a mixture of 1000 ppm-volume toluene in N_2 carrier gas. The photothermal spectra obtained at 3.3μm are shown in Figure 5.25 and normalized to the background in Figure 5.26. Overall, the coating itself absorbs a lot of incident light and there is a large background absorption peak at 3375 nm coming from the coating matrix and HMDS layer. The peak absorption value is estimated to be around 500 cm^{-1} which will obscure any signal coming from the trace gas in that wavelength region. Nonetheless, these preliminary results show that the spectral response of toluene can still be recovered when normalized to the background spectrum. The spectral shift of the peaks is an indication that the toluene molecules inside the pores are in condensed liquid phase. A similar trend was observed both in ATR spectra of the coating and other works from the literature [65], see also Figure 5.27.

From these measurements, it is clear that the background absorption of the coating and the influence of water are two main showstoppers to reach sub-ppm detection. Further investigation is needed whether it is possible to find a suitable coating which is transparent in the SWIR wavelength region of typical trace gases, yet highly hydrophobic to reduce the background signal of water. Another suggestion to mitigate water influence is to embed microheaters in the vicinity of the microring to heat up the coating to a higher temperature. However, this approach requests that the coating response to the analyte at elevated temperature remains largely unchanged. Moreover, the microheaters are metal based and need to be placed such that

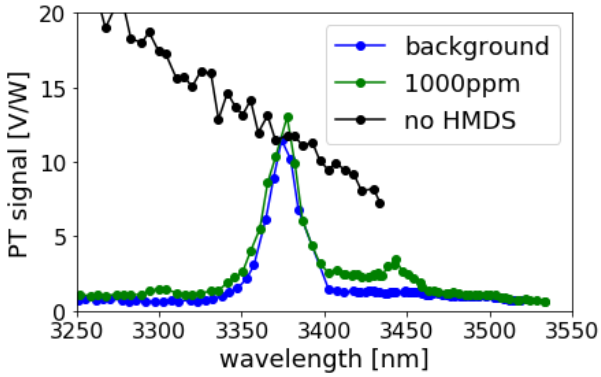

Figure 5.25: Photothermal MRR response with a mesoporous gas coating, augmented with a hydrophobic HMDS layer, exposed to 1000 ppm of toluene gas in nitrogen and the background response (0 ppm toluene). When no hydrophobic HMDS layer is applied, trapped water vapor obscures the signal even when there is no toluene present. The wavelength slope in the water signal is due to the absorption tail, originating from the broad water absorption peak at 3 µm.

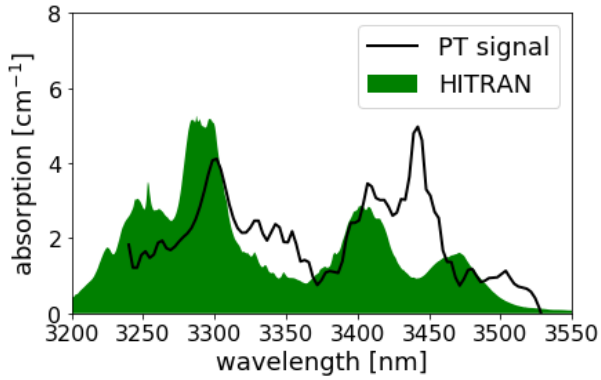

Figure 5.26: The absorption spectrum of toluene (1000ppm) is recovered from the PT signal, normalized to the background response, and compared to the HITRAN values. All relevant absorption peaks of toluene can be recovered. There is a shift towards longer wavelengths as expected when the gas condenses in the pores.

the pump beam is not absorbed by them, to avoid an additional photothermal background signal.

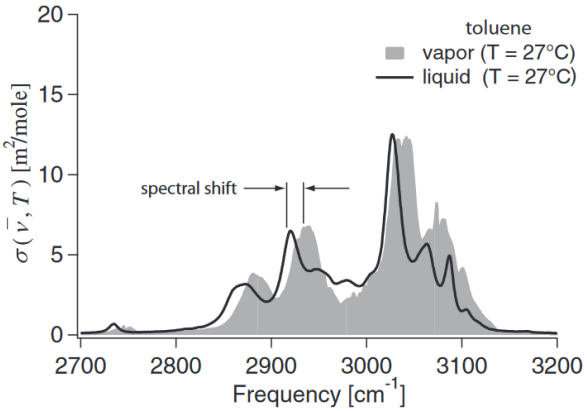

Figure 5.27: The absorption cross-section of toluene in liquid and gas phase. Note that the magnitude is similar for both cases but there is a shift towards longer wavelengths [65].

5.12 Surface Enhanced Infrared Absorption

It is interesting to consider an additional enhancement approach to further increase the photothermal sensitivity which is similar to Surface Enhanced InfraRed Absorption spectroscopy (SEIRA), often used to increase the absorption signal in the visible wavelength range. The techniques relies on coupling the light to *plasmon* modes, electric charge oscillations at the interface between a dielectric and a metal [66, 67]. Plasmons can give rise to a very strong local electric field enhancement around particles, also called Localized Surface Plasmon (LSP) modes. Plasmons can also be guided along the metal interface as a travelling charge-oscillation wave, a mode known as a Surface Plasmon–Polariton (SPP). For many applications, the LSP modes are desirable having a high field enhancement and broadband response. However, one needs to take some special design considerations into account in the mid-infrared wavelength region.

Most common metals such as gold and silver, have a strongly negative real part of the dielectric constant at mid-infrared frequencies, such that the electric field inside the plasmonic particle is vanishingly small. This inhibits the existence of LSP modes [67]. To achieve broadband field enhancement, non-traditional metals such as graphene or 'designer' metals, such as doped semiconductors and indium-tin-oxides (ITO) must be used instead. Using traditional metals such as gold, it is still possible to design antenna-like plasmonic structures that will exhibit high field enhancement in a narrow wavelength range. The field intensity enhancement in the gas-region are

expected to be on the order of ×10-100 [68]. However for the photothermal case, the challenge remains to design and pattern the metal structures such that the dielectric substrate does not produce an increased background signal due to heating.

5.13 Conclusions

An integrated mid-IR photothermal spectroscopic sensor using suspended SOI microring resonators was demonstrated. The transducer circumvents the need of using a mid-infrared detector by transducing the heat generated through optical absorption to a cheaper near-infrared read-out system. The sensor was used to recover the absorption spectrum of the photoresist AZ5214 in the $3.25 - 3.6\mu m$ wavelength range in good agreement with benchmark FTIR techniques.
The photothermal signal can be increased through engineering the PIC so as to thermally isolate the ring waveguide. The resulting effective thermal resistance is estimated to be $1.2 \times 10^4 K/W$. The latter results in a NNEA of $7.6 \times 10^{-6} cm^{-1} W/Hz^{1/2}$ for 0.5 µW of probe power. By using a pump power of 50 mW and 1s integration time, a LOD α_{min} of $1.5 \times 10^{-4} cm^{-1}$ is predicted. This suggests that sub-ppm integrated trace gas detection is possible using this method. For real-life applications, it would be advisable to select a narrower tuning wavelength range of ≈ 100-150 cm^{-1} to target only a limited number of absorbing species. This way, a more compact, faster and relatively cheaper mid-infrared source can be used such as an external cavity (EC)-QCL compared to the OPO.

A gas-adsorbing mesoporous silica coating was coated on the ring transducers. Sub-ppm LOD values were expected for trace gases such as toluene in the $3-4\mu m$ wavelength range. However the current sensitivity is severely limited by the background optical absorption of the coating matrix and the hydrophobic layer. The latter is essential, as without it, water absorption signal obscures the analyte's response completely. Further investigation is needed to engineer a coating which is transparent in the SWIR wavelength range while still being highly hydrophobic.
The PTS sensing approach described here is specifically relevant for applications where all-optical non-contact trace gas detection is required. For example, the disposable and cheap SOI ring resonator transducer can be embedded inside a food package, whereas the read-out unit containing the tunable probe and pump sources are positioned at some distance above the package. This photothermal spectroscopy approach would then allow for a selective and sensitive way of detecting trace gases without the requirement

of using a cooled mid-infrared detector.

References

[1] Stephen Bialkowski. *Photothermal spectroscopy methods for chemical analysis*, volume 134. John Wiley & Sons, 1996.

[2] Alexander Graham Bell. *The photophone.* Science, 1(11):130–134, 1880.

[3] Yuechuan Lin, Wei Jin, Fan Yang, Jun Ma, Chao Wang, Hoi Lut Ho, and Yang Liu. *Pulsed photothermal interferometry for spectroscopic gas detection with hollow-core optical fibre.* Scientific reports, 6:39410, 2016.

[4] Johannes P Waclawek, Christian Kristament, Harald Moser, and Bernhard Lendl. *Balanced-detection interferometric cavity-assisted photothermal spectroscopy.* Optics express, 27(9):12183–12195, 2019.

[5] Teemu Tomberg, Markku Vainio, Tuomas Hieta, and Lauri Halonen. *Sub-parts-per-trillion level sensitivity in trace gas detection by cantilever-enhanced photo-acoustic spectroscopy.* Scientific reports, 8(1):1–7, 2018.

[6] Hongpeng Wu, Lei Dong, Xukun Yin, Angelo Sampaolo, Pietro Patimisco, Weiguang Ma, Lei Zhang, Wangbao Yin, Liantuan Xiao, Vincenzo Spagnolo, et al. *Atmospheric CH4 measurement near a landfill using an ICL-based QEPAS sensor with VT relaxation self-calibration.* Sensors and Actuators B: Chemical, 297:126753, 2019.

[7] MB Pushkarsky, ME Webber, and CKN Patel. *Ultra-sensitive ambient ammonia detection using CO2-laser-based photoacoustic spectroscopy.* Appl. Phys. B, 77(4):381–385, 2003.

[8] Yang Dong, Mingsi Gu, Gongdong Zhu, Tu Tan, Kun Liu, and Xiaoming Gao. *Fully Integrated Photoacoustic NO2 Sensor for Sub-ppb Level Measurement.* Sensors, 20(5):1270, 2020.

[9] Zhenfeng Gong, Ke Chen, Yewei Chen, Liang Mei, and Qingxu Yu. *Integration of T-type half-open photoacoustic cell and fiber-optic acoustic sensor for trace gas detection.* Optics express, 27(13):18222–18231, 2019.

[10] Pietro Patimisco, Angelo Sampaolo, Huadan Zheng, Lei Dong, Frank K Tittel, and Vincenzo Spagnolo. *Quartz–enhanced photoacoustic spectrophones exploiting custom tuning forks: a review.* Advances in Physics: X, 2(1):169–187, 2017.

[11] Yufei Ma, Shunda Qiao, Pietro Patimisco, Angelo Sampaolo, Yao Wang, Frank K Tittel, and Vincenzo Spagnolo. *In-plane quartz-enhanced photoacoustic spectroscopy.* Applied Physics Letters, 116(6):061101, 2020.

[12] Stefano Dello Russo, Sheng Zou, Andrea Zifarelli, Pietro Patimisco, Angelo Sampaolo, Marilena Giglio, Davide Iannuzzi, and Vincenzo Spagnolo. *Photoacoustic spectroscopy for gas sensing: a comparison between piezoelectric and interferometric readout in custom quartz tuning forks.* Photoacoustics, page 100155, 2020.

[13] Arthur Sedlacek and Jeonghoon Lee. *Photothermal interferometric aerosol absorption spectrometry.* Aerosol Science and Technology, 41(12):1089–1101, 2007.

[14] N J_ Dovichi and JM Harris. *Laser induced thermal lens effect for calorimetric trace analysis.* Analytical Chemistry, 51(6):728–731, 1979.

[15] Wim Bogaerts, Peter De Heyn, Thomas Van Vaerenbergh, Katrien De Vos, Shankar Kumar Selvaraja, Tom Claes, Pieter Dumon, Peter Bienstman, Dries Van Thourhout, and Roel Baets. *Silicon microring resonators.* Laser Photonics Rev., 6(1):47–73, 2012.

[16] John Heebner, Rohit Grover, Tarek Ibrahim, and Tarek A Ibrahim. *Optical microresonators: theory, fabrication, and applications*, volume 138. Springer Science & Business Media, 2008.

[17] Steven A Miller, Mengjie Yu, Xingchen Ji, Austin G Griffith, Jaime Cardenas, Alexander L Gaeta, and Michal Lipson. *Low-loss silicon platform for broadband mid-infrared photonics.* Optica, 4(7):707–712, 2017.

[18] Shankar Kumar Selvaraja, Patrick Jaenen, Wim Bogaerts, Dries Van Thourhout, Pieter Dumon, and Roel Baets. *Fabrication of photonic wire and crystal circuits in silicon-on-insulator using 193-nm optical lithography.* Journal of Lightwave Technology, 27(18):4076–4083, 2009.

[19] Wim Bogaerts and Shankar Kumar Selvaraja. *Compact single-mode silicon hybrid rib/strip waveguide with adiabatic bends.* IEEE Photonics Journal, 3(3):422–432, 2011.

[20] Chung-Yen Chao and L Jay Guo. *Biochemical sensors based on polymer microrings with sharp asymmetrical resonance.* Applied Physics Letters, 83(8):1527–1529, 2003.

[21] Ting Hu, Ping Yu, Chen Qiu, Huiye Qiu, Fan Wang, Mei Yang, Xiaoqing Jiang, Hui Yu, and Jianyi Yang. *Tunable Fano resonances based on two-beam interference in microring resonator.* Applied physics letters, 102(1):011112, 2013.

[22] Weifeng Zhang, Wangzhe Li, and Jianping Yao. *Optically tunable Fano resonance in a grating-based Fabry–Perot cavity-coupled microring resonator on a silicon chip.* Optics letters, 41(11):2474–2477, 2016.

[23] Zhengrui Tu, Dingshan Gao, Meiling Zhang, and Daming Zhang. *High-sensitivity complex refractive index sensing based on Fano resonance in the subwavelength grating waveguide micro-ring resonator.* Optics express, 25(17):20911–20922, 2017.

[24] Mikhail F Limonov, Mikhail V Rybin, Alexander N Poddubny, and Yuri S Kivshar. *Fano resonances in photonics.* Nature Photonics, 11(9):543, 2017.

[25] Linpeng Gu, Liang Fang, Hanlin Fang, Juntao Li, Jianbang Zheng, Jianlin Zhao, Qiang Zhao, and Xuetao Gan. *Fano resonance lineshapes in a waveguide-microring structure enabled by an air-hole.* arXiv preprint arXiv:1907.02186, 2019.

[26] Anton Vasiliev, Aditya Malik, Muhammad Muneeb, Roel Baets, and Günther Roelkens. *Photothermal mid-infrared spectroscopy using Fano resonances in silicon microring resonators.* In 2016 Conference on Lasers and Electro-Optics (CLEO), pages 1–2. IEEE, 2016.

[27] S. M. Spillane D. K. Armani, T. J. Kippenberg and K. J. Vahala. *Ultra-high-Q toroid microcavity on a chip.* Nature, 421(6926):925 – 928, 2003.

[28] Petr Klan and Jakob Wirz. *Photochemistry of organic compounds: From concepts to practice.* John Wiley & Sons, 2009.

[29] SJ Strickler and Robert A Berg. *Relationship between absorption intensity and fluorescence lifetime of molecules.* The Journal of chemical physics, 37(4):814–822, 1962.

[30] Sean Keuleyan, John Kohler, and Philippe Guyot-Sionnest. *Photoluminescence of mid-infrared HgTe colloidal quantum dots.* The Journal of Physical Chemistry C, 118(5):2749–2753, 2014.

[31] S Schilt, J-P Besson, and Luc Thévenaz. *Near-infrared laser photoacoustic detection of methane: the impact of molecular relaxation.* Applied Physics B, 82(2):319–328, 2006.

[32] Gerard Wysocki, Anatoliy A Kosterev, and Frank K Tittel. *Influence of molecular relaxation dynamics on quartz-enhanced photoacoustic detection of CO 2 at λ= 2 μm.* Applied Physics B, 85(2-3):301–306, 2006.

[33] AA Kosterev, YA Bakhirkin, FK Tittel, S Blaser, Y Bonetti, and L Hvozdara. *Photoacoustic phase shift as a chemically selective spectroscopic parameter.* Applied Physics B, 78(6):673–676, 2004.

[34] Nebiyu A. Yebo, Sreeprasanth Pulinthanathu Sree, Elisabeth Levrau, Christophe Detavernier, Zeger Hens, Johan A. Martens, and Roel Baets. *Selective and reversible ammonia gas detection with nanoporous film functionalized silicon photonic micro-ring resonator.* Opt. Express, 20(11):11855–11862, May 2012.

[35] Derek M Kita, Hongtao Lin, Anu Agarwal, Kathleen Richardson, Igor Luzinov, Tian Gu, and Juejun Hu. *On-chip infrared spectroscopic sensing: redefining the benefits of scaling.* IEEE Journal of Selected Topics in Quantum Electronics, 23(2):340–349, 2016.

[36] Kazuo Sato, Mitsuhiro Shikida, Yoshihiro Matsushima, Takashi Yamashiro, Kazuo Asaumi, Yasuroh Iriye, and Masaharu Yamamoto. *Characterization of orientation-dependent etching properties of single-crystal silicon: effects of KOH concentration.* Sensors and Actuators A: Physical, 64(1):87–93, 1998.

[37] Frédéric Marty, Lionel Rousseau, Bassam Saadany, Bruno Mercier, Olivier Français, Yoshio Mita, and Tarik Bourouina. *Advanced etching of silicon based on deep reactive ion etching for silicon high aspect ratio microstructures and three-dimensional micro-and nanostructures.* Microelectronics journal, 36(7):673–677, 2005.

[38] Nebiyu A. Yebo, Petra Lommens, Zeger Hens, and Roel Baets. *An integrated optic ethanol vapor sensor based on a silicon-on-insulator microring resonator coated with a porous ZnO film.* Opt. Express, 18(11):11859–11866, May 2010.

[39] Nebiyu Yebo. *Silicon Based Integrated Optical Gas Sensing.* PhD thesis, Ghent University, 2012.

[40] Bettina Baumgartner, Jakob Hayden, Andreas Schwaighofer, and Bernhard Lendl. *In Situ IR Spectroscopy of Mesoporous Silica Films for Monitoring Adsorption Processes and Trace Analysis.* ACS Applied Nano Materials, 1(12):7083–7091, 2018.

[41] Brecht Vallaey. *Investigating gas adsorption in thin films by in situ spectroscopic ellipsometry.* PhD thesis, KU Leuven, 2018.

[42] Haolan Zhao, Bettina Baumgartner, Ali Raza, Andre Skirtach, Bernhard Lendl, and Roel Baets. *Multiplex volatile organic compound Raman sensing with nanophotonic slot waveguides functionalized with a mesoporous enrichment layer.* Optics Letters, 45(2):447–450, 2020.

[43] Markus Widenmeyer and Reiner Anwander. *Pore size control of highly ordered mesoporous silica MCM-48.* Chemistry of materials, 14(4):1827–1831, 2002.

[44] M Douglas LeVan and Theodore Vermeulen. *Binary Langmuir and Freundlich isotherms for ideal adsorbed solutions.* The Journal of Physical Chemistry, 85(22):3247–3250, 1981.

[45] Lev D Gelb and KE Gubbins. *Characterization of porous glasses: Simulation models, adsorption isotherms, and the Brunauer- Emmett- Teller analysis method.* Langmuir, 14(8):2097–2111, 1998.

[46] Haolan Zhao, Ali Raza, Bettina Baumgartner, Stéphane Clemmen, Bernhard Lendl, Andre Skirtach, and Roel Baets. *Waveguide-Enhanced Raman Spectroscopy Using a Mesoporous Silica Sorbent Layer for Volatile Organic Compound (VOC) Sensing.* In CLEO: Science and Innovations, pages STh1F–7. Optical Society of America, 2019.

[47] Anton Vasiliev, Aditya Malik, Muhammad Muneeb, Bart Kuyken, Roel Baets, and Gunther Roelkens. *On-chip mid-infrared photothermal spectroscopy using suspended silicon-on-insulator microring resonators.* ACS Sensors, 1(11):1301–1307, 2016.

[48] imec. *Europractice Homepage.* `http://www.europractice-ic.com`. Accessed: 2020-01-07.

[49] James A. De Haseth Peter R. Griffiths and James D. Winefordner. *Fourier Transform Infrared Spectrometry, 2nd Edition.* John Wiley & Sons, 2007.

[50] B.D. Teolis, M.J. Loeffler, U. Raut, M. Fama, and R.A. Baragiola. *Infrared reflectance spectroscopy on thin films: Interference effects.* Icarus, 190(1):274 – 279, 2007.

[51] Thomas G Mayerhöfer and Jürgen Popp. *Beer's Law–Why Absorbance Depends (Almost) Linearly on Concentration.* ChemPhysChem, 20(4):511–515, 2019.

[52] Alexander M. Morrison, Tao Liang, and Gary E. Douberly. *Automation of an Aculight continuous-wave optical parametric oscillator.* Rev. Sci. Instrum., 84(1):013102:1–013102:8, 2013.

[53] Thorlabs. *MIR Single Mode Fluoride Fiber Optic Patch Cables*, 2016.

[54] Peter Larkin. *Infrared and Raman Spectroscopy; Principles and Spectral Interpretation.* Elsevier, 2011.

[55] T Tsai and G Wysocki. *External-cavity quantum cascade lasers with fast wavelength scanning.* Appl. Phys. B, 100(2):243–251, 2010.

[56] G Wysocki, R Lewicki, RF Curl, FK Tittel, L Diehl, F Capasso, M Troccoli, G Hofler, D Bour, and S Corzine. *Widely tunable mode-hop free external cavity quantum cascade lasers for high resolution spectroscopy and chemical sensing.* Appl. Phys. B, 92(3):305–311, 2008.

[57] Kishore Padmaraju, Dylan F Logan, Takashi Shiraishi, Jason J Ackert, Andrew P Knights, and Keren Bergman. *Wavelength locking and thermally stabilizing microring resonators using dithering signals.* Journal of Lightwave Technology, 32(3):505–512, 2013.

[58] Michael R Watts, Michael J Shaw, and Gregory N Nielson. *Microphotonic thermal imaging.* Nature Photonics, 1(11):632–634, 2007.

[59] Brian W Lang. *On the New American National Standard for Shock Testing Equipment.* In Structural Dynamics, Volume 3, pages 955–960. Springer, 2011.

[60] Jerry Workman Jr. *The Handbook of Organic Compounds, Three-Volume Set: NIR, IR, R, and UV-Vis Spectra Featuring Polymers and Surfactants.* Elsevier, 2000.

[61] Pietro Patimisco, Gaetano Scamarcio, Frank K. Tittel, and Vincenzo Spagnolo. *Quartz-Enhanced Photoacoustic Spectroscopy: A Review.* Sensors, 14(4):6165–6206, 2014.

[62] Vincenzo Spagnolo, Pietro Patimisco, Simone Borri, Gaetano Scamarcio, Bruce E Bernacki, and Jason Kriesel. *Part-per-trillion level SF 6 detection using a quartz enhanced photoacoustic spectroscopy-based sensor with single-mode fiber-coupled quantum cascade laser excitation.* Opt. Lett., 37(21):4461–4463, 2012.

[63] Pengcheng Xu, Haitao Yu, and Xinxin Li. *Functionalized mesoporous silica for microgravimetric sensing of trace chemical vapors.* Anal. Chem., 83(9):3448–3454, 2011.

[64] Jeroen Missinne, N Teigell Benéitez, Nivesh Mangal, Jing Zhang, Anton Vasiliev, Joris Van Campenhout, Bradley Snyder, Günther Roelkens, and Geert Van Steenberge. *Alignment-tolerant interfacing of a photonic integrated circuit using back side etched silicon microlenses.* In Silicon Photonics XIV, volume 10923, page 1092304. International Society for Optics and Photonics, 2019.

[65] Jason Morgan Porter. *Laser-based diagnostics for hydrocarbon fuels in the liquid and vapor phases.* PhD thesis, Stanford University, 2010.

[66] Ross Stanley. *Plasmonics in the mid-infrared.* Nature Photonics, 6(7):409–411, 2012.

[67] Stephanie Law, Viktor Podolskiy, and Daniel Wasserman. *Towards nano-scale photonics with micro-scale photons: the opportunities and challenges of mid-infrared plasmonics.* Nanophotonics, 2(2):103–130, 2013.

[68] Daniel Rodrigo, Odeta Limaj, Davide Janner, Dordaneh Etezadi, F Javier García De Abajo, Valerio Pruneri, and Hatice Altug. *Mid-infrared plasmonic biosensing with graphene.* Science, 349(6244):165–168, 2015.

6

Non-Dispersive Spectroscopy for CO_2 leak detection

The *global food industry utilizes Modified Atmosphere Packaging (MAP) to extend the shelf-life of fresh products. The packages are typically filled with very high concentrations of CO_2 (50-100%) to reduce microbial-growth. However, often during transport and handling the package integrity can be comprised leading to a leak of CO_2 to ambient concentrations which dramatically increases the food spoilage rate. There is therefore a need to monitor the package integrity in a cheap and mass producable way. This short chapter presents a simple non-dispersive infrared sensing scheme for leak monitoring.*

Contents

6.1 Introduction

The sensor should only be able to discriminate the concentration inside the package between very high (MAP) and low concentrations (ambient) of CO_2 [1]. For this reason, a very simple, yet cheap and effective integrated sensor can be fabricated using Non-Dispersive Infrared spectroscopy (NDIR) with an optical pathlength interaction of only 1 mm. The proposed sensor is demonstrated in a mock-up package environment and further integration strategies are discussed.

6.2 Non-Dispersive IR spectroscopy

Non-dispersive gas spectroscopy is one of the easiest optical sensing methods available, and for this reason they have been widely commercially successful. In particular CO_2 is notoriously difficult to detect using non-optical (e.g. chemical) sensors, and therefore NDIR opened the path for low-cost mass market applications [2]. All that is needed is a broadband source , such as a micro-light bulb (a filament) which passes through two filters, one covering the absorption band of the analyte gas (signal channel) and the other a non-absorbing region of the spectrum (reference channel). The light then interacts with the gas and is analyzed with a photodetector [2, 3]. The spectral windows of the filter are chosen such that ideally no other gas except for the analyte experiences absorption. The filters are typically directly coated onto a dual-channel packaged detector (e.g. in a TO9-can). Typical filters are shown in Figure 6.1 with the CO_2 absorption spectrum. NDIR of CO_2 relies on the very high absorption coefficient in the mid-infrared wavelength range around 4.2 µm which is on the order of 500 cm^{-1}, hundred times stronger than typical trace gas absorption coefficients in the SWIR (3-4µm wavelength range). Therefore, about 1 mm of optical pathlength is required to detect large swings in CO_2 concentration. Simple broadband light-bulb sources and low-cost thermopile detectors are sufficient. The idea for food-package integrity monitoring is to directly scale down the existing NDIR technology to a disposable silicon MEMS-like unit which can easily be embedded into existing packaging foils. The solution has to be minimally invasive to the packaging process in the food industry.

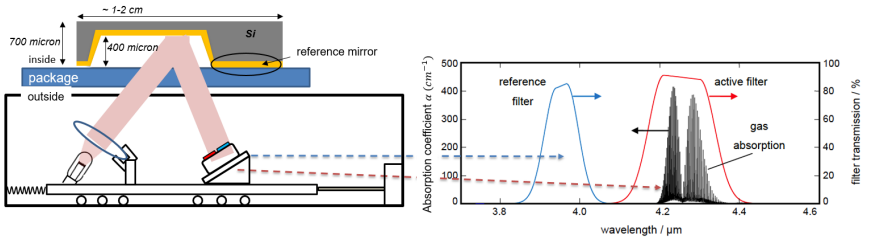

Figure 6.1: Schematic of a minaturized NDIR sensor for CO_2 monitoring inside a food package. The tiny Si structure is embedded on the inside of the package foil which gives the light beam an effective optical pathlength of about 1 mm on the inside. A read-out unit containing the source, detector and NDIR filters collects the signal through the foil. NDIR filter responses for CO_2 adapted from [2].

6.3 Experimental results and discussion

Silicon chips were prepared by patterning the surface with a rectangular mask which is then used to anisotropically (54deg) etch down the silicon along the <111>-plane. The etch-depth was controlled to be around 400-500 µm. A thin 200 nm layer of gold was deposited on the surface to make it highly reflective in the 4.2 µm wavelength region. The final chips have the cross-section as in Figure 6.3. The region which is not etched-down provides a reference measurement signal to compensate for any CO_2 present in the beam-path from source to detector outside of the food-package. The etched region gives an effective optical beam pathlength of about 1 mm through the CO_2-rich MAP of the package.

The etched silicon pieces were placed in a custom built aluminum optical gas chamber, see Figure 6.2. The gas cell accepts standard 1 inch optical elements and a AR-coated window for the MWIR range was used, covering the CO_2 band at 4.3 µm. For the broadband source and detection, a benchtop FTIR was used. In normal operation mode, it was not possible to perform a measurement in reflection. For this purpose, a variable angle specular reflection accessory (Pike Veemax III) was used to couple the light from the FTIR at a small angle θ and collect the reflected beam at the photodetector. A calibrated gas cylinder of 8% CO_2 in N_2 was used to fill the gas cell at a slight overpressure of 1.4 bar. The overpressure is monitored with a barometer to be certain that no leaks occurred during handling and experiment. The FTIR spectrum was recorded for different incident positions of the light beam, see Figure 6.3. When light is incident on the NDIR cavity, higher absorption in the 4.3 µm band is observed. This measurement is compared to a situation when the light hits the reference

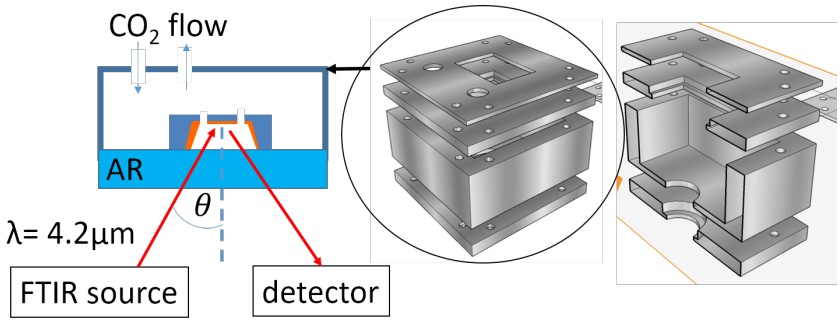

Figure 6.2: A custom optical gas chamber was built to mimic the MAP environment. A 1 inch, 5 mm AR window was used to efficiently couple light in and out of the silicon cavity. The angle of incidence θ of the FTIR beam was controlled using a angle reflection accessory (Veemax III).

mirror on the silicon piece. The ratio of the spectra between the two measurements is a direct measure of the concentration of CO_2 inside the 400 µm cavity. Note that the transmission in the 'reference' case is not unity due to the presence of CO_2 in the beam path of the FTIR system [1]. The ratio of the transmission matches well with the expected 8% (1.4 bar) change by comparing to the absorption coefficients of the HITRAN database [4]. The instrument function of the FTIR (spectral resolution) is taken into account to match the spectral response to the HITRAN database. The response of a 'true' non-dispersive measurement can be inferred from this 'dispersive' FTIR evaluation of the NDIR cavity.

In order for the industry to adapt to new technologies, it is important that the implementation does not interfere with the production chain as much as possible. The food packaging lines are very optimized already and the partners are reluctant to make changes that will affect time and price of the process.

A first integration prototype was tested that encapsulates a silicon piece with injection moulding in a hard plastic, similar to the production process of ground coffee packages. These contain so-called coffee 'valves' that allow air to pass through selectively. The silicon piece in this case is held between two pins of an injection molding device and a few mm of plastic is cast around it, leaving the two areas which were held by the pins open. This 'valve' can then be further thermally or acoustically welded to the 'soft' package foil, see also Figure 6.4. The first prototypes have shown that an

[1] In this experiment, the FTIR is purged with purified, dry air. In this way, the background CO_2 concentration remains constant for the duration of the measurements

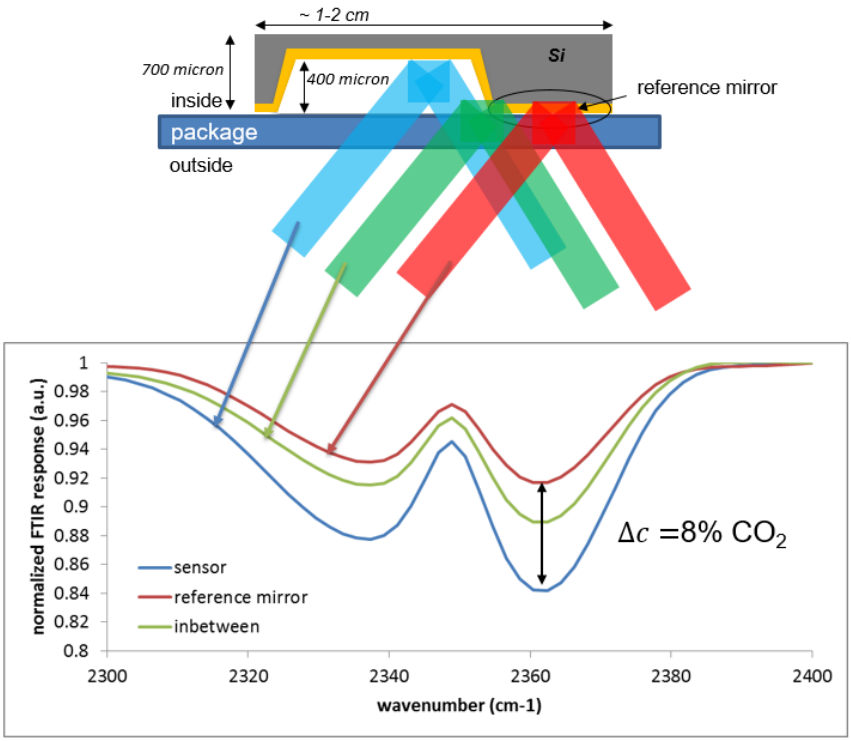

Figure 6.3: Experiment to evaluate the NDIR micro-cavity for CO_2. The gas cell is filled with 8% CO_2 at 1.4bar. An FTIR was used to characterize the spectral transmission of the NDIR cavity unit through an AR-coated window in the gas cell. By varying the focal point on the sensor, the ratio between the reference and etched region of the transducer gives the correct CO_2 concentration.

airtight seal of the food package is possible. The silicon NDIR cavity can then be further interfaced with a handheld NDIR source/detector system with a focusing system to probe two zones: one is the cavity (CO_2 signal) and the other is the reference mirror to reference out any absorption coming from the ambient air in the beam path and any absorption coming from the foil itself. The exact choice for the optics, source, detector and NDIR filters is an engineering task outside the scope of this work. In view of the relatively high LOD (a few percent CO_2, the constraints on the required specifications for the components are not demanding and it is expected that simple thermopile detector and thermal source are sufficient. In other words, there is no need in having a high-performance spectrometer or cooled detector here. A good starting point for the potential choice of components can be found here [2, 3]. It is worth noting that any other material which

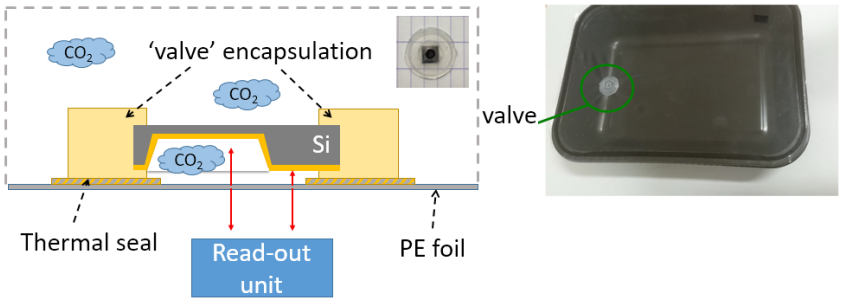

Figure 6.4: First prototype to integrate the silicon cavity piece on the package. The NDIR cavity can be embedded in a 'valve'-like structure made from hard plastic with injection molding. The valve can subsequently be welded to the food package inner foil to produce an airtight seal.

can be reliably molded into a stable, half a millimeter cavity with reflective surfaces, can also serve the same purpose as tested here. For example, a hard plastic can be directly molded and coated with a reflective powder. However, in the context of the CheckPack project, it was the intention to find a suitable carrier that can do both trace gas sensing (with the PTS approach) and CO_2 monitoring at the same time. A locally etched PIC with additional spectroscopic functionality can fulfill this task.

6.4 Conclusions

A simple NDIR system in the mid-infared for CO_2 leak monitoring was explored, specifically for leak monitoring of modified atmosphere packages. A silicon piece can be locally anisotropically etched to provide a precise optical pathlength of about 1 mm. The non-etched area on the silicon piece can be used as a reference path that will reference out any ambient CO_2 concentration variations or foil absorption.

A proof-of-concept experiment with a FTIR source and detector has shown that this approach is viable to detect percentage level CO_2 variations, sufficient for simple leak detection of MAPs. First steps were taken to integrate such components on to an actual food package foil. Injection molding around the silicon piece and subsequent thermal welding to the foil have enabled an air-tight enclosure.

References

[1] Devon Zagory and Adel A Kader. *Modified atmosphere packaging of fresh produce.* Food Technol, 42(9):70–77, 1988.

[2] Jane Hodgkinson and Ralph P Tatam. *Optical gas sensing: a review.* Measurement Science and Technology, 24(1):012004, 2012.

[3] Jane Hodgkinson, Richard Smith, Wah On Ho, John R Saffell, and Ralph P Tatam. *Non-dispersive infra-red (NDIR) measurement of carbon dioxide at 4.2 μm in a compact and optically efficient sensor.* Sensors and Actuators B: Chemical, 186:580–588, 2013.

[4] Laurence S Rothman, Iouli E Gordon, Alain Barbe, D Chris Benner, Peter F Bernath, Manfred Birk, Vincent Boudon, Linda R Brown, Alain Campargue, J-P Champion, et al. *The HITRAN 2008 molecular spectroscopic database.* Journal of Quantitative Spectroscopy and Radiative Transfer, 110(9-10):533–572, 2009.

7 Conclusions and outlook

7.1 Conclusions

The premise in this work was to explore and pursue the integration of novel, spectroscopic sensors on silicon photonic ICs for a new generation of ultra-compact, cheap, highly sensitive and selective devices. A special focus was devoted to devices operating in the SWIR and MWIR wavelength range from 2-4 µm. The application range for such devices is diverse, one can envision for example the incorporation of such sensors in food packages for food spoilage detection or one could think of incorporating such devices in a portable safety monitor or smartphone, which can measure e.g. CO_2, CO and CH_4 in the air to alert the user. To truly advance the field, low cost sensors capable of detecting sub-ppm concentrations are required. However, it was indicated that by simply scaling down existing TDLAS systems, sub-ppm sensitivities cannot be achieved and other enhancement methods are needed. In this context, two different spectroscopy routes were investigated: the realization of a fully-integrated broadband dispersive spectrometer and a disposable sensor unit which can be probed all-optically from a distance. The questions raised in the introductory chapter are now answered:

How can we reach sub-ppm sensitivity on a disposable, passive silicon chip, which is read out using an external robust optical interrogation system?

In order to reach sub-ppm sensitivities, the use of gas adsorbing coatings and on-chip photothermal spectroscopy was analyzed and developed. A

proof-of-concept demonstration indicates that sub-ppm detection is indeed possible with this method. However, the absorbance of the available preconcentration coatings are severely limiting the performance. Methods to increase the sensitivity have been proposed.

How can we integrate in a low-cost way mid-infrared sources and spectrometers on a silicon trace gas sensor for use in handheld applications?
This context has led to the development of high-resolution AWGs with outstanding performance across the full SOI operation range (2-4 µm). Further, these AWG-based spectrometers were integrated with thermo-optic modulators, enabling to use only a single, (cooled) high-performance photodiode in the mid-infrared for spectral analysis as opposed to an array of PDs, lowering the potential cost of the device. First steps have been taken towards integration further in the MWIR wavelength range at 3.3 µm, where the PIC is co-integrated on top of a butterfly packaged photodiode. A design was proposed, capable of detecting CH_4 in the 3.3 µm wavelength region in the 10-100 ppm range. The proposed integration approach is viable route for handheld applications in the mid-infrared.

Is it possible to calibrate the sensor on-line, such that a precalibration is not necessary?
The proposed photothermal sensor can in principle provide on-the-fly calibration. However, the background absorption of the coating matrix and water vapor can nullify this advantage as was observed experimentally. Further, the coating absorption coefficient is not precisely known and can vary between samples.
Moreover, fully integrated devices require calibrated on-chip optical sources. For example, the integration of widely-tunable III-V-on-SOI based external cavity laser structures is a promising approach to cover the SWIR wavelength band with a single high resolution laser source. In this context, a novel switch-based, digital FTIR-based architecture was implemented on an SOI PIC, which enables in-line monitoring of sparse emission spectra such as the wavelength output of an integrated laser. The fabricated device shows an accuracy of 100 pm over a wavelength span of 130 nm in the 2.3 µm wavelength range.

Lastly, the integration of a non-dispersive CO_2 measurement method for package integrity monitoring applications was analyzed. A simple silicon NDIR cavity was fabricated that is capable of detecting percentage level CO_2 concentrations. First exploratory steps were taken to integrate such a cavity on to a food package.

7.2 Outlook

The reliance of the photothermal spectroscopy method on the gas-adsorbing coating was proven to be a high risk and the coating background absorption limits the current usability. In order for this method to succeed, a great challenge lies in the development of novel coatings that have extremely low optical absorption in the mid-infrared. Furthermore, any component that will give a background absorption signal is detrimental. Organic contaminants such as dust or 'oily' fingerprints on the PIC will have much larger effective absorption cross-sections than the sub-ppm analyte in the MWIR 3-4 µm wavelength range, effectively burying the useful signal. The same issues will occur in on-chip mid-infrared TDLAS-based systems and care must be taken to prevent such contamination. Coming back to the case of packaged food analysis, it is questionable that this kind of contamination can be avoided in a realistic environment. Moreover, water condensation on the coating surface will also have a similar effect. The coating can be functionalized with a hydrophobic layer and in this work this has resulted in better SNR, but at the cost of added absorption peaks from the matrix in the spectrum.
It is tempting to move towards even longer wavelengths where the gas absorption cross-sections can be even higher. However, all of the above will have the same detrimental effects and water absorption will also scale.

A possible innovation direction, briefly touched upon during this PhD, is to explore integrated photoacoustic spectroscopy (PAS) methods which do not require gas adsorbing coatings. A particulary intersting method uses acoustic resonators such as quartz tuning forks (QEPAS) in such a way that is immune to external acoustic noise. This area would benefit from the compact integration of laser source, resonator and an optical interferometric 'microphone' to sense the photoacoustic wave.
The PAS methods, however have their own caveats. One notable example is that the PAS signal can experience (de)amplification depending on the gas matrix involved and on the exact gas type that is under test. For example, the presence of water vapor in the gas matrix can affect the relaxation dynamics of the absorbing gas under test, resulting in larger or weaker signals even when the pump wavelength is perfectly transparent for water.

For the integrated spectrometer designs described here, further steps involve the integration of a mid-infrared broadband source together with the PD and PIC. The coupling from the source to the single-mode waveguide will present the biggest challenge and careful optical design of the full system and microlenses, together with the fabrication tolerances must be evaluated in detail.

The 'digital', imperfect dFTIR system is a first illustration on how data driven systems can be used for sensing. The performance of the system are pushed to the limits with artificial intelligence (AI)-based processing of the data. It is not yet clear what spectroscopic sensitivity levels (LOD) of the dFTIR-architecture system can be guaranteed for a given device and unknown spectrum. Further research is needed on the optimal layout architecture and layout tolerances, as well as on the optimal number of pathways needed to achieve a certain sensitivity specification which holds true regardless of the input spectrum distribution.